

WISSENSCHAFTLICH-TECHNISCHE BERICHTE

FZR-354

September 2002

ISSN 1437-322X

Archiv-Ex.:



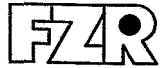
Temenoujka Fitz

Ion nitriding of aluminium

Herausgeber:
Forschungszentrum Rossendorf e.V.
Postfach 51 01 19
D-01314 Dresden
Telefon +49 351 26 00
Telefax +49 351 2 69 04 61
<http://www.fz-rossendorf.de/>

Als Manuskript gedruckt
Alle Rechte beim Herausgeber

FORSCHUNGSZENTRUM ROSSENDORF



WISSENSCHAFTLICH-TECHNISCHE BERICHTE

FZR-354

September 2002

Temenoujka Fitz

Ion nitriding of aluminium

Dissertation

Institut für Ionenstrahlphysik und Materialforschung
Forschungszentrum Rossendorf e.V.
Technische Universität Dresden

Ion nitriding of aluminium

von der
Fakultät Mathematik und Naturwissenschaften
der Technischen Universität Dresden
genehmigte

Dissertation
zur Erlangung des akademischen Grades
Doctor rerum naturalium
(Dr. rer. nat.)

vorgelegt von
Temenujka Fitz, geb. Telbizova
geboren am 19.02.1971 in Sofia, Bulgarien

Dresden 2002

Eingereicht am 3. March 2002

1. Gutachter: Prof. Dr. W. Möller
2. Gutachter: Prof. Dr. B. Rauschenbach
3. Gutachter: Prof. Dr. H. J. Spies

Verteidigt am 1. Juli 2002

Contents

Abbreviations	iv
1 Introduction	1
2 Fundamentals	5
2.1 AlN properties and methods of formation	5
2.1.1 Properties	5
2.1.2 Methods of formation	6
2.2 Surface interactions during ion nitriding	11
2.2.1 Ion-solid state interaction	11
2.2.2 Gas-solid state interaction	15
2.3 Processes in the solid state during ion nitriding	17
2.3.1 Phase formation	17
2.3.2 Diffusion	18
3 Experimental	21
3.1 Experimental equipment	21
3.1.1 Vacuum system	21
3.1.2 Ion source	21
3.1.3 Sample mounting, heating and temperature control	23
3.1.4 Sample material and preparation	23
3.2 Analysis techniques	24
3.2.1 Diagnostics of the ions and neutrals	24
3.2.2 Surface analysis	25
3.2.2.1 Ion beam analysis	25
3.2.2.2 X-Ray diffraction	33
3.2.2.3 Electron microscopy	35
3.2.2.4 Auger electron spectroscopy	36
4 Results and discussion	37
4.1 Characterisation of the ion beam and residual gas composition	37
4.1.1 Introduction	37
4.1.2 Experiment and discussion	37
4.1.2.1 Ion current density and beam uniformity	37
4.1.2.2 Beam energy and composition	39
4.1.2.3 Gas composition	41

4.1.3	Summary	43
4.2	The role of the oxide layer	44
4.2.1	Introduction	44
4.2.2	Experimental results	44
4.2.3	Discussion	46
4.2.4	Summary	47
4.3	Nitrogen incorporation and loss	49
4.3.1	Introduction	49
4.3.2	Ion-solid state interaction	49
4.3.2.1	Experimental results	49
4.3.2.2	Discussion	52
4.3.3	Gas-solid state interaction	53
4.3.3.1	Experimental results	53
4.3.3.2	Discussion	54
4.3.4	Summary	54
4.4	The mechanism of diffusional transport	55
4.4.1	Introduction	55
4.4.2	Experimental results	55
4.4.3	Discussion	58
4.4.4	Summary	59
4.5	Growth kinetics of the nitride layer	60
4.5.1	Introduction	60
4.5.2	Experimental results	60
4.5.3	Model of aluminium ion nitriding	61
4.5.4	Discussion	65
4.5.5	Summary	66
4.6	Phase formation and structure analysis	67
4.6.1	Introduction	67
4.6.2	Experimental results	67
4.6.3	Discussion	70
4.6.4	Summary	72
4.7	Characteristics and properties of the nitride layers	73
4.7.1	Atomic density	73
4.7.2	Morphology and adhesion	74
4.7.3	Stress	77
4.7.4	Stoichiometry	80
4.7.5	Electrical properties	81
4.7.6	Tribological and corrosion properties	83
4.8	Ion nitriding of the AlMg _{4.5} Mn alloy	86
4.8.1	Introduction	86
4.8.2	Experimental results	86
4.8.3	Discussion	89
4.8.4	Summary	90

List of Figures	96
List of Tables	97
Bibliography	99
Acknowledgement	108
Declaration	109

Abbreviations

AC	Alternating Current	PDF	Powder Diffraction Files
AES	Auger Electron Spectroscopy	PECVD	Plasma Enhanced CVD
BF	Bright Field	PIII	Plasma Immersion Ion Implantation
CVD	Chemical Vapour Deposition	PIIAD	Plasma Immersion Ion Assisted Deposition
DC	Direct Current	PLD	Pulsed Laser Deposition
DF	Dark Field	PN	Plasma Nitriding
ERDA	Elastic Recoil Detection Analysis	PVD	Physical Vapour Deposition
FPUW	Force Per Units Width	RBS	Rutherford Backscattering Spectroscopy
FWHM	Full Width at Half Maximum	RF	Radio Frequency
HRTEM	High Resolution Transmission Electron Microscopy	SCE	Standard Calomel Electrode
IBA	Ion Beam Analysis	SEM	Scanning Electron Microscopy
IED	Ion Energy Distribution	TEM	Transmission Electron Microscopy
I - V	Current - Voltage	TOF	Time Of Flight
MBE	Molecular Beam Epitaxy	XRD	X-Ray Diffraction
NRA	Nuclear Reaction Analysis		

1 Introduction

Aluminium is a material with a wide potential for industrial applications. It offers a unique combination of light weight and high strength. It has a low mass density of 2.7 g/cm^3 and it has about one-third the weight of iron, steel or copper. Lightweight aluminium is easy to handle. The combination of its strength with flexibility offers the possibility to be formed in different shapes and it is an attractive material for application in fields such as aerospace, automotive technology as well as high speed rail and sea travel. When used in the transportation field it can yield significant benefits in a reduction of fuel. Aluminium is suitable for cryogenic purposes. Its strength actually increases at very low temperatures and therefore it is a material of preference in the space technology. The corrosion resistance of aluminium is high due to the presence of a thin, protective film of aluminium oxide on the surface. Advantage of aluminium is that it does not rust like iron or steel. Its low cost as well as its capability to be recycled over and over without losing any of its characteristics, should be also pointed out.

However, in spite of its attractive bulk properties, even in alloyed form, aluminium exhibits poor mechanical surface properties, i.e. low hardness and high wear. Surface modification is a standard technology in modern industry used to combine different bulk and surface properties within one component. Improvement of tribological properties of metals and their alloys can be achieved by processes as nitriding, oxidizing, carburizing, boriding, etc. It has been shown that the surface properties of aluminium can be improved by formation of a nitride surface layer, because aluminium nitride exhibits high hardness and wear resistance as well as significantly enhanced corrosion resistance and high thermal and chemical stability [1, 2]. Nitriding has an advantage for application of aluminium in marine environments or other salinated humid atmospheres, where aluminium oxide dissolves by reaction with chloride and does not passivate. However, at present nitriding of aluminium does not find any large scale industrial application, due to problems in the formation of nitride layers with good quality. Requirements are a stoichiometric composition, a sufficient thickness and a smooth surface. For tribological application a good adhesion between the nitride layer and the aluminium substrate is required to prevent delamination. Moreover, for the nitriding process moderate temperatures are needed, since aluminium has a relatively low melting point of about $660 \text{ }^\circ\text{C}$.

At present, aluminium nitride layers are produced mainly by deposition. The early attempts to nitride aluminium with gas and liquid failed due to the existence of a native oxide, which acts as a barrier against nitriding. A common feature of the deposition methods is that they require a high substrate temperature. Aluminium nitride layers grown by deposition often have a poor adhesion to the substrate. Moreover, although the coating layer is many times harder than the covered metal, it can easily break when

a force is applied due to the weak material inside. The later phenomenon is known as "egg-shell" effect. In this context, layers produced by an ion implantation technique are supposed to have an advantage, since usually a concentration gradient between the layer and the substrate is formed, which results in better adhesion. Combining ion implantation of aluminium with a subsequent deposition of aluminium nitride can avoid the "egg-shell" effect, since the intermediate layer created by implantation improves the interaction between the hard coating layer and the soft aluminium bulk. Furthermore, it results in formation of thicker nitride layers with better surface properties than these achieved by a single process of deposition or implantation. Such combined processes are called duplex (two-step) processes, and they exhibit a high potential for surface hardening [3, 4].

The present study is devoted to formation of aluminium nitride layers by ion implantation as it is a method of significant importance for surface modification of aluminium either as a single or a duplex process. Now a days, the most established implantation method is the beam line ion implantation. It provides ions with a high energy in a broad energy range and thus offers a possibility for very good control over the modification depth. However, beam line ion implantation is not applied for surface modification of metals on an industrial scale, since it is a complicated and relatively expensive method. More attractive for the industry is the plasma immersion ion implantation technique (PIII), which has a possibility for surface modification of large three-dimensional components at lower costs. During plasma immersion ion implantation, as the name suggests, ions are extracted from a plasma surrounding the sample and implanted with a maximum energy of about 40 keV. Another similar method, which has a potential for industrial application, is the plasma nitriding (PN). It consists of glow discharge created around the sample, which provides neutrals and ions with an energy of several hundred volts only. Due to the energy limitation in this methods, the depth of modification is limited. Therefore in both, PIII and PN, diffusion is used to grow nitride layers with a sufficient thickness. Such a combination of nitrogen implantation and diffusional transport is successfully applied to improve the surface properties of steel, since the nitrogen atoms diffuse quickly into the steel substrate and form a protective layer [5, 6, 7, 8, 9]. However, the mechanism of diffusional transport during nitriding of aluminium is not understood yet. Another problem which occurs at low-energy ion implantation is related to the influence of the surface oxide layer. If the energy of the ions is not sufficient to penetrate through the oxide, it can act as a barrier against nitriding or induce a contamination with oxygen [10, 11]. In particular, the lack of understanding leads to difficulties in achieving control over the process and limited reproducibility. Therefore, it is of practical interest to obtain knowledge about the mechanism of aluminium nitride layer formation.

The aim of the present study is to investigate the mechanism of aluminium nitriding by techniques that employ implantation of low-energy nitrogen ions and diffusional transport of atoms. By definition ion nitriding consists of a heat treatment involving diffusion, whereby nitrogen is introduced into the surface area of a solid substrate [12, 13]. The term "ion" is used to indicate that the nitrogen is mainly supplied to the substrate by nitrogen ions. In the present study the nitrogen ions are delivered by an ion beam produced from a hot filament ion source. This has some of the advantages of the beam line ion implantation such as a very good control over the ion energy, fluxes, substrate temperature and a low contamination. Furthermore, the process parameters can be independently controlled and

therefore closely related to physical characteristics, which allows the physical description of the mechanism of aluminium nitriding. It should be pointed out, that ion nitriding differs from the above mentioned PIII and PN due to the way of ion delivery but a close similarity between the methods exists. Therefore, ion nitriding can be used as a model system for plasma nitriding and plasma immersion ion implantation. By applying ion beam diagnostic and different methods of surface analysis such as ion beam analysis, X-ray diffraction, electron microscopy etc., the phenomena of aluminium ion nitriding will be studied. Recently, the nitriding mechanism of austenitic stainless steel during ion nitriding has been successfully investigated [14]. In this study, a similar approach is used to investigate the mechanism of aluminium ion nitriding.

To fulfill the aim of this study, first the interaction between the nitrogen ions and the solid aluminium surface in terms of nitrogen incorporation and sputtering will be studied. Of particular importance is an investigation of the role of the surface oxide on the mechanism of nitrogen incorporation. Special emphasis will be given to a study of the diffusion phenomenon during nitriding of aluminium. An investigation of the growth kinetic of the aluminium nitride layers as a function of the process parameters will be presented. Characterisation of composition, phase formation, structure, surface morphology and other properties of the obtained nitride layers as density, hardness and corrosion resistance will be described, since they are of significant importance for the final application of this technique. In addition, a study on the ion nitriding of AlMg_{4.5}Mn alloy will be performed and the obtained results will be compared to those obtained by ion nitriding of pure aluminium.

The present study is structured as follows: In chapter 2, after reviewing the properties of aluminium nitride and the different techniques for its production, a short overview of the fundamental phenomena taking place during ion nitriding of aluminium is presented. In chapter 3, the description of the used experimental system as well as the applied diagnostics of the ion beam and surface analyses is given. The main part of the thesis is chapter 4, where the results are shown and discussed. The last chapter contains a summary and conclusions.

2 Fundamentals

2.1 AlN properties and methods of formation

2.1.1 Properties

In equilibrium aluminium nitride (AlN) has a hexagonal closed packed wurtzite structure, as shown in Fig. 2.1. In this lattice, the aluminium and nitrogen atoms are 4 - fold coordinated in a tetrahedral geometry. AlN has a mass density of 3.26 g/cm^3 and a high atomic density of $9.58 \times 10^{22} \text{ at/cm}^3$ [15]. Its hardness of 1200 HV is high, resulting to a low wear [16]. The melting temperature of AlN is about $2800 \text{ }^\circ\text{C}$. This high thermal stability is accompanied by good chemical stability and corrosion resistance. Beside the tribological properties, AlN has interesting thermal, electrical, optical and acoustic properties. For instance, it has a small thermal expansion coefficient of $4.84 \times 10^{-6} \text{ K}^{-1}$ in a temperature range of $25 \text{ }^\circ\text{C}$ to $600 \text{ }^\circ\text{C}$ and a high thermal conductivity of 30.1 W/mK and 20.06 W/mK at $25 \text{ }^\circ\text{C}$ and $600 \text{ }^\circ\text{C}$ respectively [17]. Aluminium nitride is a wide band gap semiconductor with a direct band gap of 6.2 eV . The binding is partially ionic with a significant degree of covalency. Also, AlN has a high specific electrical resistivity of about $10^{11} \text{ } \Omega\text{m}$, a static dielectric constant of 8.5 and low dielectric loss. Pure AlN is highly transparent over a broad wavelength range from 200 nm to approximately $12.5 \text{ } \mu\text{m}$. The acoustic wave velocity of AlN along the c-axis with a value of 10.4 km/s is one of the highest among those of piezoelectric materials [18].

Due to these properties, AlN is a material of preference in many different areas. Formation of an AlN layer on the surface of aluminium can be used to improve its hardness, wear and corrosion resistance. Moreover, AlN thin films can find applications in microelectronic and optoelectronic devices as passivation and dielectric layers in integrated circuit short wavelength emitters. AlN is a very good buffer layer for deposition of GaN on sapphire or silicon substrates [19]. It can also be used as a phase contrast layer in optical discs [20]. Due to its high surface acoustic wave velocity, AlN thin films can be used as low frequency filters, which are utilized for example in mobile communication equipments [21, 22]. Aluminium nitride films find an application as pyroelectric sensors because AlN exhibits a temperature dependent spontaneous polarization along the c-axis and therefore are used to measure heat irradiation [23].

Because of the wide range of applications, AlN has been studied for many years. However, its properties depend very sensitively on the production method and also on contamination, especially of oxygen.

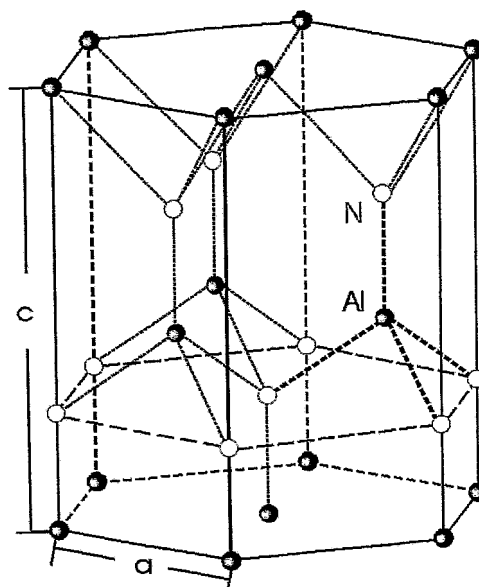


Figure 2.1: AlN wurtzite structure with lattice constants $a = 3.11 \text{ \AA}$ and $c = 4.98 \text{ \AA}$.

2.1.2 Methods of formation

The techniques which are used for production of AlN layers can be subdivided in two main groups: deposition and implantation methods. Deposition methods are mainly used for formation of AlN layers on silicon and sapphire substrates, because when deposited on aluminium they often have a poor adhesion to the substrate. The second group of methods are applied for surface modification of aluminium and aluminium based alloys.

Deposition methods can be classified as chemical vapour deposition (CVD) or physical vapour deposition (PVD). In a CVD process a vapour phase dispersion of the material to be deposited is created. A thermally driven chemical reaction takes place either in the vapour phase very near to the surface or on the substrate itself. A low pressure is not always required. CVD depends on the availability of volatile chemicals which can be converted by some reactions into the desired solid. AlN has been produced by reaction of organometallic compounds [24, 25, 26, 27]. CVD of AlN requires a very high reaction temperature above $1000 \text{ }^\circ\text{C}$. This drawback can be overcome by using plasma enhanced CVD (PECVD), where a plasma activates the species and thus decreases the deposition temperature [28, 29, 30, 31]. However, the nitride layers produced by this technique contain a lot of contaminations. Now a days the CVD technique is almost exclusively used in laboratory environments and is practically not applicable for industrial purposes. PVD consists in production of the atomic, molecular or ionic species needed for deposition by evaporation or sputtering from a solid target. These species are transported to the substrate, where an atomic assembly takes place. Thermal evaporation requires a sufficiently low pressure to allow the vapour to propagate freely to and condense on the substrate. PVD includes techniques such as molecular beam epitaxy (MBE), electron

beam melting and evaporation and laser ablation. MBE deposition has been used to grow AlN single crystals and highly textured AlN films with excellent quality [32, 33, 34]. For production of AlN epitaxial layers a high temperature, above 800 °C, is also necessary. This prevents the application of MBE for coating of aluminium, since this temperature is above its melting point. Using plasma source MBE the substrate temperature can be decreased down to 600 °C [35]. Another PVD method which has been proven to produce AlN films with good quality and low oxygen contamination is pulsed laser deposition (PLD) [36, 37, 38, 39]. Due to the congruent evaporation of compounds and their transfer to the substrate it results to a high deposition rate without significant contamination. However, the application of PLD for industrial purposes is limited due to the sophisticated equipment and requirement for scanning of the laser beam or target manipulation in order to obtain layers with desirable thickness uniformity. The atomic vapour is not only produced by thermal evaporation, it can be created also by sputtering of the target material. This method gives a possibility to use many different solid materials as a target, since a physical momentum-exchange process is applied. There are numerous variants of sputter deposition in use today, which can be classified as DC diode, RF diode, magnetron or ion beam deposition. Sputter deposition may be carried out in a variety of systems, which may differ in the sputtering configuration, geometry, target type, substrate position, gas type and pressure. In DC diode, RF diode and magnetron sputtering systems, both the sputter target and the substrate are immersed in the plasma from which the ions for sputtering are extracted. In an ion beam deposition system, the ions needed for sputtering are generated in an external ion source. The difference between the systems does not change the basic sputtering process itself but it results in different fluxes and energies of sputtered atomic or ion species impacting the substrate. Using sputtering techniques AlN films with controllable stoichiometry, composition and with a high thickness uniformity have been produced at high deposition rate also on an industrial scale [40, 41, 42, 43, 44, 45, 46]. However, problems due to process instability as a result of inhomogeneous sputtering and poisoning of the target by the reactive gas exist.

To the second group belong all methods in which energetic nitrogen ions are implanted into the a substrate of aluminium or aluminium alloy. Depending on the way of providing the ions, these methods can be classified as implantation with or without mass separation. Conventional beam line ion implantation is carried out in a vacuum environment in which an ion source is used to create ions of the species to be implanted. Then after mass separation the ions are accelerated by a potential of tens to hundreds of kilovolts and directed onto the sample. This technique is preferable for modification of materials for which a high temperature treatment is not required. A very good control over the implanted species, fluxes, ion energy and thereby the depth of modification can be achieved. Several studies have been published on the formation of AlN by conventional implantation of nitrogen ions into aluminium substrates [47, 48, 49, 50, 51, 52, 53, 54, 55, 56, 57]. However, as a line of sight method the implantation has its shortcomings, mostly related to the small size of the beam spot. For treatment of larger substrates, the beam has to be scanned across the surface, which requires long processing times in particular, if high doses are necessary. This, in addition to the complexity of a conventional implanter makes the method economically unattractive. However, for many purposes a mass separation

is not important. In this case, more simple equipment can be used, which decreases the cost and makes the method more attractive for application. Such techniques are plasma nitriding (PN), plasma immersion ion implantation (PIII) and broad beam ion implantation. A drawback is that these methods provide low energy ions, which limits the depth of material modification to the near surface area. To overcome this obstacle, the substrate is heated to a temperature, which allows diffusion of atoms. As a result the depth of modification can be sufficiently increased. When heat treatment and diffusion are involved for the formation of the AlN layer the method is often called ion nitriding, as used in the present study.

The conventional plasma nitriding uses a glow discharge of diode type in a high pressure of nitrogen (100 - 1000 Pa). A DC voltage (typically 0.3 - 1 keV) is applied between a cathode on which the sample is placed and the chamber wall [58]. Under this conditions, an anomalous glow discharge builds up around the sample. A flux of neutrals and ions bombards the surface and provides the activation energy for chemical reaction. At present, plasma nitriding is more often performed by pulsed DC voltage. It has some advantages such as the possibility to adjust the substrate temperature without altering the plasma parameters and control over the nitriding process by selection of the ratio of pulse duration to pulse repetition. The early attempts to nitride aluminium by plasma nitriding failed because of the native oxide, which exist on every aluminium surface. Arai et al. [10] were the first to show that plasma nitriding of aluminium is possible, if the oxide layer is removed by a sputtering process prior to the nitriding. After applying a sputter cleaning with argon or argon-hydrogen mixture, thick nitride layers (up to 10 μm) were obtained by plasma nitriding of aluminium alloys [59, 60, 61, 62]. In contrast, Reinhold et al. reported formation of AlN layers with sufficient thickness (about 8 μm) without additional pre-treatment sputtering [63]. The authors assume that removal of the oxide layer occurs simultaneously to the nitriding process. However, the nitride layers produced by plasma nitriding often contain a high amount of oxygen contamination [64]. Plasma nitriding at low pressure (0.5 - 10 Pa) can be performed by using an additional thermionic electron source to the conventional diode system [65, 66, 67]. The electrons are used to increase the plasma ionisation. Another modification of plasma nitriding at low pressure is the arc-assisted plasma process [68, 69]. In this method, a thermionic arc discharge is generated in argon in a ionisation chamber mounted on the top of the reactor. Segmented anodes lining the reactor wall spread the plasma emanating from the ionisation chamber uniformly over the nitriding chamber. These segmented anodes and a hot filaments in the ionisation chamber create a uniform, low pressure plasma (0.4 - 0.8 Pa). In arc-assisted plasma process, samples can be nitrated at floating potential or based to a DC voltage. However, Renevier et al. [70] reported that aluminium can be nitrated only if bias is applied. The mechanism of plasma nitriding has been investigated in several studies. Optical emission spectroscopy and mass spectrometry have been applied to analyse the glow discharge [58, 68, 69, 70, 71, 72, 73]. A model at which the nitrogen ions (atoms and molecules) are responsible for the formation of the nitride layer is presented in Ref. [74, 75]. A mechanism governed by physisorption of molecules on metal surfaces followed by low-energy ion bombardment induced surface nitride formation is published in Ref. [76, 77, 78]. In other studies [79, 80] it is concluded that during plasma nitriding process the active species are the nitrogen atoms.

The plasma immersion ion implantation technique combines elements from ion implantation with elements from conventional ion nitriding. In PIII, the substrate to be nitrified is immersed in a plasma, generated by an external source such as filament discharge, radio-frequency and electron cyclotron resonance source [81]. Positive ions are extracted from the plasma and accelerated by applying a series of negative high-voltage pulses (10 - 40 kV). A plasma sheath forms around the sample and ions bombard the sample. This method is also often called plasma source ion implantation (PSII) and it is widely used for nitriding of aluminium and aluminium alloys [2, 8, 82, 83, 84, 85, 86, 87, 88]. Richter et al. [89] have reported formation of 15 μm thick nitride layer with a stoichiometric concentration and good adhesion by PIII of AlMg_{4.5}Mn at 40 kV bias voltage and 500 °C substrate temperature. A big advantage of the method is its ability to implant the whole surface of large three dimensional components with satisfying uniformity in a short implantation time since it provides an high ion current density. However, the absence of the mass separation system can be a reason for sample contamination, because all ionized species are implanted.

During broad beam ion implantation the sample is exposed to a high flux of energetic ions produced by an ion source. The ions are created in a plasma discharge in the volume of the source. They are accelerated and formed as a diverging beam, usually by means of simple grid systems. The broad beam gas ion sources have a limitation in ion energy of about 5 keV. This method allows good control over ion energy and flux. Moreover, since the plasma is located only in the volume of the ion source a process can be achieved, which is basically free of contamination. The method allows precise and independent control over the substrate temperature during the nitriding process. Nitriding of aluminium and aluminium alloys by an ion source at low energies is reported in Ref. [53, 90, 91, 92, 93].

A combination of deposition and plasma immersion techniques is the so called plasma immersion ion assisted deposition (PIIAD) method. During PIIAD a metal plasma, normally produced by a cathodic arc, is combined with applying high voltage pulses to the substrate. Formation of compound films is possible by using reactive gases. In order to avoid deposition of droplets, which are emitted from the arc, the plasma can be filtered by magnetic field [94] or by shield plate [95]. Recently, a study on the formation of high textured AlN layers on silicon and sapphire substrates by PIIAD has been published [96, 97].

2.2 Surface interactions during ion nitriding

2.2.1 Ion-solid state interaction

When an energetic ion interacts with a solid state, it loses its kinetic energy due to electronic interactions and nuclear collisions. As a consequence of the interaction, the incident ion is slowed down to energies in the order of the solid state binding energies (collisional phase) and finally to thermal energies by excitation of phonons. In electronic interaction the ion slows down but does not change its direction. Nuclear collisions cause a change of the ion direction and in the extreme case the ion is backscattered. Moreover, during nuclear interaction the energy of the ion transferred to the collision partners may cause radiation damage. In dependence on the transferred energy the atoms of the substrate can be displaced than a short time or be deposited at a site different from their original one. For sufficiently large energy transfer, an ion may create fast recoil atoms which in turn may initiate collision cascades of uncoordinated moving atoms. If atoms suffer collisions close to the surface, they can be scattered out of the solid state, which is known as sputtering. For an extended irradiation, sputtering causes a removal of the surface layer. After slowing down, the ions are incorporated into the substrate materials. They create a change of the composition and structure of the solid state. Lattice defects such as vacancies, interstitials, self-interstitials and substitutional impurities are created. If chemically active ions are used, different chemical reactions may occur resulting in the formation of new phases [98].

For details of the ion-solid state interaction the interested reader is referred to e. g., Refs. [99] and [100]. Here only a brief description will be given.

To calculate the nuclear energy loss in the solid state per unit distance the interaction potential has to be known. Normally, this is a screened Coulomb potential:

$$V(r) = \frac{1}{4\pi\epsilon_0} \frac{z_1 z_2 e^2}{r} \chi\left(\frac{r}{a}\right) \quad (2.1)$$

where z_1 and z_2 are the atomic numbers of the incident ion and target atoms, respectively, ϵ_0 is the dielectric constant in vacuum and $r/a = x$ is the distance in units of the screening length a and $\chi(r/a) = \chi(x)$ is the screening function as, e. g., the Thomas Fermi screening function.

The average energy loss per covered distance x can be defined by the stopping power $-dE/dx$ or the stopping cross section:

$$S = -\frac{1}{n} \frac{dE}{dx}, \quad (2.2)$$

where n denotes the atomic density of the solid substrate. Assuming that the nuclear and the electronic interactions act independently, the total stopping cross section is composed of a nuclear and an electronic fraction:

$$S = S_n + S_e. \quad (2.3)$$

The stopping cross section can generally be written as:

$$S = \int T d\sigma(T), \quad (2.4)$$

where T denotes the energy transfer and $d\sigma$ the interaction cross section. In case of the nuclear interaction, the elastic energy transfer is given by:

$$T_n = E_0 \frac{4M_1 M_2}{(M_1 + M_2)^2} \sin^2 \frac{\vartheta_c}{2}, \quad (2.5)$$

where E_0 is the initial ion energy, M_1 is the mass of the incident ion, M_2 is the mass of the substrate atoms and ϑ_c is the scattering angle in the center of mass system. The nuclear interaction cross section can be determined from the interatomic interaction potential Eq. 2.1.

In the present study, the electronic energy loss (S_e) plays a minor role due to the relatively low ion energy (< 3 keV). If the velocity of the ion is small compared to the Bohr velocity v_0 , which is the case here, S_e is proportional to the square root of the ion energy, E :

$$S_e \propto \sqrt{E} \quad (2.6)$$

For incident N^+ ion energies between 0 keV to 10 keV in aluminium and AlN, the nuclear and electronic stopping power are shown in Fig. 2.2.

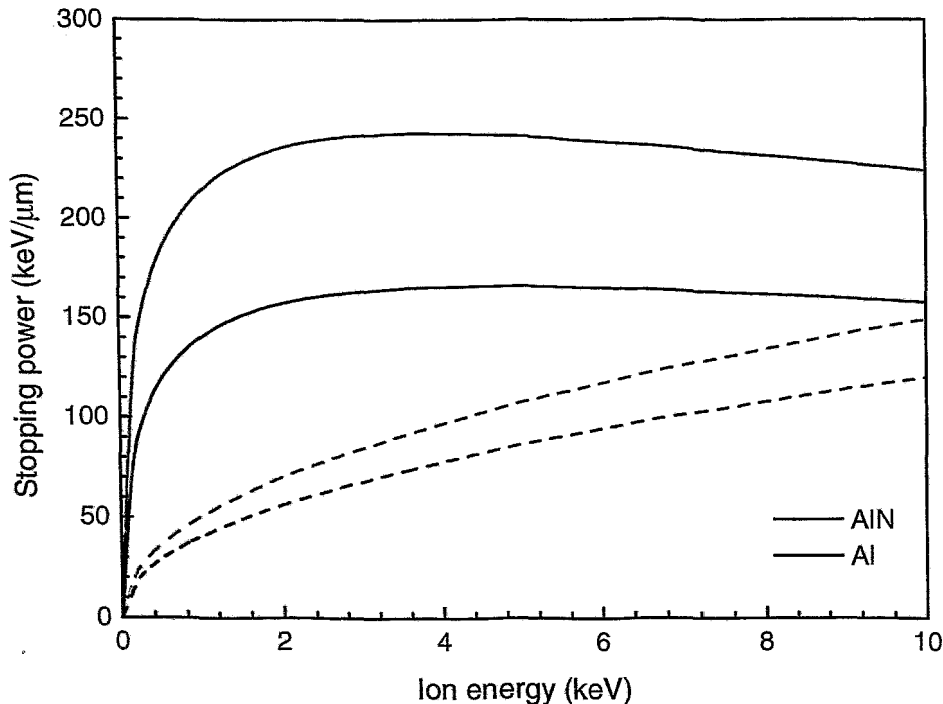


Figure 2.2: Comparison of nuclear stopping power (solid line) and electronic stopping power (dashed line) for atomic nitrogen ions in Al and AlN substrate, taken from SRIM 2000 [101].

Depending upon the amount of deposited energy per unit volume, three different regimes of a collision cascade can be distinguished: i) single collision, ii) linear cascade and iii) thermal spike. In the single collision regime the cascade does not really develop and the atomic motion is stopped after a few collision events. In the linear cascade regime the collisions take place essentially only between fast ions and atoms being at rest. In the thermal spike regime the lattice atoms within the cascade become a thermal ensemble with a high temperature, which may exceed the melting temperature of the solid state. For the energies mainly used in this work, the collision cascade is assumed to be in the linear regime. However, for the case of energy ≤ 250 eV the cascade is in the single collision regime [102].

For practical ion implantation the mean projected range R_p is the most important parameter. It is defined as the most probable distance of the stopped ion to the surface. There are analytical formulas to calculate the distribution of the projected range, but they contain many approximations. In a simple approximation the distribution is Gaussian like. Fig. 2.3 shows the mean projected range R_p calculated by TRIM [103] as a function of energy for N^+ ions into Al and AlN at normal incidence. The ion energy is chosen corresponding to the energy range of the ion source used here. R_p shows an almost linear dependence on the incident ion energy. It is larger in case of the aluminium than for AlN due to the difference in atomic density.

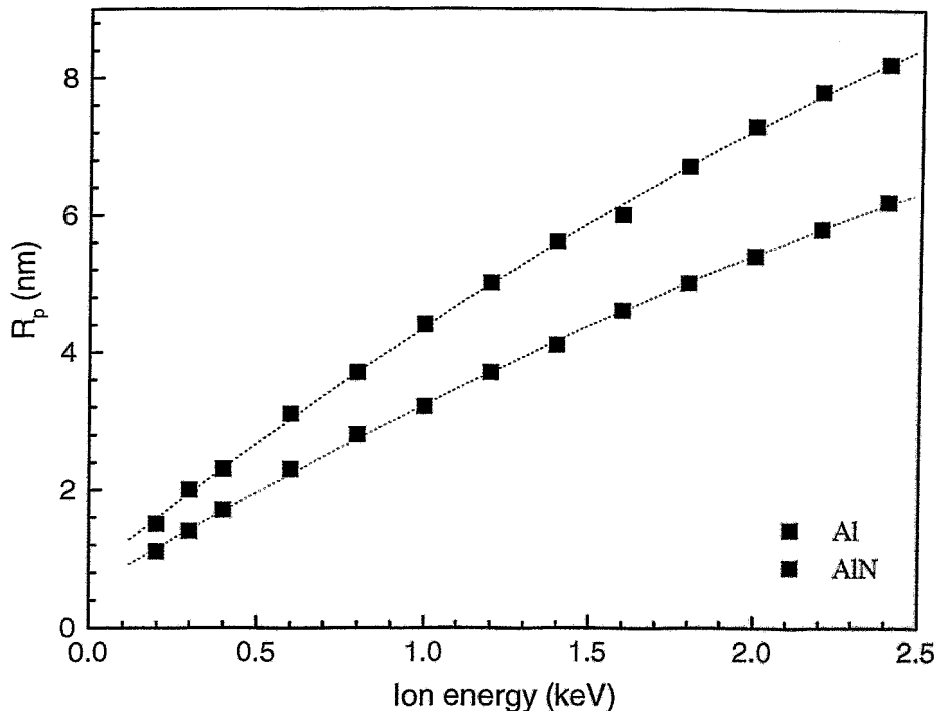


Figure 2.3: The mean projected range of atomic nitrogen ions implanted into Al and AlN as a function of ion energy obtained by TRIM simulations. 5000 projectiles were calculated for each energy.

During ion implantation sputtering plays an important role since it may set the limit to the maximum concentration of atoms that can be incorporated in a material. The sputtering yield is defined as number of sputtered atoms per incident ion and depends on ion species, ion energy, substrate material and incidence angle of the ion onto the substrate surface. According to the "Sigmund model" [104] (linear cascade regime) the sputtering yield, Y , for normally incident ions with energy E_0 is given by:

$$Y(E_0) = \frac{4.2 \cdot 10^{14} \text{ cm}^2}{E_s} \zeta \left(\frac{M_1}{M_2} \right) S_n(E_0), \quad (2.7)$$

where E_s is the surface binding energy (see below) and ζ is tabulated as a function of the mass ratio. For the case of low incident energies (single collision regime) the above formula is not valid anymore due to the existence of a sputtering threshold energy. In this case semiempirical formulas have to be applied [99, 100, 102]. For ions incident at an angle θ with respect to the surface, the normal linear cascade theory predicts a rise in the yield proportional to $\cos^{-f} \theta$, where the exponent f is a function of M_2/M_1 . Knowing the sputtering yield for a given energy and the incident ion flux j_0 , the flux of sputtered atoms, j_{sp} , can be calculated by:

$$j_{sp} = Y \cdot j_0 \quad (2.8)$$

In practice, computer programs based on the binary-collision approximation are often used for simulation of the ion-solid state interaction. In this study the projected ranges of ions are simulated by TRIM [103, 101] and TRIDYN [105, 106] is applied to estimate the sputtering and backscattering yields. TRIM considers only a static substrate and therefore it is strictly valid only in the limit of low implantation fluences. TRIDYN is a "dynamic" version of TRIM, which simulates the dynamic change of thickness and composition in the substrate during high-dose ion implantation. In both programs, the incoming ions are characterised by their mass, atomic number, angle of incidence and kinetic energy. TRIDYN considers also the incident fluence. For the case of molecular ions, as N_2^+ used here, it has to be taken into account that the collision with the surface causes a dissociation of the molecule. Then, the incident energy of the molecule is distributed according to the atomic masses of the molecule components ("Shrapnel model"). For instance, the N_2^+ molecule ions dissociates to two single N atoms, each of them taking one half of the incident energy. The substrate is characterised by its density and composition. The simulations were performed using the standard atomic density of AlN (9.58×10^{22} at/cm³) and assuming composition of stoichiometric AlN. For calculation of the oxygen sputtering yield due to implantation into an aluminium oxide layer the atomic density of Al_2O_3 (1.17×10^{23} at/cm³) is used [15]. Other important input parameters of the substrate for TRIDYN and TRIM are the following binding energies:

1. The surface binding energy E_s . It is the energy that a target atom must overcome to leave the surface of the substrate. According to Eq. 2.7 this energy determines critically the sputtering yield, being proportional to the inverse of the surface binding energy. E_s is often set equal to the sublimation enthalpy ΔH_s . For the case of a metal-gas compound $A_n B_m$, where B is the gaseous element, the surface binding energy can be calculated by taking into consideration the thermodynamic balance as following [107]:

$$E_s(A-B) = \frac{1}{2}\Delta H_s(A) + \frac{n+m}{4n}\Delta H_m(B) + \frac{n+m}{2nm}\Delta H_f(A_nB_m), \quad (2.9)$$

where $\Delta H_f(A_nB_m)$ denotes the formation enthalpy per molecule of the compound and ΔH_m the molecular binding energy of B. The surface binding energy in AlN, $E_s(Al-N)$, is calculated to be 9.1 eV by taking $\Delta H_s = 3.36$ eV, $\Delta H_m(N_2) = 9.84$ eV, $\Delta H_f(AlN) = 2.5$ eV [15] and applying Eq. 2.9. The surface binding energy in Al_2O_3 , $E_s(Al-O)$, is found to be 12.1 eV for $\Delta H_s = 3.36$ eV, $\Delta H_m(O_2) = 5.16$ eV and $\Delta H_f(Al_2O_3) = 17.36$ eV [15]. $E_s(Al-Al)$ is taken equal to the sublimation enthalpy of aluminium ($\Delta H_s = 3.36$ eV). Neglecting any chemistry between the gas atoms, it is assumed that $E_s(N-N) = E_s(O-O) = 0$ eV.

2. The bulk binding energy E_b . It is the energy that each recoil atom loses when leaving its lattice site and collides with other substrate atoms. A well-defined value for this energy is difficult to obtain and therefore it is often set to zero. The experience shows that such a choice leads to reasonable results, if the surface binding energy is chosen properly [107].

3. The cutoff energy E_c . It determines the energy at which any projectile or atom in a collision cascade is stopped. For a correct calculation of sputtering, a reasonable value for the cutoff energy should be equal or less than the surface binding energies.

The TRIDYN simulations were performed in a stationary mode, i. e. by assuming that the AlN matrix remains unaltered. The obtained sputtering and backscattering yields are shown in Fig. 2.4 as a function of the incident ion energy. The sputtering yield of both nitrogen and aluminium increases as the beam energy rises up to 1.2 keV and shows only a weak energy dependence at higher beam energies. The backscattering yield exhibits a different behaviour with a slight decrease as the beam energy increases. These values are used for theoretical estimation of nitrogen loss due to sputtering and backscattering as described in section 4.3.

2.2.2 Gas-solid state interaction

Besides the influence of the energetic ions, the substrate is also exposed to the interaction with the residual gas. The effect of gas-solid state interaction is often not taken into consideration but in fact it can contribute to the growth of the nitride layer. The neutral species can be reflected from the surface or be selectively bound from the gas phase to the surface of the solid state. The last phenomenon is called adsorption. The adsorbed species can be bound by weak Van-der-Waals bounds (physisorption) or by chemical binding (chemisorption).

For this study it is of importance to consider the interaction of oxygen and nitrogen neutrals with the aluminium surface. The effect of oxygen chemisorption on a clean aluminium surface has been investigated for example in Refs. [108, 109]. It has been observed that the chemisorbed oxygen atoms form a coverage layer on the aluminium surface. Due to an effect of high temperature (300 °C) the oxygen atoms become mobile and a transformation to the oxide phase takes place. To the knowledge of the author, at present no information is available on the effect of nitrogen neutral species. There are

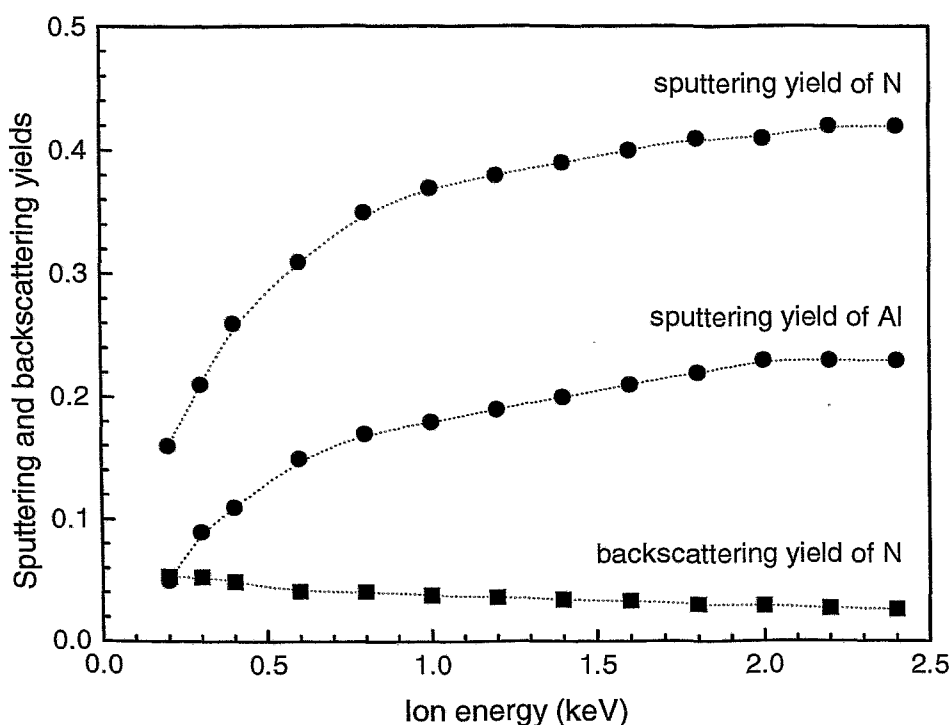


Figure 2.4: Partial sputtering yields of nitrogen and aluminium, and backscattering yield of nitrogen as function of the ion energy, calculated by TRIDYN. The simulations were performed for atomic nitrogen ions implanted into an AlN substrate using $E_s(Al-N) = 9.1$ eV, $E_s(Al-Al) = 3.36$ eV, $E_s(N-N) = 0$ eV and $E_b = 0$ eV.

some similar studies (for example Ref. [110]) on the adsorption of ammonia on a NiAl substrate and subsequent decomposition, which leads to formation of AlN layers.

In addition, the effect of neutrals might be enhanced by the ion irradiation since synergisms between ion bombardment and chemistry might exist. This phenomenon is known as ion induced interaction. The ions might have two effects on the adsorbed neutrals: i) they can stimulate desorption of the adsorbed neutrals (ion - stimulated desorption) or ii) they can also increase the chemisorption of the neutral species. The mechanism of ion induced interaction is not well understood up to now and there are a lot of open questions. Its effect on the N - Al system is also not known. An example for an ion induced nitriding of a metal substrate can be found in Ref. [111]. In this study, a Nb sample has been exposed to nitrogen gas under Ar^+ ion bombardment. It has been shown that the bombardment with argon ions stimulates the reaction between the adsorbed nitrogen and the metal atoms producing a NbN layer.

2.3 Processes in the solid state during ion nitriding

When atoms of a foreign element are added to a solid state system, they cause an increase in the free energy. Since every system tends to reach its equilibrium state with the minimum energy, a transformation can occur and a new phase can be formed. One of the most fundamental processes by which a system attempts to reach a stable arrangement of its atoms is diffusion. These two phenomena, phase formation and diffusion, are of significant importance for the formation and growth of the nitride layer during ion nitriding of aluminium. Therefore, they will be briefly discussed here with respect to the Al-N system. A more detailed information is available for example in Refs. [112, 113]. In addition, it should be noted that when the new element is introduced into the system by ion implantation, several other effects such as defects formation, ion induced segregation and diffusion, ion mixing etc. can occur [98]. This makes the description of the processes in the solid state a quite complicated task.

2.3.1 Phase formation

The phases which a system of two elements forms at different concentration of the elements in dependence on temperature, when the system is in equilibrium, are given by a binary phase diagram. For Al - N system the binary phase diagram is shown in Fig. 2.5. The established equilibrium solid phases are the solid solution of nitrogen in the Al f.c.c. lattice and hexagonal AlN. The solid solution phase exists stably only at a very small concentration of nitrogen, less than 0.002 % [50]. A system can also form different phases under an influence of pressure. At low hydrostatic pressure the aluminium nitride has a wurzite type structure (see Fig. 2.1). At elevated pressure AlN can undergo a transformation to a cubic zinc-blende or a NaCl type structure [114].

In fact, as mentioned above, the phases formed as result of ion implantation are often different from what is predicted by the equilibrium thermodynamics, giving rise to order-disorder transformations, metastable phase formation and growth, grain growth, preferred texture, densification etc. The phase formation during nitrogen ion implantation of aluminium was studied by Lucas et al. [115, 116]. They have shown that nitrogen embedded in the f.c.c. Al lattice causes a metastable transition to the f.c.c. AlN phase, which has a crystallographic relationship with the aluminium matrix. At low concentration of nitrogen, the nitrogen atoms occupy the tetrahedral interstitial sites in the {111} planes of the aluminium lattice. When the solid solubility is exceeded, slip of atomic planes of the f.c.c. Al occurs, which leads to formation of AlN precipitates in the more stable hexagonal close packed form.

Once small precipitates are formed (nucleation), further supply of nitrogen atoms to the system can make them growing. In principle, nucleation induces change of the free energy of the system due to three main factors: i) creation of a volume with the new phase, which causes a reduction of the volume free energy, ii) creation of an interface area, which gives an increase in the free energy and iii) the fit of the volume with the new phase in the space of the original matrix, which gives rise to the misfit strain energy. The growth of the nuclei is controlled by the requirement of energy minimization of the system. Again, Lucas et al. [116] have shown that during nitrogen implantation into aluminium

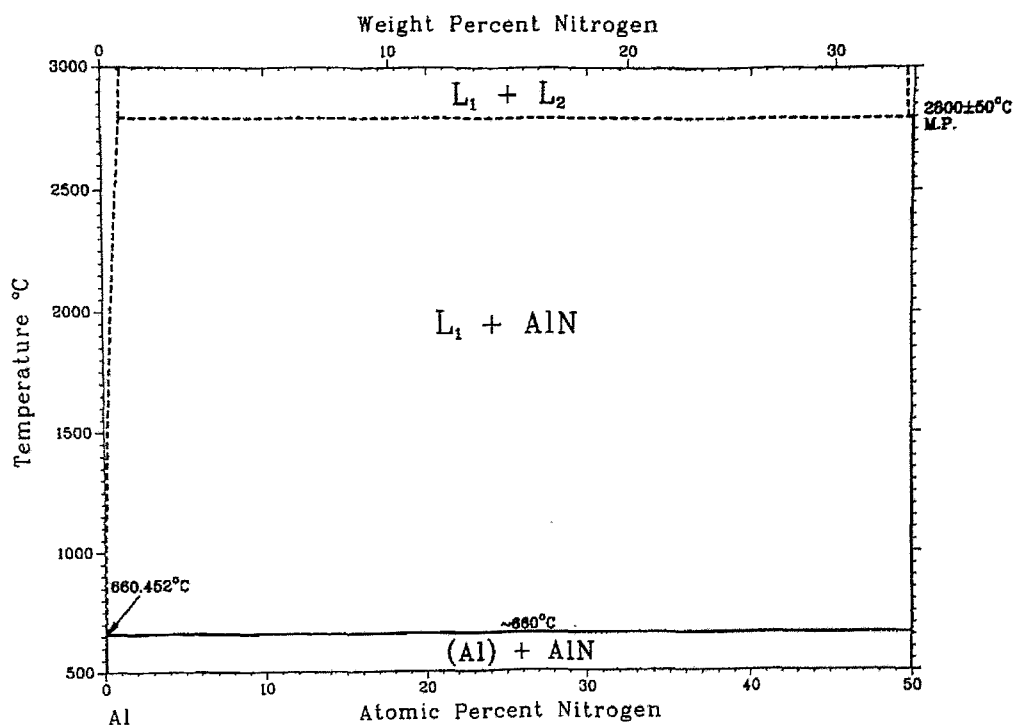


Figure 2.5: Al - N binary phase diagram taken from Ref. [114], for details see text.

the nuclei grow preferably in the $\langle 111 \rangle$ direction favouring to the large space available. A dependence of the nucleus size on the process temperature was observed. At temperatures equal to or lower than 300°C small precipitates are created. At higher temperature larger but few precipitates are formed, most probably due to the higher diffusivity of the atoms.

2.3.2 Diffusion

In general, by introducing a fraction of an element into a solid system the chemical potential of this element in the system changes. Then, due to the difference in the chemical potentials, atoms start to diffuse down the chemical potential gradient, if the provided mobility is sufficiently high. It is often said that the atoms diffuse away from the regions of high concentration to the regions of low concentration. This is not always the case, but in practice the concentration differences are easier to measure and therefore it is more convenient to relate diffusion to the concentration gradient than to the chemical potential gradient. In this sense, the flux j of diffusing atoms is proportional to the concentration gradient:

$$j = -D \frac{\partial c}{\partial x}, \quad (2.10)$$

with the diffusion coefficient D , which is given by:

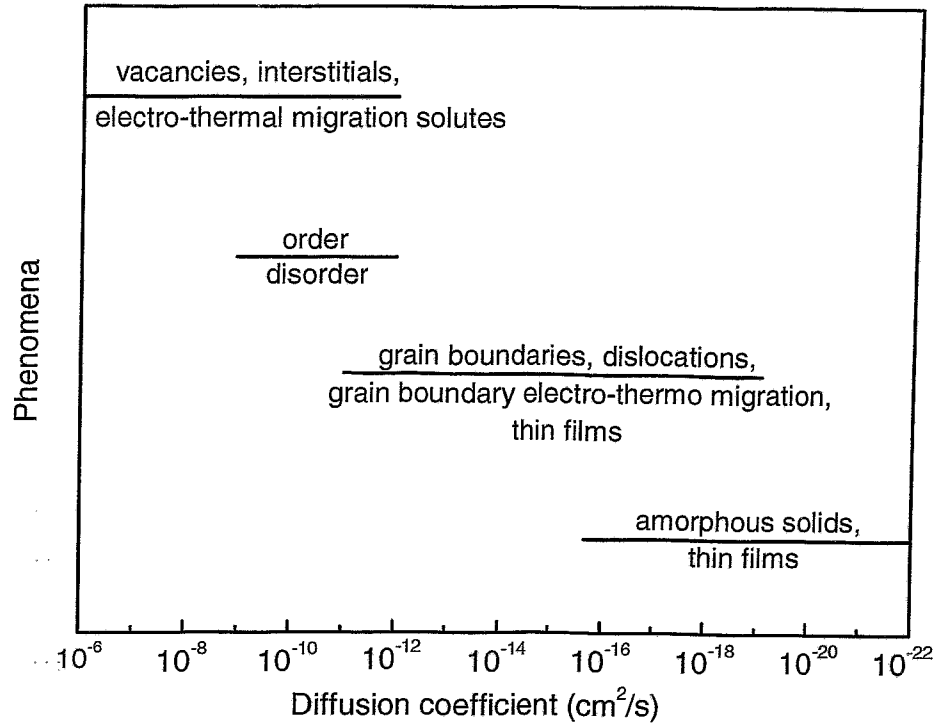


Figure 2.6: The magnitude of the diffusion coefficient for different mechanisms of diffusion, according to Ref. [119]. The temperature range is not specified.

$$D = D_0 \exp\left(-\frac{U}{kT}\right), \quad (2.11)$$

where D_0 denotes the diffusion constant and U the activation energy of diffusion, k the Boltzmann constant and T the temperature. Eq. 2.10 is known as first Fick's law, can be used only for a steady-state regime, i.e., when the flux is independent of time. In the time dependent case, for species that obey a conservation law and the diffusion coefficient is assumed to be independent of time the first Fick's law can be transformed to a second order partial differential equation known as second Fick's law:

$$\frac{\partial c(x, t)}{\partial t} = D \frac{\partial^2 c(x, t)}{\partial x^2} \quad (2.12)$$

Several analytical solutions exist for this equation corresponding to different initial and boundary conditions. These solutions express the dependence of the concentration on depth and time, which can be used to determine the value of the diffusion coefficient D . For i) constant surface concentration and ii) zero initial time the solution is given by the error function. The last indicates that the penetration depth varies with the square root of the time. If a constant surface recession is also considered as a boundary condition, than the evolution of the diffusion layer differs from the square root function of the time. This effect has been observed by Dimitrov et al. during plasma nitriding of steel [117, 118].

In practice, the kinetics of the diffusional growth depends also on the mechanism of diffusion. There are two common mechanisms by which atoms can diffuse in a crystal lattice. The diffusing atoms can take an interstitial location, if interstitial sites are vacant and if the radius of the diffusing atoms is smaller than that of the substrate atoms. The other mechanism is substitutional, where the diffusing atoms have a larger radius and they displace the substrate atoms and take their positions. However diffusion can also occur, if there are extended defects in the crystal such as dislocations, interfaces and grain boundaries. Usually the grain boundary diffusion is more pronounced compared to the diffusion within the grain, because the activation energy of diffusion along grain boundaries is lower than the activation energy in the lattice. The highest diffusivity in a solid state is observed for amorphous materials. Fig. 2.6 illustrates the range of the diffusion coefficients for the different mechanisms of diffusion, according to Ref. [119]. The diffusion scale in the figure is based on bulk process and the temperature range at which the diffusion coefficient are determined is not specified.

3 Experimental

3.1 Experimental equipment

The experimental system used for this work is schematically shown in Fig. 3.1. An ultrahigh vacuum chamber, 300 mm in diameter and 600 mm in height, houses three main units: A) a vacuum system, B) an ion source connected with a power supply and a gas flow control system and C) a sample manipulator equipped with a movable sample holder, a heater, and a thermocouple. A residual gas analyser and a Faraday cup are also located in the chamber. The description of these units and the analysis techniques, applied in this work, is given below.

3.1.1 Vacuum system

The chamber is evacuated to a typical base pressure of about 3×10^{-6} Pa by a 200 l/s turbomolecular pump coupled with a rotary pump and a 1800 l/s cryogenic pump. The total pressure in the chamber is measured by a pirani gauge head and a cold cathode gauge calibrated for nitrogen.

3.1.2 Ion source

The ion source is a hot filament ion source (Kaufman type), which was developed by the "Institut für Oberflächenmodifizierung" in Leipzig [120, 121]. Fig. 3.2 shows a sketch of the ion source and the power supplies. The ion source is housed in a cylindrical stainless steel body 70 mm in diameter and fitted with a ring of permanent magnets 95 mm in diameter. A tungsten filament is mounted on the cup at the rear side of the source. The inner discharge chamber is a tube made of stainless steel 40 mm in diameter and 50 mm in length. The ring anode is made of high purity graphite with an inner diameter of 30 mm. Two planar multiaperture grids of high purity graphite are used to extract and form a collimated beam of 30 mm in diameter. The screen grid with a thickness of 0.5 mm and the accelerator grid with a thickness of 1 mm are mounted 2 mm apart from each other.

The inner body of the ion source, the ring anode and the screen grid are held at a positive potential, which is the sum of beam voltage U_b and discharge voltage U_d given by a "beam" and a "discharge" DC power supply, respectively (see Fig. 3.2). This potential determines the ion energy and can be set to a maximum value of 2400 V. The potential of the filament is lower than the potential of body, anode and screen grid. The filament

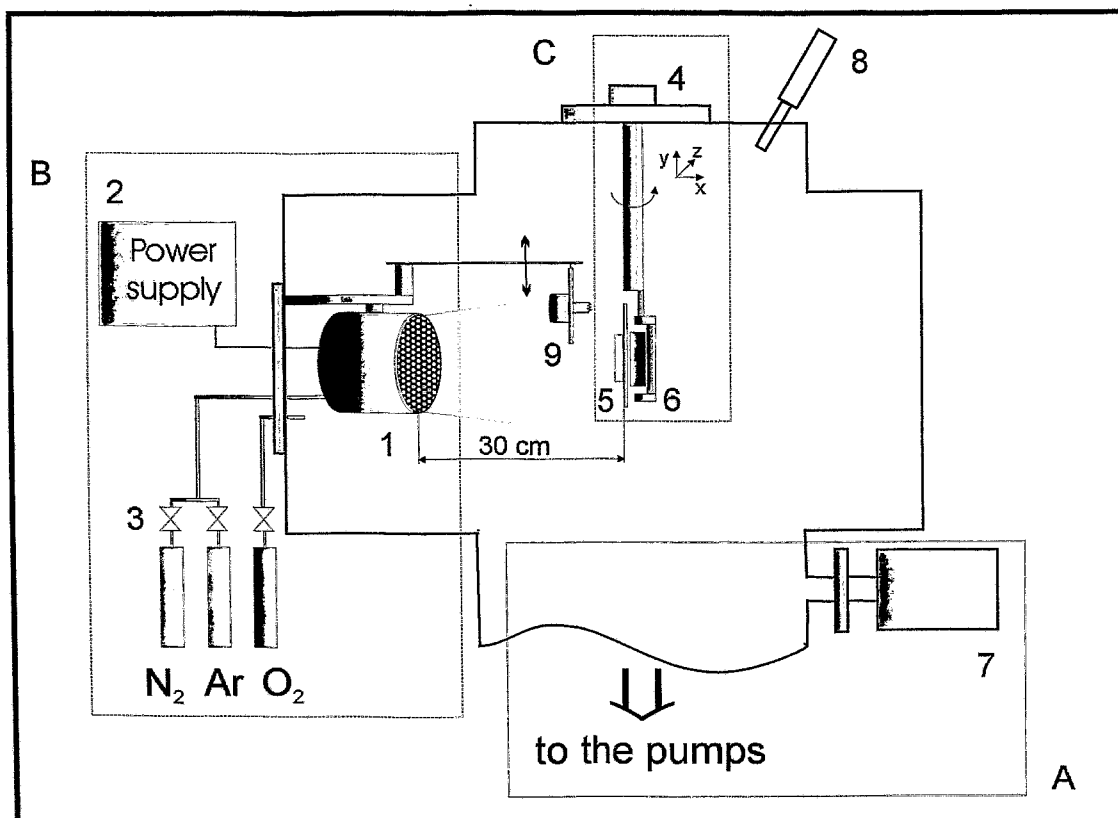


Figure 3.1: A sketch of the ion nitriding system showing: (1) the ion source, (2) the power supply of the ion source, (3) the gas flow controlling system, (4) the sample manipulator, (5) the movable sample holder, (6) the boron nitride heater, (7) the cryogenic pump, (8) the quadrupole partial pressure analyser and (9) the Faraday cup mounted on a movable holder used also as a shutter for the ion beam.

is heated by an AC power supply (filament voltage U_f) which controls the current of the discharge. Due to the difference in the potentials, the electrons which are emitted from the filament are accelerated to the ring anode. On their way the electrons dissociate and ionise the molecules of the gas injected into the ion source. The accelerator grid is held at a negative voltage U_{acc} with respect to the ground by an independent DC accelerator supply, which can be varied from - 500 V to 0 V. The potential difference between the screen and accelerator grids defines the ion optical parameters of the source.

Mass flow controllers type *AFC – 260*, *ASM* and a control unit type *247C*, *MKS* are used to select the gas flow through the ion source (Fig. 3.1). As process gas, argon and nitrogen with a purity of 99.999 % were used. The gas flux can be also injected directly into the chamber by a separate gas pipe situated near the source. In this way, for example, gas inlet of oxygen (99.999 %) was used in order to provide a different partial pressure of oxygen in the processing chamber.

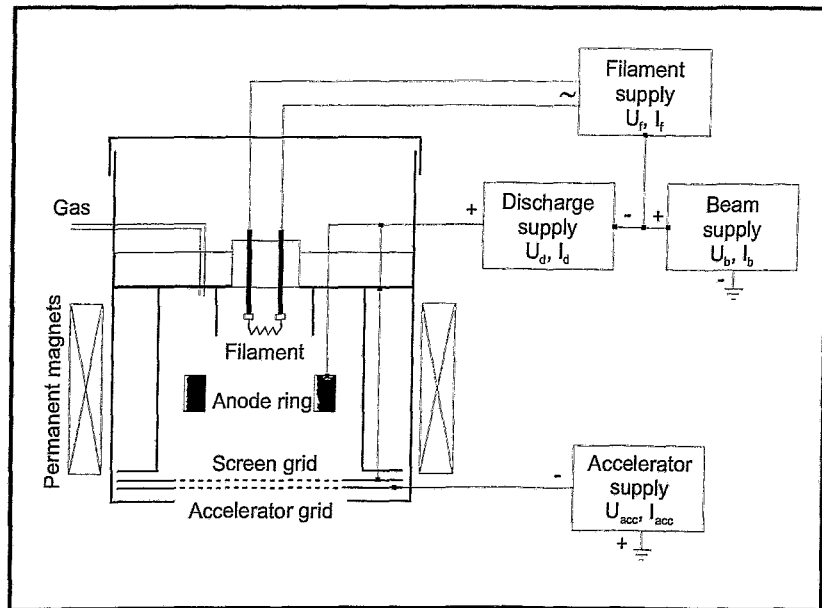


Figure 3.2: A sketch of the ion source with power supply.

3.1.3 Sample mounting, heating and temperature control

The sample can be mounted without breaking the vacuum in the chamber by a load lock and a transfer system. The sample manipulator enables xyz translation and has a rotational degree of freedom around the horizontal plane, which allows to turn the sample from the mounting position to the position of the ion beam. The manipulator also houses a boron nitride heater situated on the rear side of the movable sample holder, about 1 mm apart. The sample is heated to the desired temperature by adjusting the power applied to the boron nitride heater. Additionally, a hot filament mounted on the rear side of the Faraday cup and in front of the sample (see Fig. 3.1) is used in order to provide a similar heat to the sample as the heat caused by the ion beam. This prevents from a rapid increase of the temperature in the first minutes of the process. The temperature of the sample was measured by a thermocouple type K (Ni/CrNi) fixed into a hole drilled sideways in the sample. The thermocouple consists of two parts: one belongs to the movable sample holder and the other to the manipulator, which are fixed together during mounting the sample in the processing chamber. The sample temperature is monitored by *EUROTERM* 200.

3.1.4 Sample material and preparation

Drawn rods of 20 mm diameter from high-purity (99.999 %) polycrystalline aluminium were purchased from *Goodfellow*. From these rods, samples with 2 mm thickness were cut and mechanically polished to mirror finish. Al (111) oriented single crystal samples delivered by *MaTeck* were also used. Prior to the treatment all of the samples were ultrasonically cleaned in ethanol.

3.2 Analysis techniques

3.2.1 Diagnostics of the ions and neutrals

The current density of the ion beam was measured by a Faraday cup, which is mounted on the movable holder in front of the ion source and near to the sample (see Fig. 3.1). The radial ion current distribution was investigated by shifting the Faraday cup and measuring the current density at different positions. During the measurements the retarding field aperture of the Faraday cup was held at a negative voltage of 150 V in order to suppress secondary electrons generated at the cup. The incoming ion current reaching the cup was measured via an ampermeter.

The beam extracted from the ion source, was characterised by an energy selective mass spectrometer (*HIDEN EQP 500*), known as plasma monitor. For the measurements, the mass spectrometer was located 50 cm opposite the ion source in its axis of symmetry, while the sample manipulator was removed. A schematic view of the probe of the plasma monitor is shown in Fig. 3.3. The main units are: an extractor with a 100 μm in diameter aperture followed by an electron impact ion source and a 45° electrostatic energy analyser (0 to 1000 eV) matched to a quadrupole mass filter (0 to 500 amu) and a secondary electron multiplier (channeltron).

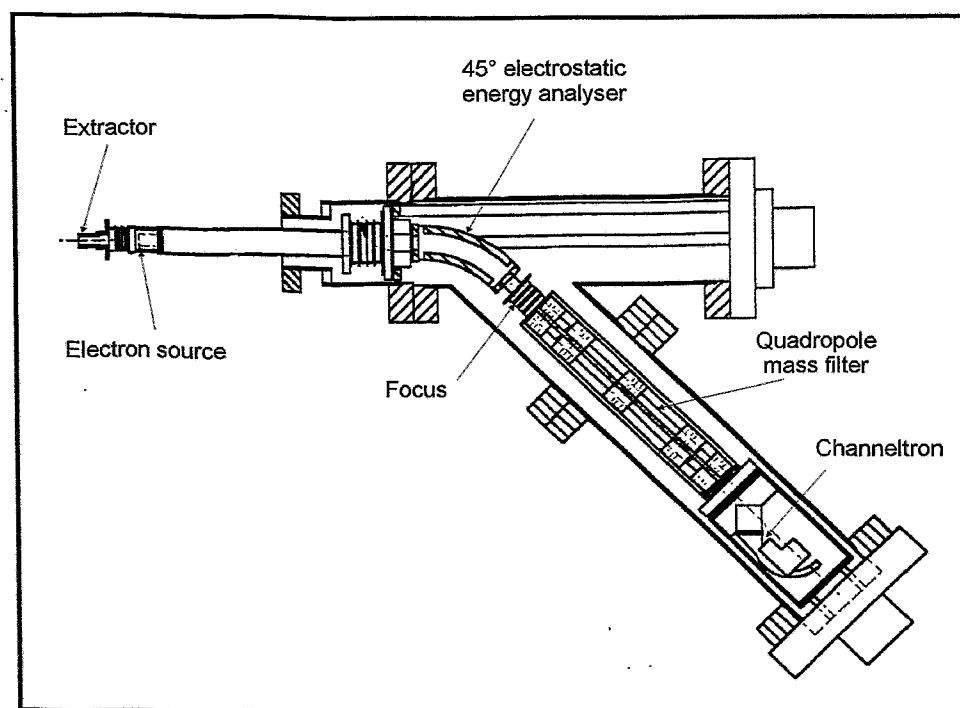


Figure 3.3: A scheme of the probe of the energy selective mass spectrometer (*HIDEN EQP 500*) used for characterisation of ion energy and beam composition.

The plasma monitor allows to determine mass and energy spectra of neutrals and ions. In the neutral detection mode, neutral species diffuse from the chamber into the mass spectrometer through the extractor. Neutral species are ionized by the integrated electron impact ion source. In the positive ion detection mode, ions pass through the orifice and are focused into the energy analyser selected according to their energy. The energy analyzer works at a constant pass energy, and an energy scan is performed by shifting the reference potential of the probe. The ionic species enter the quadrupole RF mass filter to be detected as function of their mass-to-charge ratio (m/z). Scanning the mass at fixed ion energy allows the acquisition of the various ionic species and scanning the energy at a fixed mass allows the measurement of the ion energy distribution (IED).

The mass dependence of the transmission of the probe was determined by comparing the electron-impact mass spectrum for He, CH₄, N₂ and Ar. The transmission was found to be constant up to 40 amu. For the IED measurement, the probe of the plasma monitor was correctly calibrated for each mass in order to get the optimum intensity. As the ion transmission of the probe is constant over the present range of mass (0 - 40 amu), the fraction of each ionic species can be estimated from the area of the ion energy distribution. This method has been proven to provide a more reproducible measurement of the beam composition, in contrast to the peak height of the ion mass spectrum.

The partial pressures of H₂, H₂O, N₂, O₂ and CO₂ were measured by a quadrupole partial pressure analyzer (*Balzers QMG 064*) mounted on the top wall of the chamber as shown in Fig. 3.1. Its working principle is similar to this of the plasma monitor at the neutral detection mode. Some of the molecules entering the analyzer are ionised by electrons emitted from a filament. Then, only the ions with specific mass-to-charge ratio are selected by a quadrupole mass filter (most of the ions are single charged). The quantity of ions at each mass is measured by an ion detector and the magnitudes of these signals are used to determine the partial pressures of the respective gases.

3.2.2 Surface analysis

3.2.2.1 Ion beam analysis

Ion beam analysis (IBA) was used for compositional surface analysis as a fast and quantitative method. It is based on the interaction between accelerated charged particles (ions) and the atoms of the investigated material. There are three main physical concepts of IBA:

1. The energy and momentum transfer between a fast particle and a nucleus of the substrate atoms leads to the concept of the kinematics of a single binary scattering event. It reveals the capability to determine atomic number or mass from the energy of the detected particle. The scattering process can be elastic or inelastic. It is elastic, if the total kinetic energy is conserved after the collision and the internal energy of the particles does not play a role. It is inelastic, if the scattering does not conserve the kinetic energy and atomic or nuclear excitation occurs.

2. The probability of a scattering event or a nuclear reaction leads to the concept of a scattering or reaction cross section, which gives the capability of quantitative analysis of the atomic composition. The scattering cross section can be calculated from the force

acting during the collision between the incident particle and the atom of the investigated material. If the force can be described as an unscreened Coulomb repulsion of the two positively charged nuclei, the cross section is given by the well known Rutherford formula [122]. If the incident particle has sufficient energy to overcome the Coulomb's barrier of the sample nucleus, than it feels the nuclear forces and its energy is transferred to the nucleus. The reaction cross section can not be expressed with a simple analytical function and has to be experimentally determined.

3. The average energy loss of an ion moving through a medium, which leads to the concept of the stopping power and to the capability of depth determination. The stopping power can be considered as known by applying semi-empirical data and the Bragg's rule [123].

Rutherford backscattering spectrometry (RBS)

Rutherford backscattering spectrometry (RBS) consists of irradiation of a sample by a light ion beam (normally H^+ or He^+) in the 1 - 3 MeV energy range. The incident ions are elastically backscattered from the atoms in the sample and further detected at a given scattering angle. A schematic diagram of the RBS experiment is shown in Fig. 3.4. The energy of the detected ion E_1 depends on the initial energy E_0 , the mass M_1 of the ion, the mass of the sample atoms M_2 and the depth where the collision takes place. For an atom at the surface, the ratio between the energy of the scattered ions and the initial energy, in the laboratory frame of reference, is given by the kinematic factor K :

$$K_{RBS} = \frac{E_1(x=0)}{E_0} = \left[\frac{\sqrt{M_2^2 - M_1^2 \sin^2 \theta} + M_1 \cos \theta}{M_1 + M_2} \right]^2, \quad (3.1)$$

where θ is the scattering angle. When the collision takes place at a certain depth x , there is an additional loss of energy during the way in and out of the sample ΔE_{in} and ΔE_{out} , respectively.

$$E_1(x) = K(E_0 - \Delta E_{in}) - \Delta E_{out} \quad (3.2)$$

The total number of ions that are recorded with an energy E_1 at a certain angle θ is given by the product of the ion fluence, solid angle of the detector Ω , area density of the atoms in the sample and the cross section σ . The Rutherford cross section is given by:

$$\frac{d\sigma_{RBS}}{d\Omega} = \left(\frac{Z_1 Z_2 e^2}{4E} \right)^2 \frac{4}{\sin^4 \theta} \frac{\left[\sqrt{M_2^2 - M_1^2 \sin^2 \theta} + M_2 \cos \theta \right]^2}{M_2 \sqrt{M_2^2 - M_1^2 \sin^2 \theta}} \quad (3.3)$$

The experimental RBS spectrum represents the number of scattered ions per energy interval. RBS is a technique mainly applied for depth profiling of heavy elements. A weak concentration of a light element can not be detected, if its energy distribution is overlapping with heavier components of the sample.

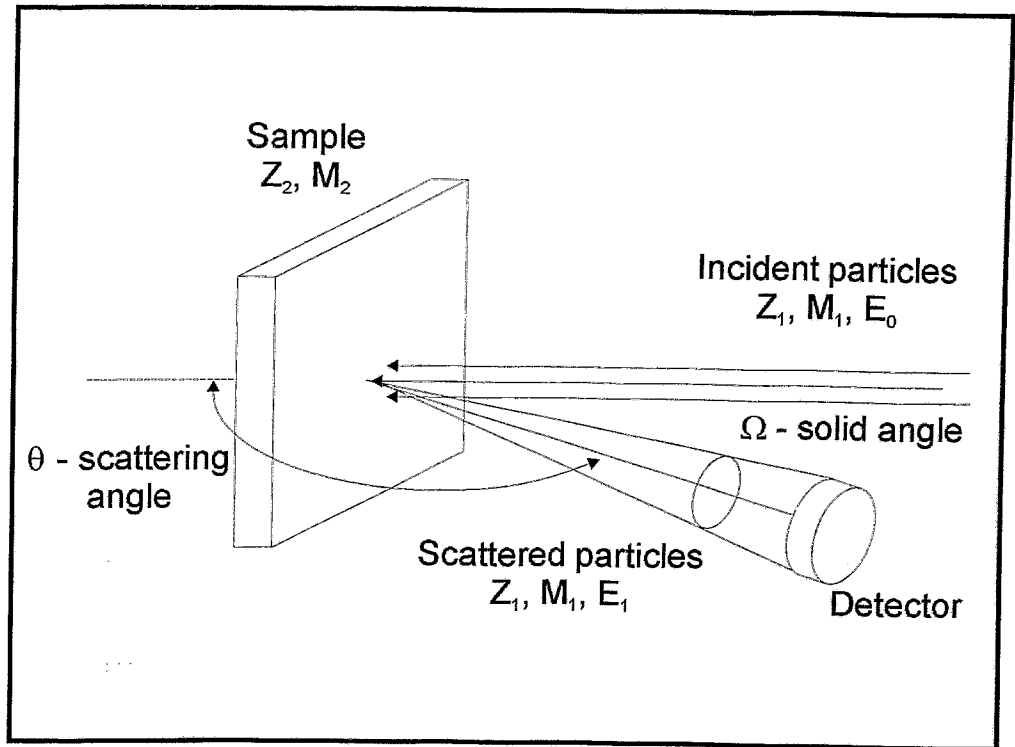


Figure 3.4: A schematic diagram of RBS scattering geometry.

For this study, RBS analysis was performed using 1.7 MeV $^4\text{He}^+$ ions provided by the Rossendorf Van de Graaff accelerator. The beam was incident normally on the sample surface and the backscattered particles were analysed by a silicon solid state detector, mounted at a scattering angle of 170° . The detector has a nominal thickness of $100\ \mu\text{m}$, a solid angle of 1.3 msr and an energy resolution of about 13 keV.

Elastic recoil detection analysis (ERDA)

Elastic recoil detection analysis (ERDA) uses a beam of particles heavier than the sample atoms of interest. The lighter sample atoms can be than knocked forward in the elastic collision and recoil out of the sample. In order to detect them, the sample is tilted at a grazing angle with respect to the direction of the incident beam. In difference to RBS, in ERDA several different types of atoms are detected (recoils and the forward scattered ions). Therefore, a separation between them is needed, which is realized by specific detectors. The equations for the analysis of ERDA are analogous as for RBS, considering that in this case atoms from the sample are detected:

$$K_{ERD} = \frac{E_1(x=0)}{E_0} = \frac{4M_1M_2 \cos^2 \phi}{(M_1 + M_2)^2}, \quad (3.4)$$

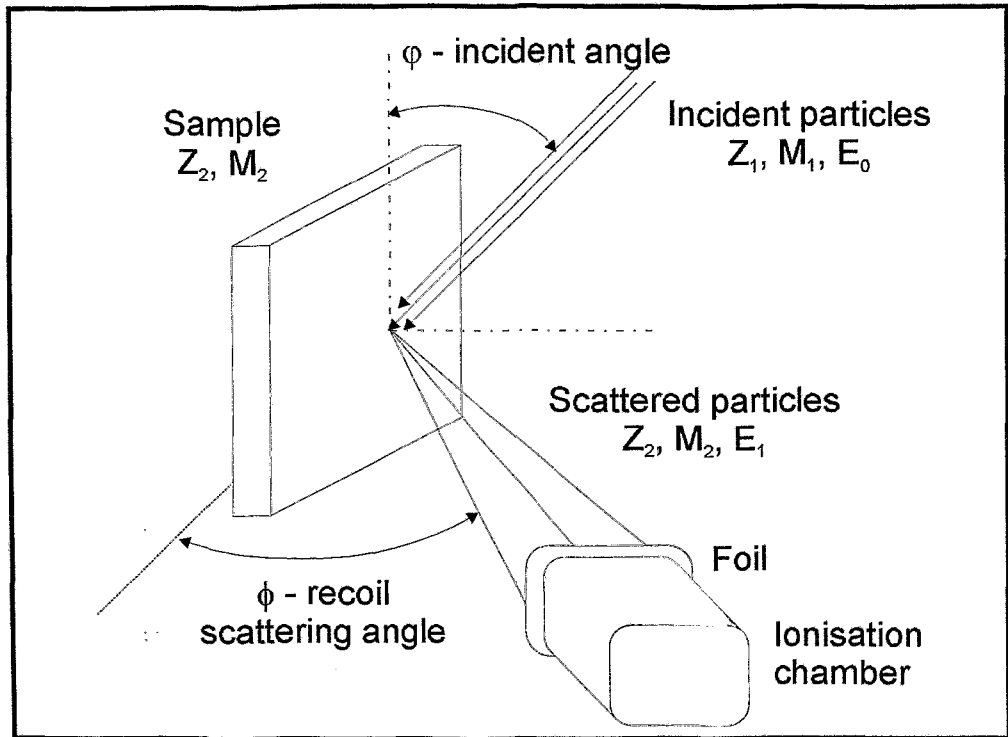


Figure 3.5: A schematic diagram of ERDA scattering geometry.

$$E_1(x) = K_{ERD}(E_0 - \Delta E_{in}^{ion}) - \Delta E_{out}^{recoil}, \quad (3.5)$$

$$\frac{d\sigma_{ERD}}{d\Omega} = \left(\frac{Z_1 Z_2 e^2 (M_1 + M_2)}{2M_2 E_0} \right)^2 \frac{1}{\cos^3 \phi}, \quad (3.6)$$

where ϕ is the recoil scattering angle with respect to the incoming beam. A schematic diagram of the ERDA experiment is shown in Fig. 3.5.

ERDA experiments were performed using a 35 MeV Cl^{7+} ion beam, supplied from the Rossendorf 5 MeV Tandem accelerator. For the different purposes of this work three configurations were used, which are briefly described below.

ERDA was applied for an in-situ real time investigation of the influence of oxygen partial pressure on the nitriding of aluminium described in section 4.2. The sample surface was simultaneously exposed to the nitrogen ion beam and to the Cl^{7+} beam. The analysing beam was directed at an incident angle of 17.5° . The recoiled atoms were detected at scattering angle of 35° by a $\Delta E - E$ ionisation chamber, known as "gas telescope", with a $1.2 \mu\text{m}$ thick entrance Mylar window and filled with isobutane at a pressure of 4×10^3 Pa. This detector has a large acceptance angle, which allows determination of a large number

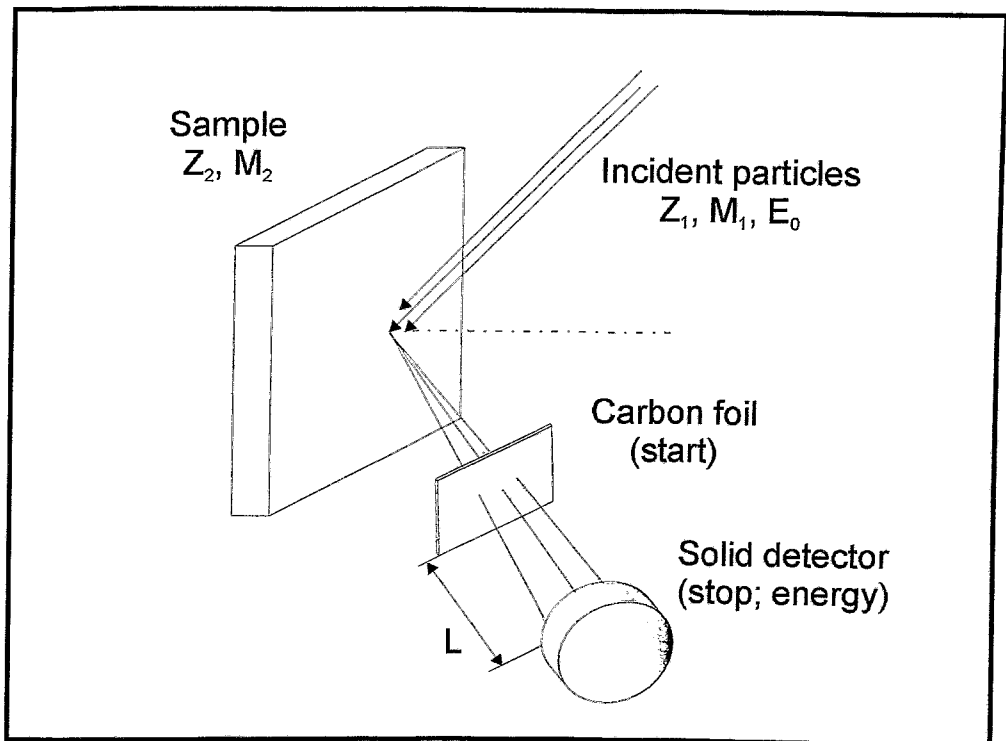


Figure 3.6: Experimental configuration for mass and energy dispersive TOF ERDA. The carbon foil and the solid state detector are separated by a flight part of $L = 1.05$ m.

of recoils in a short time. Sufficient energy resolution maintains by trajectory identification depth of large solid angle. This is a necessary condition for real time analysis, because the time for the measurement has to be comparable to the time of the process. The principle of the ionisation chamber is based on the specific energy loss, which the particles undergo over their trajectories inside the detector volume [124, 125]. In the $\Delta E - E$ ionisation chamber a transversal electrical field, perpendicular to the ion path is applied, which allows to determine the energy loss per distance beside the total energy E . This gives a possibility for determination of the atomic number Z using $\Delta E \sim Z$ and the kinetic energy E of the recoil atoms.

Some of the ERDA measurements were performed ex-situ at an incident angle of 15° and a scattering angle of 30° using a Bragg ionisation chamber with $1.2 \mu\text{m}$ Mylar entrance window, operated with isobutane at a pressure of 1×10^5 Pa. This detector uses a similar principle like the "gas telescope" but a longitudinal electric field, parallel to the ion path is applied. It also determines the atomic number and kinetic energy of the recoils. The Bragg ionisation chamber has a smaller acceptance angle compared to the "gas telescope" and therefore the trajectories of the recoils are better aligned, which results in a better energy resolution. More details are given in Refs. [125, 126].

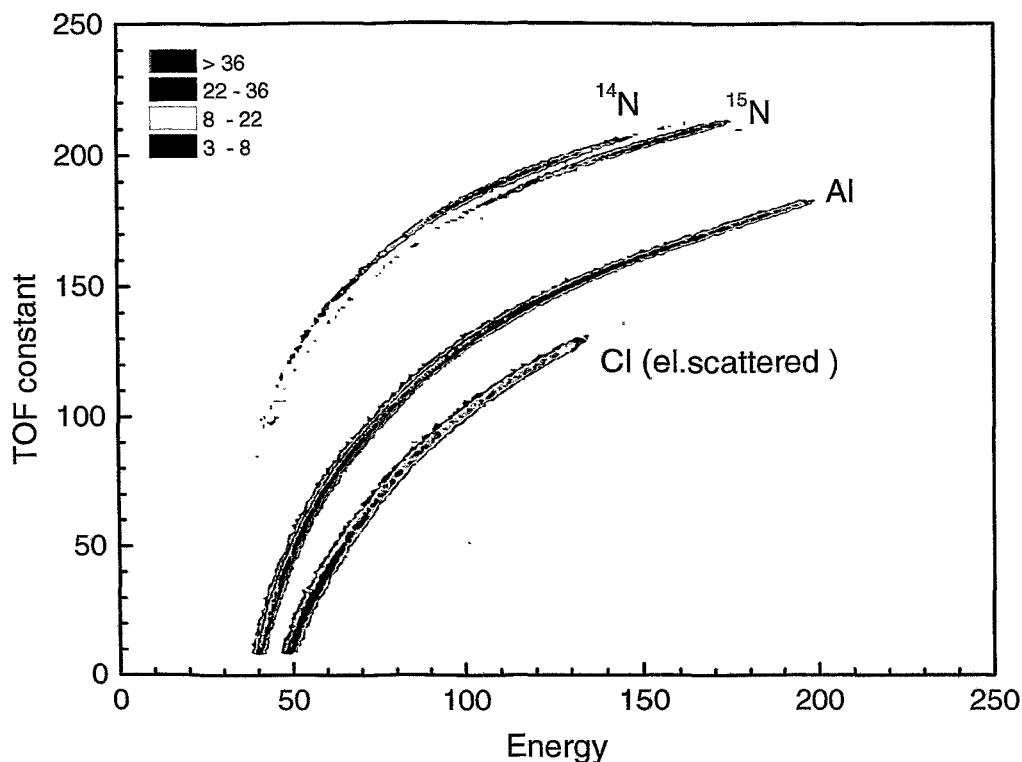


Figure 3.7: TOF ERDA spectrum obtained from an aluminium sample ion nitrided with ^{14}N and ^{15}N .

In the cases when the mass separation is of importance, the time-of-flight (TOF) ERDA technique [126] illustrated in Fig. 3.6 was used. It allows a simultaneous measurement of TOF and the kinetic energy of the recoils. The TOF is determined by signals obtained from a thin carbon foil (60 nm) situated near the sample and from a solid state detector after a flight distance L . The solid state detector provides both the signal for the "stop" time and the energy of the detected particle. Determination of the TOF allows a separation between recoils of different mass but with the same energy. An example of a TOF ERDA spectrum obtained from an aluminium sample ion nitrided with ^{14}N and ^{15}N is shown in Fig. 3.7. The spectrum consists of different branches corresponding to the specific atomic mass, in this case of scattered Cl and the recoils Al, ^{15}N , and ^{14}N . The colour scale in the figure represents the total number of recoils or scattered Cl. It has to be noted that for a fixed energy, heavier recoils give smaller TOF constant due to an inversion in the stop and start signals. The well separation between ^{15}N and ^{14}N demonstrates the mass resolution of the method. For a given mass, the atoms scattered from the surface have higher energy than those from the depth and therefore they appear at the right edge of each branch. Due to the small difference in mass between ^{14}N and ^{15}N their surface energies are very close. The different energy range of ^{14}N and ^{15}N recoils in Fig. 3.7 indicates that ^{15}N is situated only near the surface, while ^{14}N is found to be in the depth. The corresponding depth profile is shown and discussed in Fig. 4.11 b).

Nuclear reaction analysis (NRA)

In nuclear reaction analysis (NRA) the ion beam suffers an inelastic collision with the sample nucleus and nuclear reaction occurs. Generally, it results in an emission of reaction products, particles or gamma rays, which are further detected.

NRA was applied to analyse nitride layers which exceed the depth range of ERDA. The analysis was performed at the same experimental set up as used for RBS with 1.4 MeV incident energy of the deuterium (d) ions. The reaction $^{14}\text{N}(\text{d}, \alpha_1)^{12}\text{C}$ was used, where ^{14}N and d are the reactants, α_1 and ^{12}C are the products. An example of a typical spectrum obtained from an ion nitrided aluminium sample is shown in Fig. 3.8. It consists of elastically backscattered deuterium at low energies, followed by peaks which can be attributed to protons and α -particles of the excited high energy states as denoted in Fig. 3.8. The non identified peaks in the spectrum are most probably due to deuterium reactions with the aluminium atoms. The α peak used for the determination of nitrogen depth profiles appears at high energy (6669 keV) due to the high positive Q value (9146 keV) of the nuclear reaction. In order to suppress the background due to protons in the energy range of the used α_1 peak, the detector was operated at a reduced voltage of 15V.

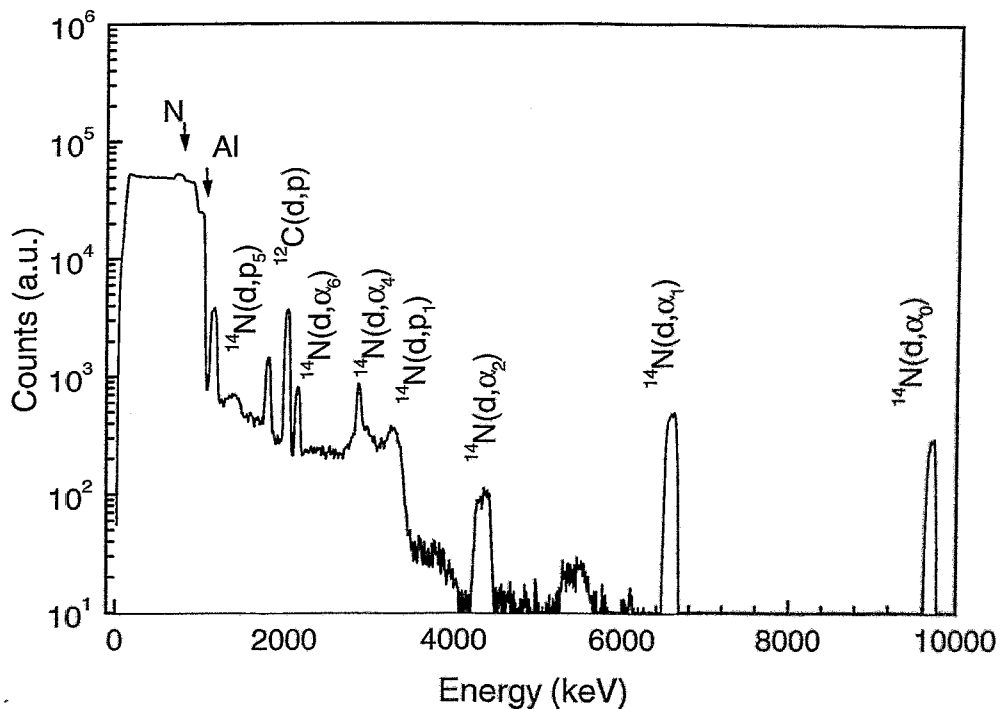


Figure 3.8: NRA spectrum for the ion nitrided aluminium sample obtained using the $^{14}\text{N}(\text{d}, \alpha_1)^{12}\text{C}$ reaction at 1.4 MeV incident energy and a scattering angle of 170° .

Evaluation of IBA spectra

In this study, the data obtained from IBA measurements were evaluated mainly by the WINDF 6.5 computer code [127]. The program uses a simulated annealing algorithm described in detail in Ref. [128]. For ERDA, the required input parameters are only the measured spectrum, the experimental conditions and the elements present in the sample (which for the most cases are known). For NRA, an additional information of the Q value of the reaction and the cross sections is needed. WINDF 6.5 can fit simultaneously all spectra collected from one sample which for instance can be RBS, ERDA, NRA, taking into consideration all information in a self-consistent way. An example for a fitted NRA spectrum is given in Fig. 3.9, where the part of elastically backscattered deuterium and the alpha peak resulting from the nuclear reaction are simultaneously fitted.

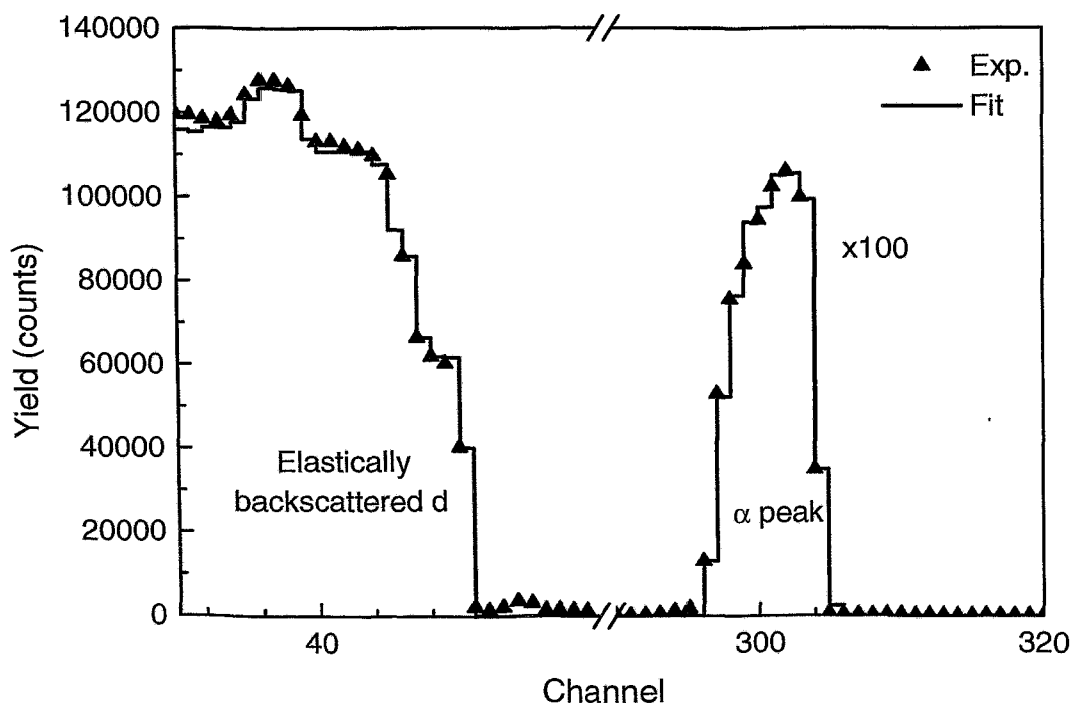


Figure 3.9: NRA spectrum (triangles) obtained from an ion nitrided aluminum sample and a data fit (solid line) performed by WINDF 6.5.

As a result, the program provides the so called "best simulated layer structure" shown in 3.10 a), which represents the number of simulated layers with their atomic fraction. Moreover, the program calculates "point-by-point" depth profiles shown in Fig. 3.10 b), where one concentration value is calculated from each data point in the spectrum by using the algorithm given in Ref. [129]. It has to be taken into consideration that the "point-by-point profile" is convoluted with the energy resolution. In general, the quantity obtained by IBA is the atomic fraction in dependence on the area density (at/cm^2) of the material being studied as a measure of depth. The obtained profiles can be transferred to a real depth scale by using the atomic density of the investigated material.

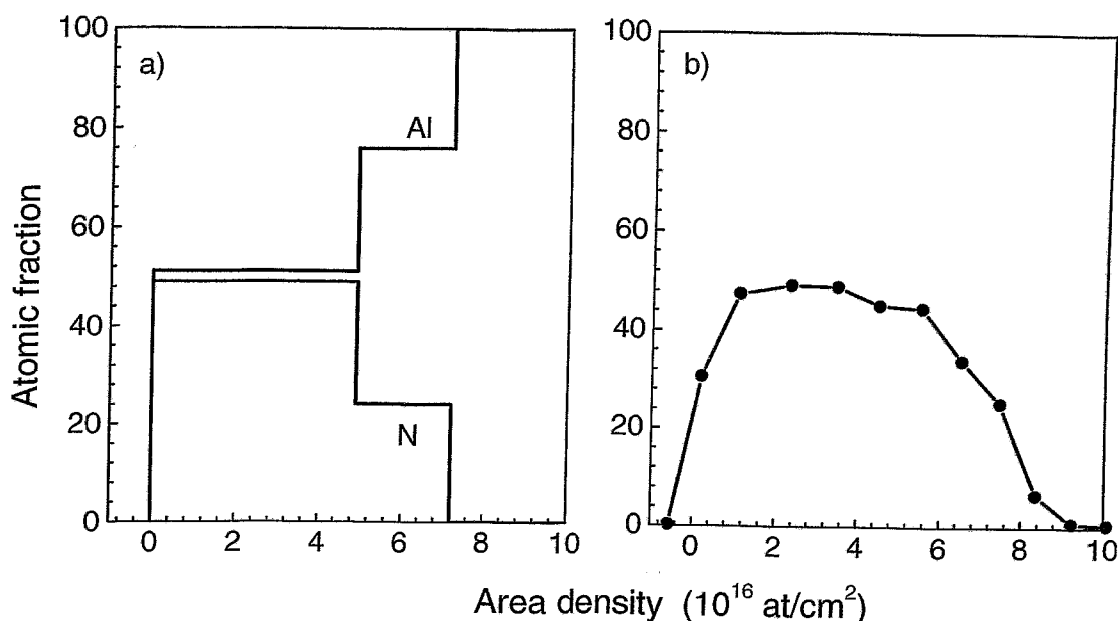


Figure 3.10: Elemental profiles calculated using the data fit shown in Fig 3.9: a) "best structure" profiles for nitrogen and aluminium and b) "point-by-point" profile for nitrogen.

Additionally RUMP [130] and the computer program ECPE (Element Concentration Profiles from ERDA) [131] were used to determine concentration depth profiles.

3.2.2.2 X-Ray diffraction

X-Ray diffraction (XRD) is a widely used, non-destructive technique for integral investigation of the crystal structure of materials. In the present study, XRD was applied for identification of the phase composition and structure analysis of the obtained nitride layers. The method is based on the diffraction of an incident X-ray beam from atomic planes of a crystal. The interference of coherent scattering planes causes intensity maxima of the diffracted radiation in dependence on the scattering angle. These maxima are known as diffraction peaks or also Bragg reflections. The scattering angle 2θ at which the diffraction peaks occur is given by the Bragg law:

$$2d \sin \theta = n\lambda, \quad (3.7)$$

where d is the lattice spacing (the planar distance in the crystal lattice), λ is the wavelength of the X-rays and n is the diffraction order. For a polycrystalline material with random orientation of the crystallites the diffraction does not depend on sample orientation.

XRD was performed at grazing incidence technique using CuK_{α} radiation with a mean wavelength of 1.542 \AA at an incident angle of 0.5 and 1° . This method is appropriate for investigation of thin layers, as obtained in this study. The principle of the XRD at grazing incidence is shown in Fig. 3.11. The X-ray beam is directed at a small incident angle $\theta_{in} \leq 1^{\circ}$ to the sample surface in order to limit the penetration depth and to enhance

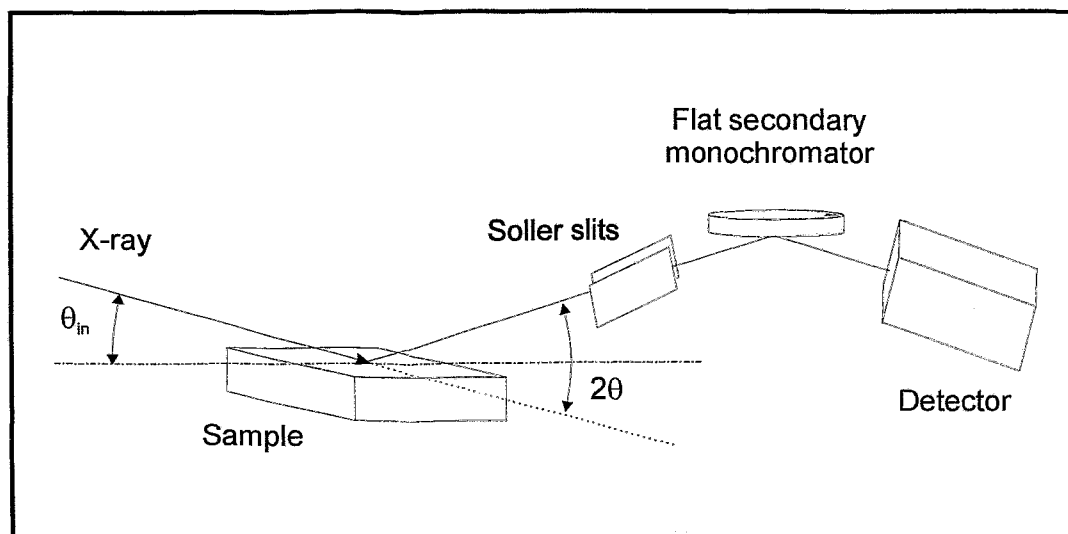


Figure 3.11: A schematic diagram of XRD at grazing incidence.

the diffraction peaks obtained from the layer with respect to these from the substrate. The detector is moved along a circle around the sample, where the angle between the incident beam and the detector is denoted as 2θ . The measured property is the diffracted beam intensity (I) in dependence on the diffraction angle. From the obtained diffraction pattern the following information can be obtained:

1. The distance between the crystal planes $\{hkl\}$ (h, k, l - Miller indices) in the lattice and the lattice constants can be calculated from the position of the diffraction peaks. The phases can be determined by comparison of these values with the data base of Powder Diffraction Files (PDF) [132]. If the intensity relations of the Bragg reflections are found to be different compared to the PDF data, then preferred crystallite orientation (texture) exists in the layer.

2. A shift of the diffraction angles from the tabulated positions is an indication that the crystal lattice is disturbed. Smaller θ -values show that the crystal lattice is expanded, whereas a shift of the diffraction angle to larger values corresponds to a compression of the lattice. From the shift of the diffraction angles in dependence on sample orientation, an information about macroscopic strains acting in the layer can be obtained.

3. From the broadening of the diffraction peaks of polycrystalline material the average grain size of the crystallites and microscopic strains in the layer can be determined. Diffraction peaks obtained from a perfect single crystal are very narrow. Broadening can occur due to three different reasons. First, due to the grain size, as crystallites with smaller size cause stronger broadening of the diffraction peaks. Second, there is a broadening due to microscopic strains, which describe the effect of local fluctuation of the macroscopic strain. And at last, there is always an effect of line broadening given by the experimental set-up.

To separate the effect caused by the grain size and microscopic strain, the "Integral width method" has been applied. In principle, it is a method for investigation of bulk materials, but it has been successfully used also for investigation of thin films [133, 134].

It considers that the integral width b of the diffraction peak can be determined as:

$$b = \sqrt{b_{\text{exp}}^2 - b_{\text{inst}}^2} \quad (3.8)$$

where b_{exp} is the experimentally measured width and b_{inst} is the width caused from the instrumental components. b_{exp} is defined as $\int I(s)ds/I(s)_{\text{max}}$, where $I(s)_{\text{max}}$ is the peak intensity and s denotes the scattering vector ($s = 2 \sin \theta/\lambda$). For the set-up used here b_{inst} is 0.25° . Furthermore, if the diffraction peaks are assumed to have a Gaussian shape, the following relationship holds:

$$b^2(s) = \frac{1}{C^2} + 2\pi \langle \varepsilon^2 \rangle s^2, \quad (3.9)$$

where $\sqrt{\langle \varepsilon^2 \rangle}$ is the microscopic strain and C is the average size of the coherently diffracting domains (crystallites). Since b^2 depends linearly on s^2 , by plotting b^2 versus s^2 a straight line is obtained with a slope equal to $2\pi \langle \varepsilon^2 \rangle$ and the intercept to $1/C^2$. In this way the average size of the crystallites and the microscopic strains can be determined separately.

For the analysis of the diffraction patterns the computer code PowderCell was used [135].

3.2.2.3 Electron microscopy

Electron microscopy is an analytical technique, which uses interaction between an electron beam and a solid state for an image formation as well as for structural and elemental characterisation of materials.

Scanning electron microscopy (SEM) uses secondary electrons or backscattered electrons that are emitted from a thick sample to image a surface. It is applied for studying the surface morphology or measuring particle sizes. The electron beam is scanned across the sample surface and the secondary electrons are produced as a result of the interaction. The intensity of the secondary electrons and thus the brightness of the image depends on the local surface relief and therefore the topography is represented on the image. Backscattered electrons are more sensitive to material (elemental) contrast. In this study, SEM was performed on a DSM 926 scanning electron microscope at 30 keV, which has a resolution of about 20 nm.

Transmission electron microscopy (TEM) images the electrons that pass through a thin sample (cross-section). These electrons are either scattered or they may remain unaffected. In result, a nonuniform distribution of electrons emerges from the exit surface of the sample, which contains the structural information. By selecting the direct beam, which passes through the sample a bright field (BF) image is formed. If one of the beams which is scattered at different angle is selected, then a dark field (DF) image is obtained. High resolution transmission electron microscopy (HRTEM) is a variation of TEM that uses phase-contrast imaging to provide a resolution of atomic scale. The main difference between the phase-contrast imaging and the other forms of TEM is the number of collected beams. While the BF and DF image uses only a single beam, the phase-contrast image requires selection of more than one. In general, the more beams are used, the higher is the resolution. In the present study, HRTEM was carried out on a Philips CM 300 electron microscope, operated at 300 kV.

3.2.2.4 Auger electron spectroscopy

Auger electron spectroscopy (AES) is another analytical technique, which uses the interaction between an electron beam and a solid state. It detects the Auger electrons emitted from the surface of the investigated material and it is applied for determination of the surface composition. In combination with sputter etching of the surface AES is also used for depth profiling. The physical principle of the method is shown in Fig. 3.12. Under the irradiation by the excitation electrons the atoms in the investigated material emit electrons from core levels. In the case of light elements, the electrons are emitted from the K shell. Then the atom relaxes via electrons with a lower binding energy dropping into the core hole. The energy difference ($E_{L_1} - E_K$) is converted to a third electron, which is emitted. The last is known as Auger electron. In the given example this is an electron from the L_2 level (see Fig. 3.12). In general, such transitions can take place between other atomic shells (K, L, M, ...) and they are labelled as KLL, LMM etc., in correspondence with the atomic levels involved. The kinetic energy of an Auger electron depends only on the involved atomic levels and not on the excitation source and it is used for identification of the element.

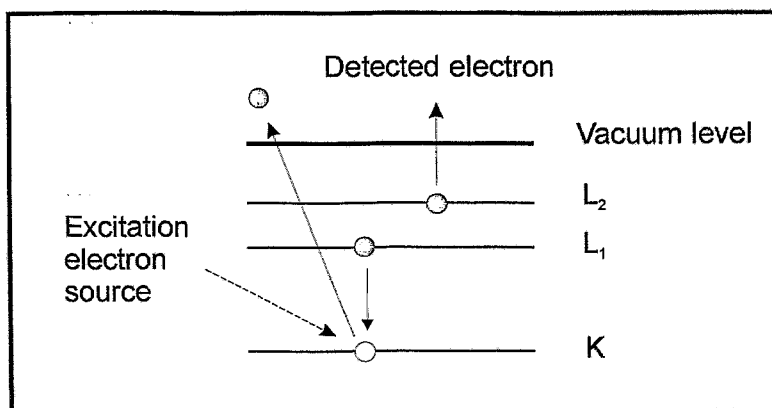


Figure 3.12: A diagram of an Auger transition.

In this study, AES was applied for determination of concentration depth profiles of layers exceeding the depth range of the ion beam analysis. The measurements were performed by a scanning Auger spectrometer MICROLAB 310F. For depth profiling argon ions with an energy of 3 keV were used. The final depth of the sputtered crater was determined by a profilometer DEKTAK and used to obtain the depth scale by assuming a constant sputter coefficient for the whole sputter time. For the quantitative evaluation of the atomic concentration relative sensitivity factors for aluminium and nitrogen were determined on the base of results obtained by ERDA.

4 Results and discussion

4.1 Characterisation of the ion beam and residual gas composition

4.1.1 Introduction

The performance of successful ion nitriding experiments requires a preceding study of the beam characteristics as ion current density, ion energy and uniformity. It is of essential importance to establish a stable operation regime for the ion source over long time. Knowledge about the identity and energy distribution of the ions reaching the substrate surface is also crucial for a better understanding and a quantitative determination of the ion nitriding process.

In this section, the dependence of the ion beam characteristics on the electrical parameters of the source and the gas flow will be discussed. The beam composition and ion energy is determined. In addition, the composition and the partial pressure of the gas in the experimental chamber is characterised.

4.1.2 Experiment and discussion

4.1.2.1 Ion current density and beam uniformity

The ion current density of the extracted beam depends on the gas flow through the ion source. Therefore, the dependence of the ion current density on the applied flow of N_2 was measured and the results are shown in Fig. 4.1 a). In the beginning of the obtained curve, a significant increase in the ion current density with increasing the N_2 flow is observed. This evolution is correlated to an increase of the plasma density in the source due to a higher possibility for collisions between electrons and neutrals. After a gas flow of about 1.2 sccm is approached, the ion current density becomes almost constant. At this regime the discharge in the source remains stable and a sufficient ion current density can be extracted without fluctuations. On the base of this investigation a gas flow of 1.3 sccm is chosen for the performance of the ion nitriding experiments in the present study. This value is in the beginning of the plateau in Fig. 4.1 a), which insures a stable operation of the ion source and long life time of the filament.

Experiments were carried out to characterise the operation of the ion beam current density with respect to the applied voltages. As mentioned in section 3.1.2, the ion current density can be set by the AC filament voltage (U_f) and DC anode discharge voltage (U_d) (see Fig. 3.2 on page 23). For the performance of ion nitriding experiments the discharge voltage is chosen to be constant ($U_d = 100$ V) and the desirable current density of the beam is adjusted by the filament voltage. An exactly reproducible setting of the ion current density by U_f is not possible because with increase of the working time the thickness of the filament decreases, which leads to a reduced electron emission. Nevertheless, the dependence and the operation range can be described. Fig. 4.1 b) shows a linear increase of the ion current density with increasing AC amplitude of the filament U_f . The maximum ion current density at which a stable beam is extracted is about 0.4 mA/cm².

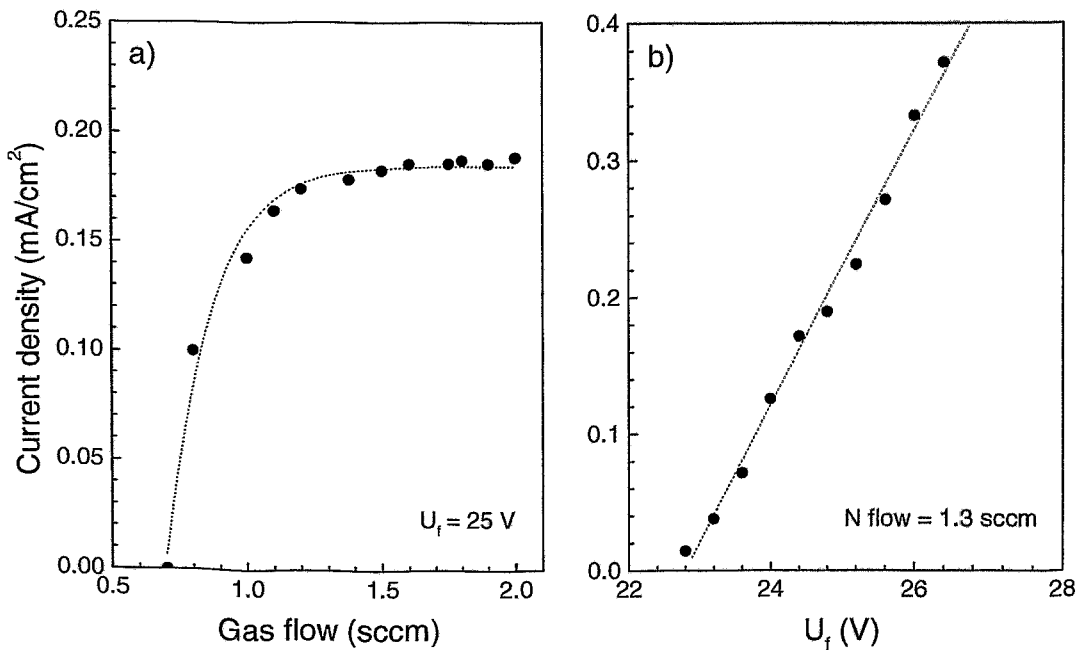


Figure 4.1: Ion current density as a function of a) gas flow of N_2 at $U_f = 25$ V and b) applied filament potential, measured in the centre of the ion beam at a gas flow of 1.3 sccm and $U_b = 1500$ V, $U_d = 100$ V, $U_{acc} = 300$ V.

The uniformity of the beam was investigated by measuring the radial distribution of the ion current at the sample position. For this purpose, different accelerating voltages (U_{acc}) were applied since the focusing of the ion beam depends on the difference in potentials between the accelerating grid and the inner body of the source. The obtained results are shown in Fig 4.2. For U_{acc} of 300 V the ion beam can be considered as uniform over the diameter of the sample (20 mm) within 5 %, while for 100 V the uniformity is within 10 %. Therefore, for the operation of the ion source an accelerating voltage of 300 V is chosen.

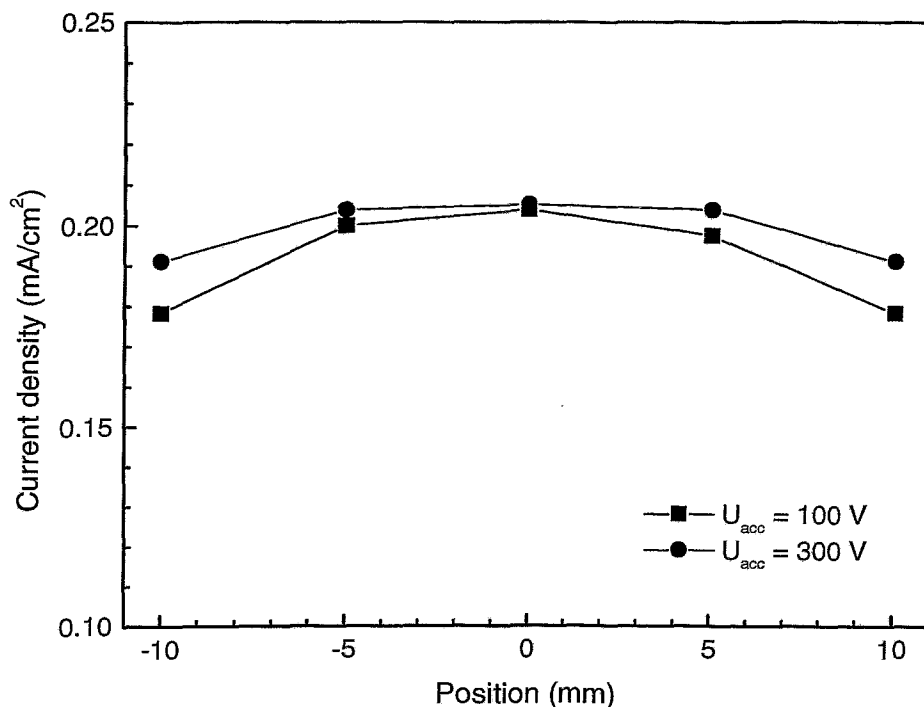


Figure 4.2: The radial distributions of ion density measured at the sample position for $U_{acc} = 100$ V and $U_{acc} = 300$ V.

4.1.2.2 Beam energy and composition

The ion beam composition was determined by an energy and mass selective spectrometer described in section 3.2.1. Fig. 4.3 shows a characteristic ion mass spectrum obtained during operation with a N_2 flow of 1.3 sccm, a current density of 0.2 mA/cm², a beam voltage of 300 V and a discharge voltage of 100 V. The main peak in the spectrum appears at 28 amu/e and indicates that the dominating ions in the beam are single charged nitrogen molecules N_2^+ . They are created by ionisation of the N_2 molecules in the discharge of the ion source. The second important peak in the spectrum is at 14 amu/e due to single charged nitrogen atoms N^+ , formed by the dissociative ionisation of N_2 molecules. A very small amount of doubly ionised N atoms (N^{2+}) is also detected as well as small satellites arising from a contribution of the singly ionised nitrogen isotope $^{15}N^+$.

The ion energy distributions (IEDs) of the dominating ionic species N_2^+ and N^+ were measured at 300 V beam voltage, 100 V discharge voltage and 0.2 mA/cm² ion current density. This analysis was performed at lower beam voltage than the values typically used for the ion nitriding of aluminium ($U_b = 300 - 2300$ V), since the plasma monitor allows a scan in energy up to 1.1 keV. Previous studies [120, 121] showed only a slight dependence of IED on the beam energy, thus it is reasonable to assume that the results obtained here are also representative for higher energies. Fig. 4.4 shows the measured IEDs, which consist of a single narrow peak with a full width at half maxima (FWHM) of about 10 eV. Consequently, the ion beam can be considered as quasi monoenergetic. The position of the peak corresponds well to the energy fixed by the sum of the beam and discharge

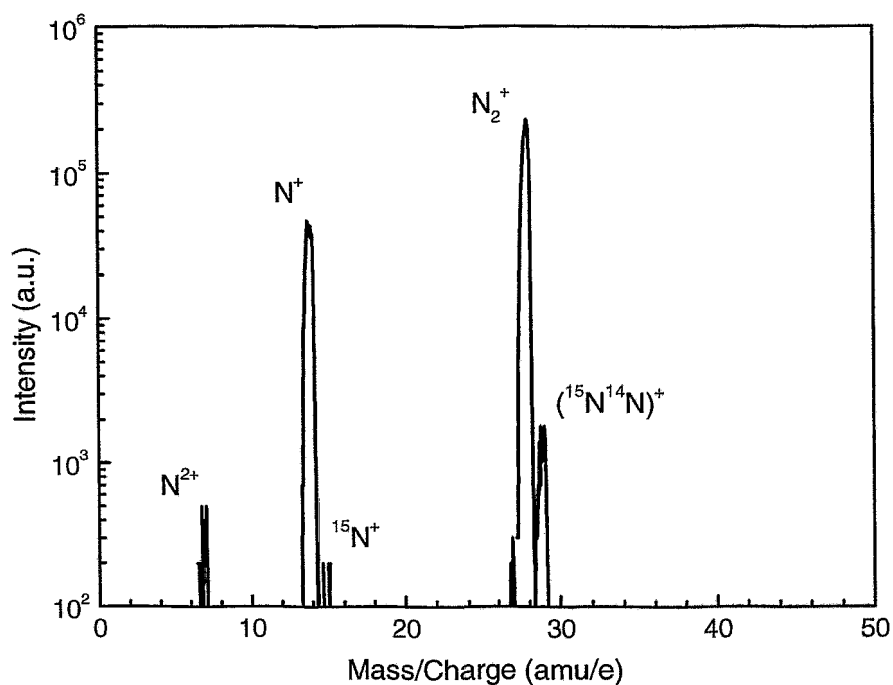


Figure 4.3: Characteristic ion mass spectrum of the reactive nitrogen ion beam. Beam parameters: 1.3 sccm N_2 flow, $U_b = 300$ V, $U_d = 100$ V and 0.2 mA/cm² ion current density.

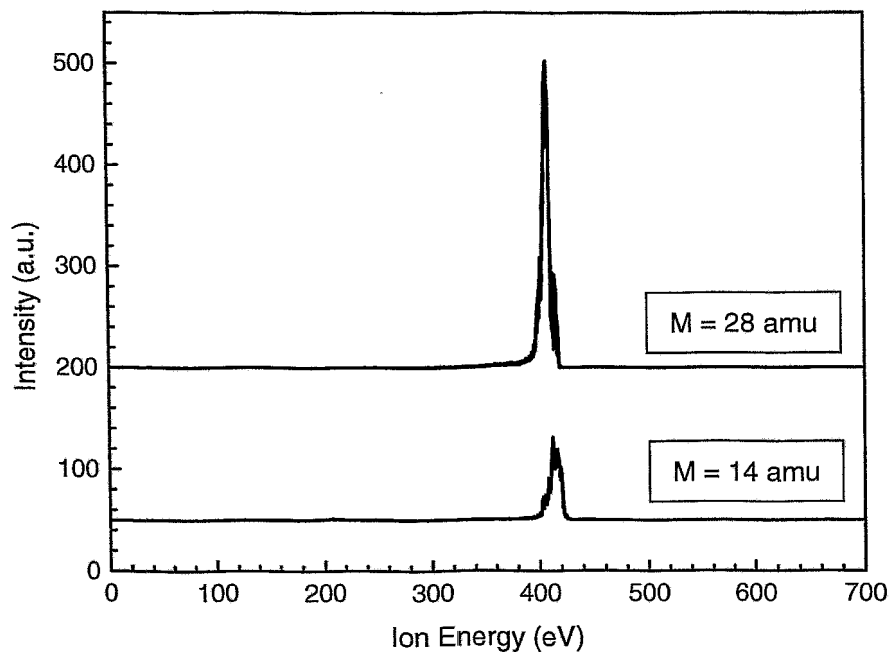


Figure 4.4: Ion energy distribution of N_2^+ and N^+ measured at $U_b = 300$ V, $U_d = 100$ V and an ion current density of 0.2 mA/cm².

voltages demonstrating a good control over the ion energy by the potentials applied to the source. As already mentioned above, the discharge voltage is chosen to be constant and equal to 100 V. Consequently, the control over the ion energy is realised by the beam voltage. Here it has to be noted, that further in this study as a process parameter the ion energy, i.e. the energy of the N_2^+ and N^+ which is equal according to Fig. 4.4, will be given. This is the value corresponding to the peak position in the IED.

The narrow IED and the small tail at lower energy indicate that collisions of ions with neutrals in the chamber can be neglected. This is in good agreement with the relation between the ion mean free path for ion neutral collision and the chamber dimensions. The mean free path $\lambda_{i/n}$ is defined as the average distance which an ion undergoes before colliding with a gas particle at a given pressure. It can be calculated by the following formula [136]:

$$\lambda_{i/n} = \frac{kT}{p\sigma}, \quad (4.1)$$

where k is the Boltzmann constant, T is the gas temperature, p is the gas pressure and σ is the collision cross section. Considering the two dominating collision processes: charge exchange and elastic collision, the last one can be expressed as [137]:

$$\sigma = \pi r^2, \quad (4.2)$$

where r is the radius of the molecule or atom. The cross section is calculated to be $1 \times 10^{-19} \text{ m}^2$ using the radius of the nitrogen molecule $1.09 \times 10^{-10} \text{ m}$, since the main neutral species present in the chamber are N_2 molecules (see below). Then, the ion mean free path for ion-neutral collisions is found to be about 11 m at a gas pressure of $3.8 \times 10^{-3} \text{ Pa}$ (corresponding to a gas flow of 1.3 sccm) at room temperature. This value is almost two orders of magnitude higher than the chamber dimensions and indicates a low probability for ion-neutral collision.

The fraction of N_2^+ and N^+ ions in the ion beam is determined as explained in section 3.2.1, after collecting a number of IEDs for both ionic species. The resulting fraction of N_2^+ and N^+ is found to be about 80 % and 20 %, respectively.

4.1.2.3 Gas composition

The partial pressures of H_2 , H_2O , N_2 , O_2 and CO_2 in the experimental chamber were measured using a quadrupole mass analyzer. Fig. 4.5 shows the results obtained at a nitrogen gas flow of 1.3 sccm when the discharge in the source is successively switched off and on. For both conditions, the main species are N_2 molecules due the diffusion of the process gas through the grids from the ion source to the chamber. The other species as H_2 , H_2O , O_2 and CO_2 are present in a very small amount with a partial pressure of few orders of magnitude less than the partial pressure of N_2 . When the source is on, an increase in the partial pressure of CO_2 is observed and a related decrease in the partial pressure of H_2O and O_2 . This effect indicates that H_2O and O_2 , dissociate in the source discharge, induce etching of the graphite parts of the ion source (the ring anode and grids), thus producing CO_2 . However, the partial pressure of CO_2 remains at a very low value ($4 \times 10^{-6} \text{ Pa}$), therefore the pollution in the chamber can be considered as negligible.

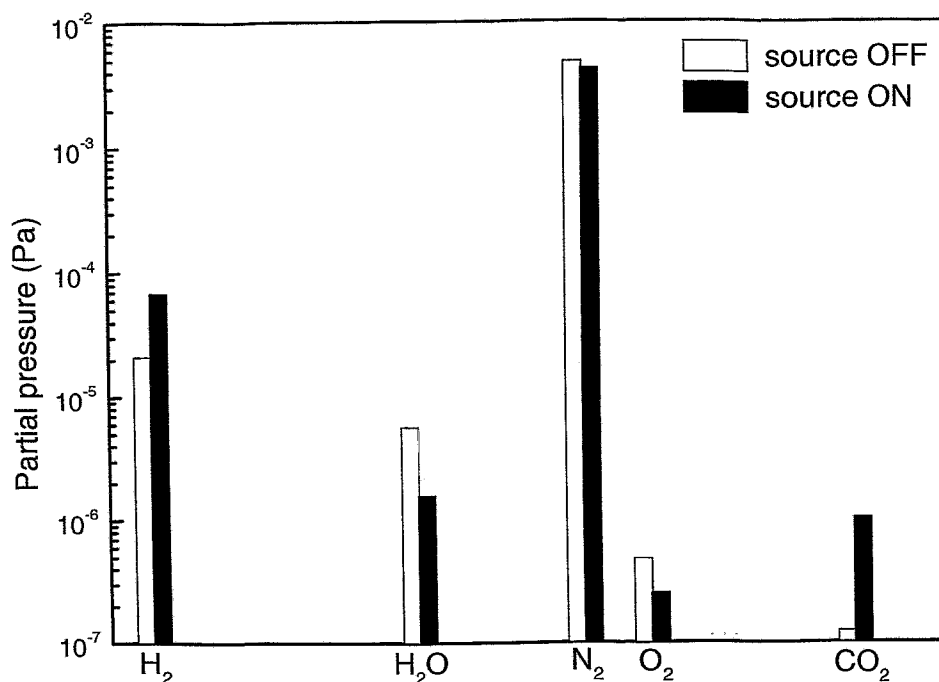


Figure 4.5: Partial pressure of H₂, H₂O, O₂, N₂ and CO₂ in the experimental chamber when the ion source is switched on and off.

It has to be taken into consideration that an atomic nitrogen is also present in the chamber, since it is created by the dissociation of N₂ in the ion source. The atomic nitrogen may play an important role for the nitriding of aluminium and therefore knowledge about its flux at the sample position is required. Under the present experimental conditions, the atomic nitrogen could not be detected by the plasma monitor. However, its flux and partial pressure can be estimated in a simple way. At an electron temperature of 4 eV in the discharge of the ion source [138], the production rate of nitrogen atoms is about 2 times higher than the production rate of nitrogen ions, according to the rate coefficients of dissociation and ionisation [139, 140], respectively. The effective sticking of the ion source walls can be assumed to be close to one for both species, since both will most probably be reemitted into the source volume as nitrogen molecules. Therefore, the flux of atoms through the extraction system is about two times higher than the flux of ions. The directed ion flux has a mean diameter of about 8 cm at the sample position. In contrast, the atomic nitrogen flux is approximately distributed according to a cosine distribution, when a plane emission is assumed. The extraction grids will cut a large fraction of the atomic nitrogen, but little influence the formed flux into the direction of the sample. Thus, less than about 3 % of the total flux falls onto the above area of 8 cm diameter. Following the above given consideration, the flux of atomic nitrogen j_N is estimated to be about 7×10^{13} at/cm²s for the ion current density of 0.2 mA/cm², mostly used in this study, with a corresponding ion flux of 1.25×10^{15} ions/cm²s. Then, the partial

pressure of atomic nitrogen p_N can be calculated from:

$$j_N = \frac{p_N}{\sqrt{2\pi mkT}}, \quad (4.3)$$

where k denotes the Boltzmann constant, T the gas temperature and m the mass of the nitrogen atom. Then, p_N is about 2×10^{-9} Pa, which indeed is too low to be detected by the plasma monitor, since it will be also reduced due to the conductance of the extraction aperture (refer to section 3.2.1).

4.1.3 Summary

The influence of applied voltages and gas flow through the ion source on the beam parameters as ion current density, energy and uniformity was investigated. The optimum value of N_2 gas flow is found to be 1.3 sccm. A stable operation of the ion source is achieved. The ion current density and energy are independently controlled by the filament and the beam voltage, respectively. A sufficient uniformity of the ion beam over the sample area is achieved at an accelerating voltage of 300 V. The analysis of the ion beam shows that it consists of N_2^+ and N^+ ions with a composition of about 80 % and 20 %, respectively. The ion beam can be considered as a quasi monoenergetic, since the ion energy distribution of both N_2^+ and N^+ consists of a single narrow peak. The shape of the ion energy distributions identifies a low possibility for ion-neutral collisions, which is in good agreement with the estimation of the ion mean free path.

The analysis of the gas composition shows that the main molecules present in the experimental chamber are N_2 . The partial pressures of H_2 , H_2O , O_2 and CO_2 are very low and therefore the impact of this contamination on the process of aluminium ion nitriding can be neglected. The flux of atomic nitrogen at the sample position is estimated to be about 20 times lower than the flux of ions.

4.2 The role of the oxide layer

4.2.1 Introduction

As already mentioned in section 2.1.2, the main difficulty for nitriding of aluminium and its alloys at low energies is related to the natural affinity of aluminium to react with oxygen and thus to form a dense surface oxide layer. Arai et al. [10] have shown that this layer acts as a barrier against nitriding and successful nitriding of aluminium takes place, if the surface oxide is removed prior to nitriding. Furthermore, it is of crucial importance to prevent a continuous reoxidation during the nitriding process itself. Parascandola et al. [11] have recently shown that the interplay between the oxide growth rate and oxide removal rate due to sputtering is a key parameter for successful ion nitriding. If the oxide growth rate is lower than the sputter rate, the surface oxide layer is essentially removed and nitridation takes place. In the opposite case, the surface oxide layer grows and can either hamper or stop the nitriding process. The thickness of the surface oxide layer becomes stationary when the two rates balance.

In this section, experiments of ion nitriding of aluminium at different oxygen partial pressure are reported. The aim of this investigation is to define a critical partial pressure of oxygen for the present ion beam parameters, under which aluminium can be successfully nitrided.

4.2.2 Experimental results

The experiments were performed in two steps. First, the samples were heated up to a temperature of $500\text{ }^{\circ}\text{C} \pm 15\text{ }^{\circ}\text{C}$ at three different values of oxygen partial pressure of $3 \times 10^{-3}\text{ Pa}$, $3 \times 10^{-4}\text{ Pa}$ and $3 \times 10^{-5}\text{ Pa}$ for 10 min. Second, ion nitriding was performed at an ion energy of 1.6 keV and an ion current density of 0.2 mA/cm^2 for 15 min. The samples were analysed before and during ion nitriding by in-situ real time ERDA. Fig. 4.6 shows the time resolved depth profiles of oxygen (left) and nitrogen (middle) obtained for the three different partial pressures of oxygen. The colour scale gives the atomic density of oxygen (blue) and nitrogen (green). The nanometer depth scale is calculated by assuming stopping powers of stoichiometric Al_2O_3 and AlN and using their standard densities. The right graphics in Fig. 4.6 show the corresponding evolution of the oxygen and nitrogen area densities. The time at which ion nitriding starts is indicated with $t = 0$. The negative time corresponds to the time when the samples are exposed to the influence of oxygen pressure only. Fig. 4.6 shows that originally all samples exhibit a native surface oxide layer with an oxygen area density of about $6 \times 10^{16}\text{ Oat./cm}^2$ (notice that the scale of oxygen is multiplied 5 times). The corresponding oxide layer thickness is calculated to be about 8.5 nm by assuming stoichiometric Al_2O_3 . It can be seen that at the highest oxygen partial pressure of $3 \times 10^{-3}\text{ Pa}$ the surface oxidation results in a significant increase in the oxygen area density up to $1.8 \times 10^{17}\text{ O at./cm}^2$. For the two other oxygen partial pressures only a slight increase is detected. Upon starting the ion nitriding ($t = 0$) the oxide layer thickness is reduced for all three cases.

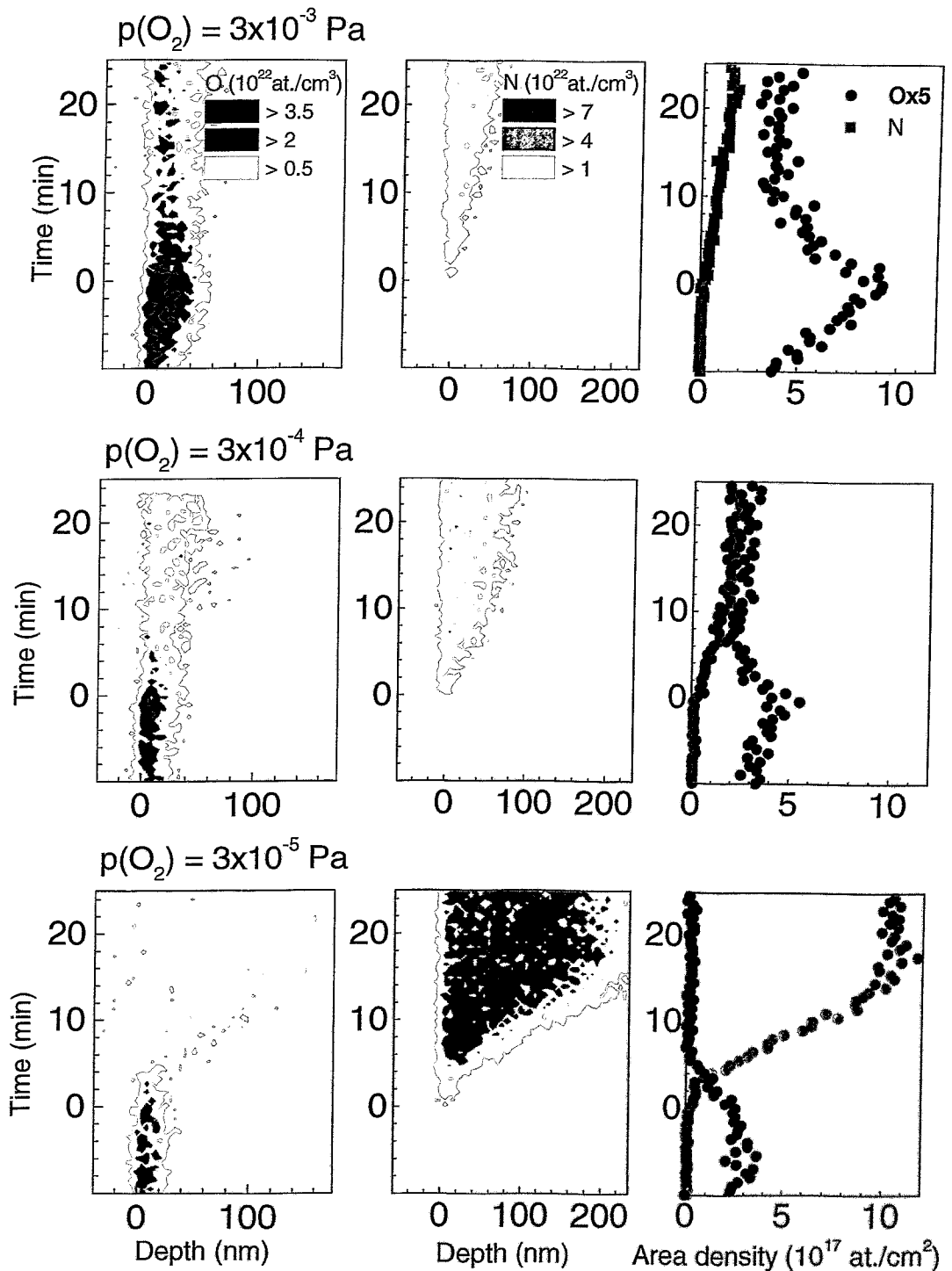


Figure 4.6: Time evolution of oxygen (left) and nitrogen (middle) depth profiles and their corresponding area densities (right) obtained by in-situ real time ERDA at different oxygen partial pressure. The colour scale gives the respective atomic density.

At partial pressures of 3×10^{-3} Pa and 3×10^{-4} Pa a stationary oxide layer establishes after about 10 min from the beginning of the ion nitriding with an area density of 8×10^{16} O at./cm² and 6×10^{16} O at./cm², respectively. At the lowest partial pressure of oxygen ($p(O_2) = 3 \times 10^{-5}$ Pa) the surface oxide layer is essentially removed within 5 min. The influence of the surface oxide layer on the nitriding kinetic of aluminium can be clearly seen in the corresponding nitrogen depth profiles. When the oxide layer is present on the surface, the nitrogen profiles have a limited thickness and area density below the stoichiometric value of AlN. When the surface oxide layer is successfully removed, the incorporation rate of nitrogen is much higher than in the other case. The nitride grows at a constant rate for the time of the ion nitriding (15 min).

4.2.3 Discussion

The oxide layer forms on the surface of aluminium due to adsorption of oxygen atoms from the residual gas in the experimental chamber. The oxide growth rate (r_{GR} , in terms of the oxygen area density per unit of time) depends on the flux of oxygen atoms arriving at the surface. For simplicity, it is assumed that the oxygen is delivered only as molecular oxygen and that the sticking coefficient of oxygen to the sample surface is one. Then, according to the kinetic gas theory the r_{GR} is given as:

$$r_{GR} = \frac{2p(O_2)}{\sqrt{2\pi mkT}}, \quad (4.4)$$

where $p(O_2)$ denotes the oxygen partial pressure, k the Boltzmann constant, T the temperature and m the mass of the oxygen molecule. Applying Eq. 4.4 the growth rate of the oxide layer is calculated for the three different partial pressures of oxygen at room temperature and using the mass of the oxygen molecule (5.3×10^{-26} kg). The obtained results are listed in Table 4.1.

On the other hand, the oxygen removal rate (r_{SR}) is caused by sputtering and depends on the ion energy and flux according to:

$$r_{SR} = j_0 \int f(E) Y_O(E) dE, \quad (4.5)$$

where j_0 denotes the incident ion flux, $f(E)$ the ion-energy distribution and $Y_O(E)$ the sputtering yield of oxygen. TRIDYN simulations were performed to estimate the sputtering yield of oxygen due to nitrogen implantation in stoichiometric Al₂O₃ at an incident angle of 17.5° (this is the angle at which ion nitriding and in-situ real time ERDA were carried out, as described in section 3.2.2.1). The sputtering yield of oxygen is calculated to be 0.32 for N⁺ and 0.27 for N₂⁺. Considering the N₂ and N₂⁺ fractions in the beam and the ion current density of 0.2 mA/cm² the total removal rate of oxygen is found to be equal to 7.4×10^{14} Oat./cm²s. This value is listed together with the values for r_{GR} in Table 4.1. It can be seen that at the lowest oxygen partial pressure of 3×10^{-5} Pa the oxide growth rate is lower than the sputtering rate. This is in good agreement with the

experimental results, which show that the surface oxide layer is successfully removed. For the two other partial pressures of oxygen, the oxide growth rate is higher than the sputtering rate. As the experiment shows, in this case a stationary oxide layer is formed on the surface which decreases the incorporation rate of nitrogen. The obtained area density of the stationary surface oxide layer is also shown in Table 4.1. The results for r_{GR} and r_{SR} together with the experimental data confirm that the interplay between oxide growth rate and oxide removal rate is a key parameter for successful ion nitriding. It is observed that the surface oxide layer acts as a barrier against nitriding. This phenomenon can be explained by comparing the oxide layer thickness (≈ 8.5 nm) with the mean projected range of N^+ (≈ 6 nm) and N_2^+ (≈ 4 nm), see Fig. 2.3 on page 13. This reveals that the nitrogen is implanted in the oxide layer, where most of the aluminium atoms are bound in oxide. Then, nitrogen atoms might remain in solid solution, diffuse into the bulk where free aluminium is present, or diffuse back through the surface in the gas phase. The experiment shows, that a very small amount of nitrogen is found behind the oxide layer, therefore it can be concluded that most of the nitrogen which has been implanted in the oxide leaves through the surface.

The experiments presented here, clearly demonstrate the benefit of surface bombardment on the nitriding process, The energetic ions can cause cleaning of the surface oxide, formed during the nitriding. This result explains the need to bias the sample during plasma nitriding as reported in Ref. [70].

$p(O_2)$ (Pa)	r_{GR} (O at./cm ² s)		r_{SR} (O at./cm ² s)	Stationary layer (O at./cm ²)
3×10^{-3}	1.6×10^{16}	>	7.4×10^{14}	8×10^{16}
3×10^{-4}	1.6×10^{15}	>	7.4×10^{14}	6×10^{16}
3×10^{-5}	1.6×10^{14}	<	7.4×10^{14}	none

Table 4.1: The growth rate (r_{GR}) and the sputter removal rate (r_{SR}) of the surface oxide layer obtained from Eqs. 4.4 and 4.5 for different partial pressures of oxygen. The area density of the stationary oxide layer measured by ERDA is also shown.

4.2.4 Summary

In this section, the influence of the surface oxide layer on the nitriding of aluminium has been investigated. The obtained results clearly show that when an oxide layer is present on the surface it hampers the incorporation of nitrogen in the aluminium substrate. If the sample surface is free of oxide, successful nitriding of aluminium takes place at a constant growth rate. It is confirmed that the thickness of the oxide layer is controlled by the interplay between the oxide growth rate due to adsorption of oxygen atoms from the residual gas and the oxide removal rate due to sputtering by the ion beam. The

bombardment with low-energy ions induces cleaning of the surface oxide simultaneously to the nitriding process. The Eqs. 4.4 and 4.5 can be used for determination of the critical oxygen partial pressure in dependence on ion energy and current density. For the used here ion energy of 1.6 keV and current density of 0.2 mA/cm², the critical partial pressure of oxygen is found to be 3×10^{-5} Pa. All further experiments performed in this study were carried out at an oxygen partial pressure equal or lower than this value in order to insure the successful nitriding of aluminium.

4.3 Nitrogen incorporation and loss

4.3.1 Introduction

During ion nitriding of aluminium, nitrogen ions are supplied to the surface by the ion beam. Considering the ion-solid state interaction, one part of the incident ion flux is incorporated into the substrate and an other part is lost due to backscattering and sputtering. The nitride layer growth depends on the amount of incorporated nitrogen atoms. On the other hand, sputtering induces surface erosion, thus reduction of the nitride layer thickness. Knowledge about the influence of the ion beam parameters as ion energy and current density on the nitrogen incorporation and loss is important for an understanding of the nitriding process and for achieving control over the nitride layer growth. Furthermore, during ion nitriding a gas-solid state interaction can also take place, since the substrate surface is simultaneously exposed to the influence of neutrals. Nitrogen adsorption from the residual gas, additionally stimulated by the ion bombardment, may contribute to the incorporation of nitrogen. Moreover, desorption of nitrogen from the solid state to the residual gas may enhance the nitrogen loss.

In this section, studies of nitrogen incorporation and loss due to sputtering and backscattering are presented. As it will be discussed in section 4.5, where the kinetics of aluminium ion nitriding is studied, the experiments described here are performed at such a substrate temperature and nitriding times for which the nitride layer growth is controlled by the rate of nitrogen supply. At these conditions, diffusion does not play a limiting role for the nitride layer growth, thus does not affect the mechanism of nitrogen incorporation and loss. The results presented here are subdivided into two subsections considering i) ion-solid state and ii) gas-solid state interaction.

4.3.2 Ion-solid state interaction

4.3.2.1 Experimental results

For an investigation of nitrogen incorporation and loss in terms of ion-solid state interaction two series of experiments were carried out. First, samples were ion nitrided at different ion energies varying from 0.4 keV to 2.4 keV with an ion current density of 0.2 mA/cm² for 20 min. Second, nitriding of aluminium was performed at a constant ion energy of 1.6 keV with two ion current densities of 0.1 mA/cm² and 0.2 mA/cm² and for different time increasing from 5 min up to 30 min. Prior to the nitriding, the native oxide layer was removed by sputtering with Ar⁺ at an ion energy of 1.6 keV and an ion current density of 0.2 mA/cm² for 10 min. The substrate temperature was 350 ± 20 °C during the Ar⁺ sputtering and the nitriding process. After treatment, the samples were cooled down in the vacuum chamber. The obtained nitride layers were analysed by NRA. TRIDYN simulations were performed to estimate the sputtering and backscattering yields of nitrogen.

The measured total amount of nitrogen atoms incorporated in the aluminium substrate is shown in Fig. 4.7 by squares as function of the ion energy. The amount of nitrogen is presented in units of at./cm², which is a direct result from the NRA spectra analysis obtained by the WINDF code. The corresponding thickness of the nitride layers calculated

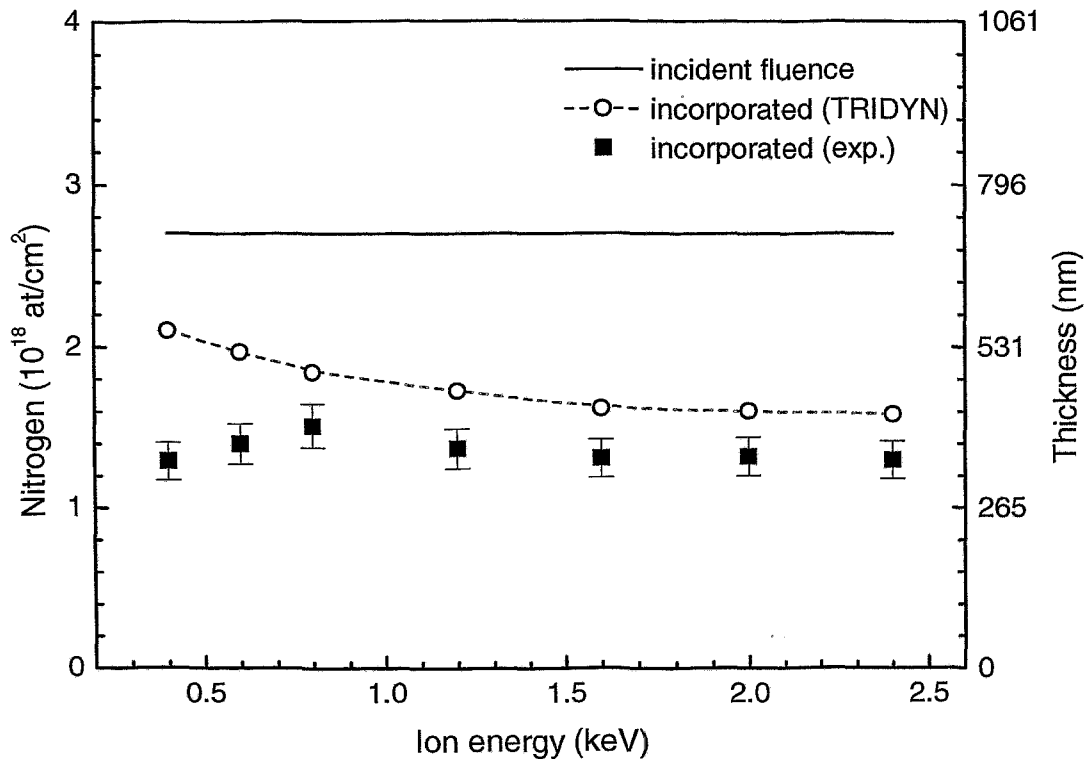


Figure 4.7: Dependence of nitrogen incorporation on the ion energy determined by NRA (squares) and calculated by TRIDYN (circles). Process parameters: ion current density of 0.2 mA/cm², nitriding time 20 min and substrate temperature 350 °C. The incident fluence of nitrogen is shown by the solid line.

from the total amount of incorporated nitrogen and the atomic density of the nitride layers (determined in section 4.7.1) is also shown on the right axis. The incident flux of nitrogen is estimated to be 2.25×10^{15} at./cm²s using the fraction of N₂⁺ and N⁺ ions in the beam and the ion current density of 0.2 mA/cm². The flux of nitrogen loss can be determined from the difference between the incident flux of nitrogen atoms and the flux of incorporated nitrogen as:

$$\dot{j}_{N \text{ loss}} = \dot{j}_{N \text{ incident}} - \dot{j}_{N \text{ incorp.}} \quad (4.6)$$

Here the loss of nitrogen is considered to be due to sputtering and backscattering only:

$$\dot{j}_{N \text{ loss}} = \dot{j}_{N \text{ sp}} + \dot{j}_{N \text{ bs}} \quad (4.7)$$

The incident fluence of nitrogen atoms supplied to the surface for a time of 20 min is 2.7×10^{18} at./cm², which is represented in Fig. 4.7 by a solid line. The amount of nitrogen, which is lost during the ion nitriding process can be experimentally determined by applying Eq. 4.6 using the amount of incorporated nitrogen measured by NRA. On the other hand, the nitrogen loss due to sputtering and backscattering can be theoretically estimated on the base of computer simulations. The results obtained by TRIDYN as a

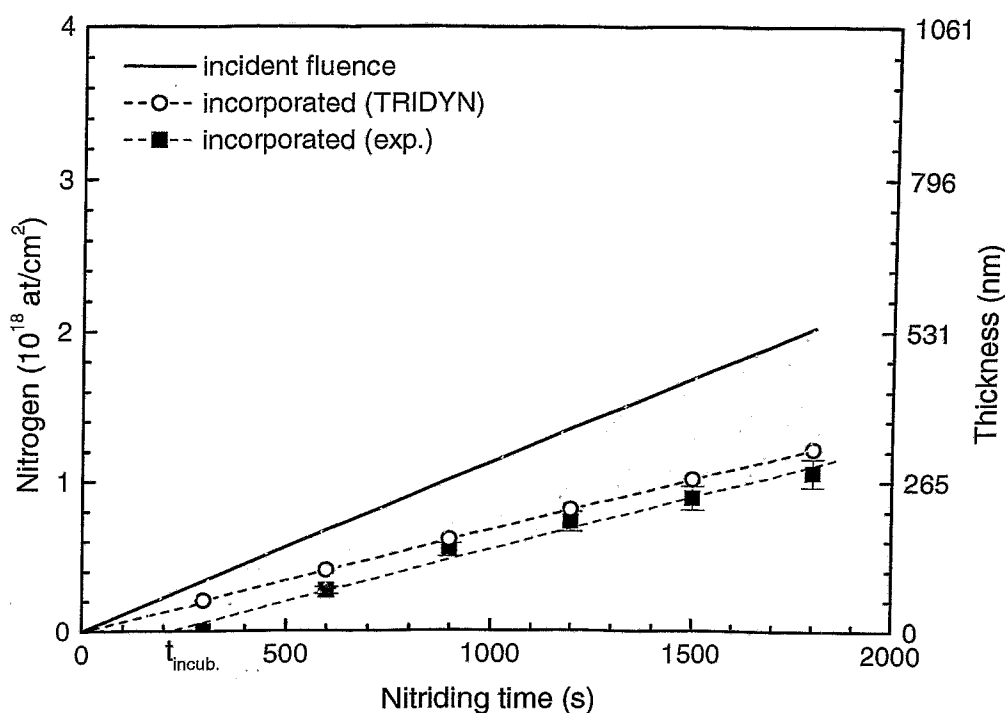


Figure 4.8: Time dependence of incident nitrogen fluence (solid line), total amount of incorporated nitrogen determined by NRA (squares) and calculated by TRIDYN (circles). Process parameters: ion energy of 1.6 keV, ion current density of 0.1 mA/cm 2 and substrate temperature of 350 °C. The amount of nitrogen loss is grey patterned.

function of the ion energy are presented in Fig. 2.4, on page 16. One has to be aware, that the simulation is performed for atomic nitrogen ions. The correct estimation of the sputtering and backscattering yields requires consideration of N_2^+ and N^+ fraction in the beam, as well as the fact that the molecular ions dissociate upon impact on the surface and each nitrogen atom takes the half of the energy. Then, the sputtering and backscattering fluxes can be calculated applying Eq. 2.8. From these and using the known flux of incident nitrogen, the amount of nitrogen which is expected to be incorporated in the substrate can be calculated. The results are shown in Fig. 4.7 by circles. They are in reasonable good agreement (within 20 %) with the experimentally determined amount of incorporated nitrogen for beam energies higher than 0.8 keV. A discrepancy is observed at lower beam energies with an estimated amount of incorporated nitrogen higher than the experimental values.

The results obtained from the experiments performed at a constant ion energy are shown in Figs. 4.8 and 4.9 as a function of the ion nitriding time for ion current densities of 0.1 mA/cm 2 and 0.2 mA/cm 2 , respectively. The total amount of nitrogen atoms incorporated in the aluminium substrate is shown by squares. A linear dependence on time is observed. In Figs. 4.8 and 4.9 it can be seen that the nitriding process has an incubation time ($t_{incub.}$) of about 4 min and 2 min, respectively. The fluence of incident nitrogen arriving at the surface is estimated for each nitriding time and shown with a solid line in

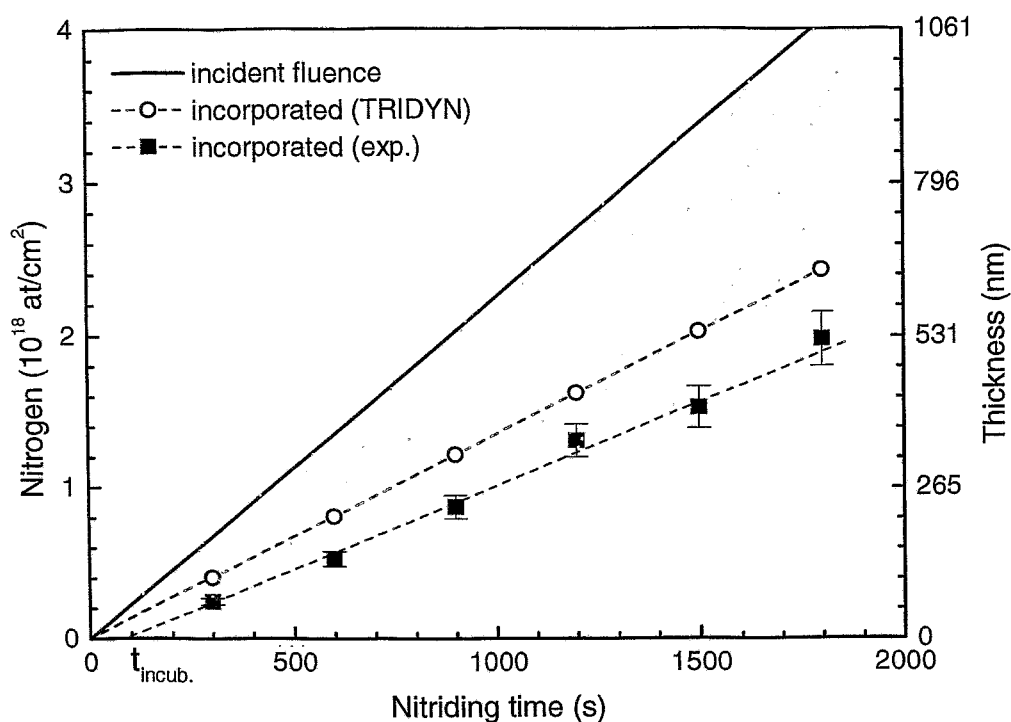


Figure 4.9: Time dependence of incident nitrogen fluence (solid line), total amount of incorporated nitrogen determined by NRA (squares) and calculated by TRIDYN (circles). Process parameters: ion energy of 1.6 keV, ion current density of 0.2 mA/cm 2 and substrate temperature of 350 °C. The amount of nitrogen loss is grey patterned.

Figs. 4.8 and 4.9. The corresponding amount of lost nitrogen is the difference between the incident fluence and the incorporated nitrogen, which is grey patterned. Furthermore, by applying TRIDYN the total sputtering yield of nitrogen is found to be 0.36 and the fraction of backscattered nitrogen is estimated to about 4 % of the incident fluence of nitrogen. Thus, the computer simulations result in 60 % incorporated nitrogen, which is shown in Figs. 4.8 and 4.9 by circles. Again, the experimentally and theoretically determined amount of incorporated nitrogen are in reasonably good agreement.

4.3.2.2 Discussion

The results presented above illustrate that the mechanism of nitrogen incorporation and loss can be successfully described in terms of ion-solid state interactions for the present range of nitriding times and substrate temperature. In this approach, only nitrogen supply by the ion beam and nitrogen loss due to sputtering and backscattering are considered. The experimentally determined amount of incorporated nitrogen per unit of time is found to be a stationary value, indicating that the flux of incident nitrogen and the flux of nitrogen loss are in balance during the process. A comparison between the sputtering and backscattering yields estimated by binary collision computer simulations reveals that the nitrogen loss is dominated by sputtering. Fig. 2.4 in section 2.2.1 shows that the sputtering yield is in the range from 0.16 up to 0.4 nitrogen atoms per incident particle,

whereas the backscattering yield is only in the range from 0.03 to 0.05. The results obtained by the simulations are consistent with the experimental data. A discrepancy is observed only at low ion energies of 0.4 keV and 0.6 keV. Such a difference may be the result of the influence of the surface oxide layer as discussed in the previous section. It has to be noted that the experiments presented here were performed at an oxygen partial pressure of about 3×10^{-5} Pa, which was determined as a critical value for an ion energy of 1.6 keV. Similar to the results of Fig. 2.4, the sputtering yield of oxygen is lower at ion energies of 0.4 keV and 0.6 keV. Thus, a stationary oxide layer may be formed, which as seen in Fig. 4.6, decreases the incorporation rate of nitrogen.

Figs. 4.8 and 4.9 show that for the present experimental parameters, the growth kinetics of the nitride layer is linear. Moreover, the thickness of the layer is proportional to the ion current density of the beam. Consequently, control over the growth rate can be achieved by the ion current density taking into account the reduction due to nitrogen loss caused by sputtering and backscattering.

The observed incubation time $t_{incub.}$ has also to be discussed here. This period can be as well related to the existence of a thin surface oxide layer built up during the time when the source is switched off in order to change from Ar to N₂ gas (about 2 min). Until the oxide layer is not sputtered again (now by the nitrogen beam) there is not noticeable growth of the nitride layer. This is consistent with the observed different incubation time, since the beam with higher ion current density induces higher sputtering rate of oxygen and thus shorter $t_{incub.}$. On the other hand, a certain time for formation of a critical size of AlN nuclei may be necessary, after which a significant growth of the nitride layer takes place.

4.3.3 Gas-solid state interaction

4.3.3.1 Experimental results

In principle, adsorption can contribute to the process of nitrogen incorporation, since the performed in section 4.1 analysis of the gas composition in the experimental chamber shows that a high amount of N₂ molecules is present. The impinging flux of N₂, estimated from the N₂ partial pressure and applying Eq. 4.3, is about one order of magnitude higher than the ion flux arriving at the surface. Moreover, it has to be taken into consideration that the ion bombardment can enhance the reaction between N₂ and aluminium. In order to test the role of N₂ molecules on the nitriding process the following experiment was performed. First, the surface oxide layer was sputtered by an argon ion beam at a current density of 0.2 mA/cm² and an ion energy of 1.6 keV for 10 min. Then, simultaneously to the Ar⁺ beam a gas flux of N₂ was directly introduced in the chamber from a separate gas inlet. A N₂ gas flow of 1.3 sccm was applied in order to provide a neutral flux of N₂ similar to this during the ion nitriding process, where the ion source was operated with 1.3 sccm N₂. The experiment was carried out for 20 min. After treatment, the sample was analysed by NRA, which shows that no nitrogen has been incorporated into the aluminium substrate.

4.3.3.2 Discussion

This result clearly demonstrates that N_2 adsorption from the ambient does not take part in nitriding of aluminium. The role of the atomic nitrogen has also to be taken into consideration, since it can react with aluminium easier than the nitrogen in molecular form. The flux of atomic nitrogen at the sample position has been estimated in subsection 4.1.2.3. It is found to be about 20 times lower than the flux of ions. Therefore, even by assuming 100 % sticking of nitrogen atoms at the sample surface, the contribution of atomic nitrogen to the nitriding process can be considered as negligible.

The determination of nitrogen desorption is more complicated. The thermal desorption alone is not expected to play a significant role, since AlN has a high binding enthalpy of 3.36 eV, and it is unlikely that a chemically bonded nitrogen atom leaves the solid state. However, if nitrogen is free, for instance in over stoichiometric concentration, it might contribute to the desorption. The ion-stimulated desorption was not investigated here, since the ion bombardment causes also sputtering and the effect of nitrogen loss due to desorption in practice can not be distinguished.

4.3.4 Summary

A quantitative determination of nitrogen incorporation and loss in terms of ion-solid state interaction was done by performing experiments of aluminium ion nitriding at different ion energies, current densities and nitriding times. Dynamic binary collision simulations were performed to estimate the sputtering and backscattering yields of nitrogen. The obtained results are about 20 % lower than that the experimentally determined ones, which is a reasonable good agreement, because the computer simulations can not fully reproduce the experiment. Consequently, it can be concluded that the nitrogen incorporation is controlled by the ion implantation, while the nitrogen loss is controlled by sputtering and backscattering, whereby sputtering is dominating.

The contribution of neutrals (N_2 molecules and N atoms) to the incorporation of nitrogen because of adsorption from the ambient is found to be negligible. The role of nitrogen desorption was not investigated.

4.4 The mechanism of diffusional transport

4.4.1 Introduction

Diffusion plays an important role for formation of the nitride layer during ion nitriding. A significant thickness can be achieved only by a diffusional transport, since the direct implantation depth is small. In general, the diffusion is affected by the motion of all atomic species. However, it is interesting to know whether the nitride layer grows due to diffusion of both species nitrogen and aluminium (growth at two interfaces) or by one dominating element. A commonly accepted opinion about the diffusional transport during nitriding of aluminium is that nitrogen atoms diffuse into the aluminium bulk. Such an approach can be found in several publications, as for example Refs. [50, 51, 60, 66, 70, 85, 115, 141]. Nevertheless, there is no clear evidence for the dominating diffusion of nitrogen.

In this section, a study of the mechanism of diffusional transport during ion nitriding of aluminium is presented. For the identification of the main diffusing species, experiments by means of a marker layer and isotope sequence techniques are performed.

4.4.2 Experimental results

First, a stoichiometric AlN layer was formed by ion nitriding with ^{14}N at an ion energy of 1.6 keV, a fluence of 3.36×10^{18} at./cm² and a substrate temperature of 500°C. Afterwards, a dilute marker layer of gold (Au) was implanted approximately into the middle of the nitride layer. The implantation was carried out at an ion energy of 1 MeV at normal incidence and a fluence of 1×10^{16} at./cm² at room temperature. The ion energy was chosen on the base of TRIM calculations performed for a substrate with stoichiometric composition and standard density of AlN resulting in a mean projected range of about 200 nm with 100 nm straggling. The type of the marker and the fluence were chosen corresponding to the requirements of RBS, used for determination of the marker layer position. The simulated peak maximum concentration is about 1 at.%. Such a low concentration renders improbable that the diffusion of aluminium and nitrogen atoms will be affected by the implanted gold atoms. On the other hand, this amount of Au atoms is sufficient to be detected by RBS. Subsequently, the sample was reinstalled in the ion nitriding system and ion nitrided with ^{15}N at an ion energy of 1.6 keV and a fluence of 2.8×10^{18} at./cm² at 400°C. During the ion nitriding with ^{15}N , a part of the sample was covered by a Si wafer. Before and after ion nitriding with ^{15}N , the sample was analysed by RBS and TOF ERDA.

Fig. 4.10 a) shows the results obtained by RBS after ion nitriding with ^{14}N and ion implantation with Au. This spectrum was simulated using the computer code RUMP. The nitrogen to aluminium ratio is determined to be about 1, which corresponds to the stoichiometric concentration of AlN. The thickness of the nitride layer is found to be about 400 nm using the standard density of AlN. The implanted gold layer is situated in a 160 nm thick zone starting at a depth of 130 nm with an average Au concentration of 0.65 at.% in the implanted zone. The results are in good agreement with the simulated

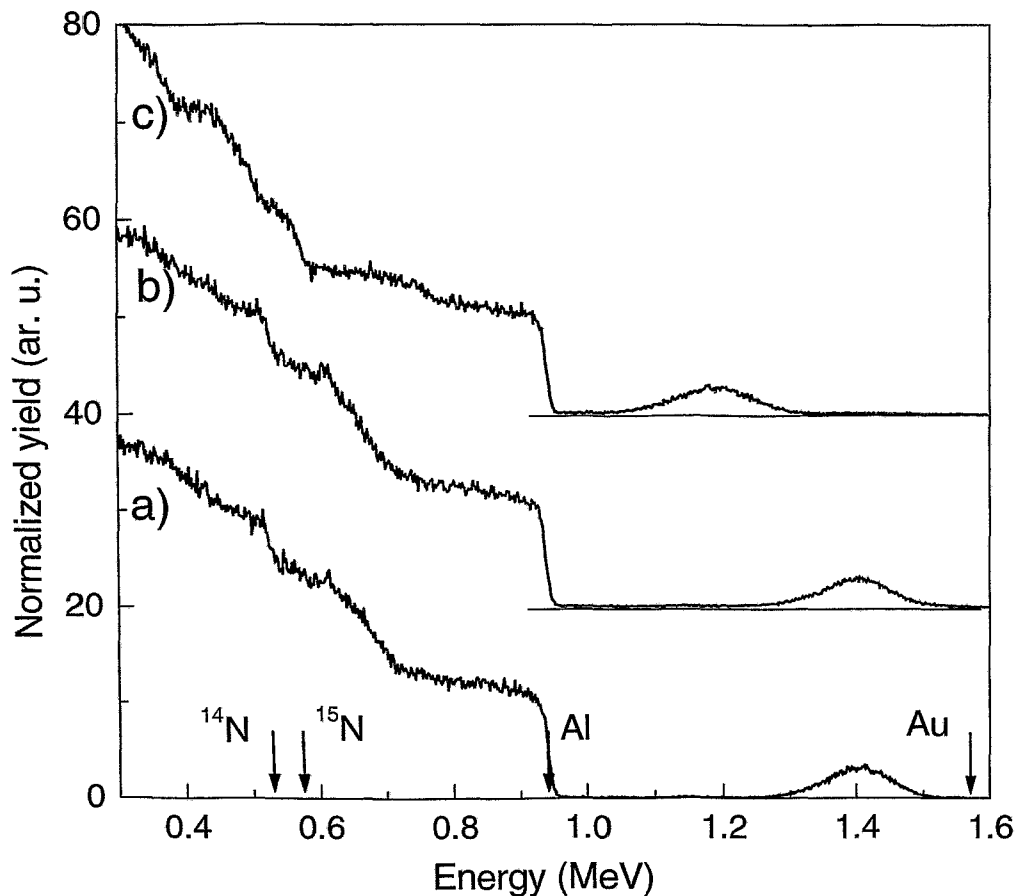


Figure 4.10: RBS spectra obtained after a) ion nitriding with ^{14}N and ion implantation with Au, b) additional heat treatment at 400°C (capped sample area) and c) subsequent ion nitriding with ^{15}N . The arrows denote the surface backscattering energies of ^{14}N , ^{15}N , Al and Au.

projected range, straggling and concentration of the marker layer. In Fig. 4.10 it can be seen that the signal obtained from the implanted gold layer has the Gaussian shape being typical for ion implantation at high energy.

For this experiment it is of essential importance to ensure that the marker layer does not move itself due to diffusion of the Au atoms in AlN. To investigate the effect of high temperature on the marker layer, RBS analysis was performed at the part of the sample, which was capped by the Si wafer during the ion nitriding with ^{15}N . Only in the case that the marker layer remains stable here, it can be also used as an indication for the relative migration of aluminium and nitrogen atoms. The obtained RBS spectrum is shown in Fig. 4.10 b) and as it can be seen the position and the shape of the Au peak remain nearly unaffected due to the temperature effect. Consequently, purely thermal diffusion of the gold atoms can be neglected. The capped part of the sample was also investigated by TOF ERDA and the obtained elemental depth profiles of ^{14}N , aluminium and oxygen are shown in Fig. 4.11 a). No other elements were detected in a significant amount. The measurement confirms the formation of a 400 nm thick stoichiometric AlN

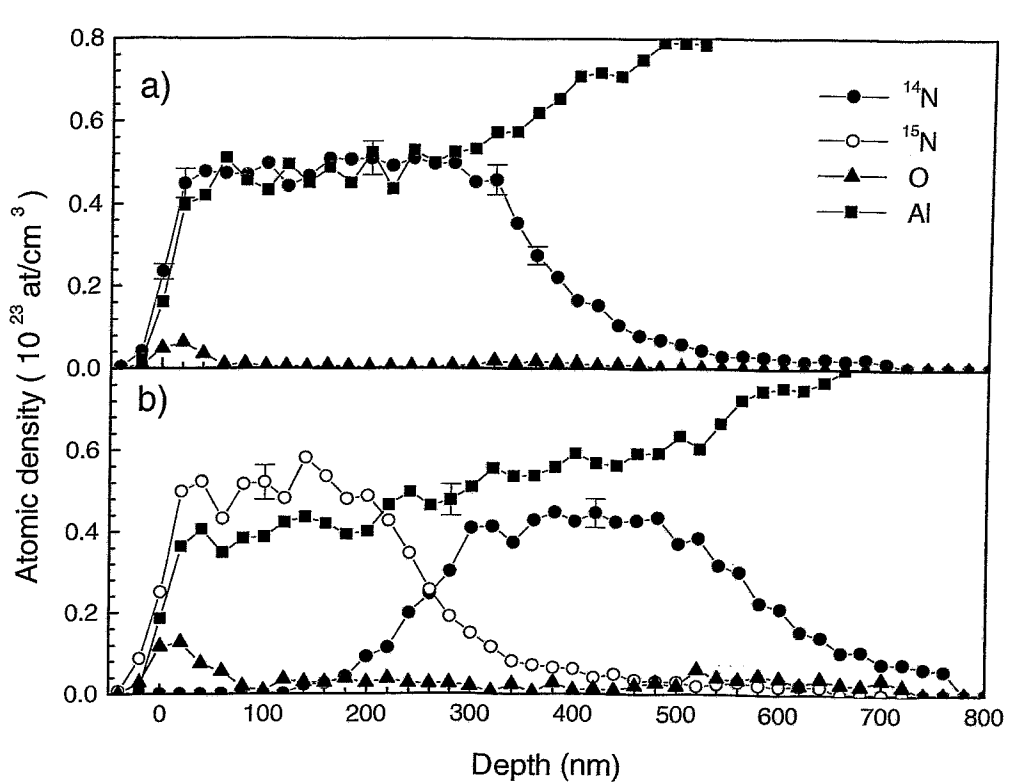


Figure 4.11: Elemental depth profiles of ^{14}N (full circles), ^{15}N (open circles), aluminium (squares) and oxygen (triangles) obtained by TOF ERDA after a) heat treatment at 400°C (capped sample area) and b) subsequent ion nitriding with ^{15}N .

surface layer. There is a well established plateau with equal atomic density of aluminium and nitrogen with an average value of $0.48 \pm 0.04 \times 10^{23} \text{ at/cm}^3$ each. A small amount of oxygen is found at the surface and close to the interface between the nitride layer and the aluminium substrate.

The effect of ion nitriding on the position of the gold marker layer was investigated in the part of the sample, which was exposed to the ^{15}N ion beam. The obtained RBS spectrum is plotted in Fig. 4.10 c). It shows clearly that the marker is shifted towards the bulk. According to a RUMP simulation, now the gold implanted zone starts at about 380 nm from the new surface. This indicates that the thickness of the nitride layer in front of the gold marker layer is significantly increased, even though the surface was eroded due to sputtering. On the other hand, the shape and average concentration of the gold layer remain nearly unchanged. Fig. 4.11 b) shows the elemental depth profiles of ^{14}N , ^{15}N , aluminium and oxygen obtained by TOF ERDA after ion nitriding with ^{15}N . It can be seen that ^{14}N is situated only in the bulk, while the post-implanted ^{15}N is located near the surface. Taking into account the limited depth resolution of the depth profiling by ion beam analysis the profiles are considered to have a rectangular shape for each of the isotopes.

4.4.3 Discussion

Three different mechanisms of diffusional transport can be discussed: i) dominating diffusion of nitrogen towards the interface AlN/Al, ii) diffusion of aluminium towards the surface or iii) a simultaneous diffusion of nitrogen and aluminium. The last one can be excluded because the diffusion of both elements is not consistent with the observed well separated rectangular nitrogen profiles. If simultaneous diffusion of nitrogen and aluminium takes place, the ^{15}N and ^{14}N depth profiles would overlap and no sharp interface between them would be observed. To decide between nitrogen or aluminium dominated diffusion, first the observed shift of the gold marker layer will be considered. As noted above, the diffusion of gold atoms in the nitride due to the high temperature during the ion nitriding process can be neglected and therefore the observed shift must be due to diffusional transport of nitrogen or aluminium atoms. If the diffusional transport would be dominated by inward diffusion of nitrogen, the nitride layer would grow behind the marker. Then the nitride thickness at front of the marker would even decrease because of surface erosion caused by sputtering, thus the gold peak should be shifted in the opposite direction relative to the surface. In contrast, the observed change of the gold peak position after ^{15}N ion nitriding shows that the nitride layer grows in front of the marker, indicating transfer of mass from the bulk through the marker layer to the surface. This mechanism is further confirmed by the ERDA elemental depth profiles in Fig. 4.11 b), which reveal that the nitride phase formation takes place at the surface. If nitrogen would diffuse through the existing nitride layer, one would expect a reverse distribution of the pre-implanted and the post-implanted isotope. It might be argued that the incoming ^{15}N dissociates the Al-N 14 bonds at the surface and then recombines with the free aluminium. The substituted ^{14}N could then be pushed into the bulk, continuing this substitution. Such a substitutional mechanism can be excluded from an energetic point of view, since behind the implantation depth the atoms obtain only a thermal energy of about 0.1 eV (estimated for a substrate temperature of 500 °C), which is much less than the binding enthalpy of AlN (3.36 eV). Moreover, as explained above the diffusion of nitrogen atoms through the bulk would shift the position of the gold marker layer to the surface. Collisional mixing as it is reported in Ref. [50] is also not an appropriate explanation for the observed depth distributions, taking into account the small implantation range and the shape of the observed depth profiles of ^{14}N and ^{15}N . Hence, it can be concluded that during ion nitriding of aluminium the nitride layer grows due to dominating diffusion of aluminium atoms from the underlying bulk towards the surface where a new AlN is formed.

In addition, it should be noted that the picture of diffusional transport dominated by diffusion of aluminium atoms is also consistent with the obtained depth profiles of oxygen (see Fig. 4.11). After the ion nitriding small amounts of oxygen are found, besides at the surface, in particular near the interfaces. These interface peaks can be attributed to the original surface positions, which are now buried by the aluminium which is diffused to the surface.

Furthermore, the distribution of ^{14}N and ^{15}N profiles reveals a layer-by-layer growth of the nitride layer. Since the nitride formation takes place at the surface, the newly formed nitride layer shifts the already existing one in direction of the bulk.

4.4.4 Summary

In this section, the mechanism of diffusional transport during ion nitriding of aluminium was investigated. To define whether the nitride layer grows due to diffusion of nitrogen or aluminium atoms an experiment by means of a dilute gold marker layer was performed. The obtained results reveal that the diffusional transport is dominated by the diffusion of aluminium rather than nitrogen. This mechanism is confirmed by the results obtained after ion nitriding with two different isotopes of nitrogen. The post-implanted ^{15}N is found near the surface, while the pre-implanted ^{14}N is situated deeply in the bulk. The rectangular shape of the isotope depth profiles excludes a simultaneous diffusion of nitrogen and aluminium atoms. Furthermore, the depth distribution of ^{14}N and ^{15}N indicates that the formation of AlN takes place close to the surface with the nitrogen being deposited there by the ion beam and the aluminium being provided by diffusion from the underlying bulk through the nitride which is formed before. The phenomenon of dominating aluminium diffusion and AlN phase formation at the surface during nitriding of aluminium is observed for the first time in the present study.

4.5 Growth kinetics of the nitride layer

4.5.1 Introduction

Achieving control over the nitride layer growth during ion nitriding of aluminium requires an investigation of the influence of all process parameters on the nitride layer growth kinetic. Since nitriding is a diffusional process, the substrate temperature is expected to play a critical role for the evolution of the nitride layer. Therefore, in this section, a study of the nitride layer growth kinetic at different substrate temperatures and fixed ion beam parameters is presented. The influence of ion flux and ion energy on the kinetics of aluminium nitriding at the temperature of 350 °C has been already investigated in section 4.3. On the base of the obtained results and considering the mechanism of diffusional transport presented in section 4.4, a model of the aluminium ion nitriding process is suggested. Equations describing the growth of the nitride layer are obtained. Diffusion coefficients and an activation energy of aluminium diffusion in the AlN matrix are derived.

4.5.2 Experimental results

Ion nitriding was performed at an ion energy of 1.6 keV and a current density of 0.2 mA/cm² for temperatures of 250 °C, 300 °C, 350 °C and 400 °C, which were kept constant within ± 20 °C during the process. For each of these temperatures a series of experiments was done, thereby increasing the nitriding time from 5 min up to 60 min. Before ion nitriding, the samples were cleaned by sputtering with Ar⁺ at an ion energy of 1.6 keV and a current density of 0.2 mA/cm² for 10 min. The samples were analysed by NRA.

Fig. 4.12 shows the obtained nitrogen profiles for the different temperatures and times. Taking into account the depth resolution of NRA, which is about 250 nm at the surface and increases towards the depth, the shape of the profiles is consistent with a rectangular depth distribution as already discussed in section 4.4. In this context, it should be noted that the profiles obtained from layers with a small thickness are significantly affected by the depth resolution. This effect is especially pronounced in the case of 250 °C, where the layers have a maximum thickness of about 180 nm only. Here the maximum nitrogen concentration is strongly reduced. In Fig. 4.12 it can be also seen that the profiles at 400 °C and 350 °C have a slightly different nitrogen maximum concentration of 48 at. % and 44 at. %, respectively. Since these layers are of comparable thickness the observed difference can not be explained by the depth resolution of the method and will be further investigated in section 4.7.4.

The thickness of the nitride layers was defined from the total amount of incorporated nitrogen and the atomic density of the layers (determined in section 4.7.1). The results are shown in Fig. 4.13 by squares as a function of nitriding time for the different temperatures. Again, an incubation time of about 2 min is observed. Moreover, two different dependencies of layer thickness on nitriding time can be distinguished. At 400 °C the dependence is linear. This can be interpreted as layer growth proportional to the supply of nitrogen atoms by the ion beam. At temperatures of 300 °C and 250 °C the layer thickness obeys an apparently different dependence on time, which appears to be parabolic one and indicates a diffusion controlled process. The evolution of the layer thickness at 350 °C is

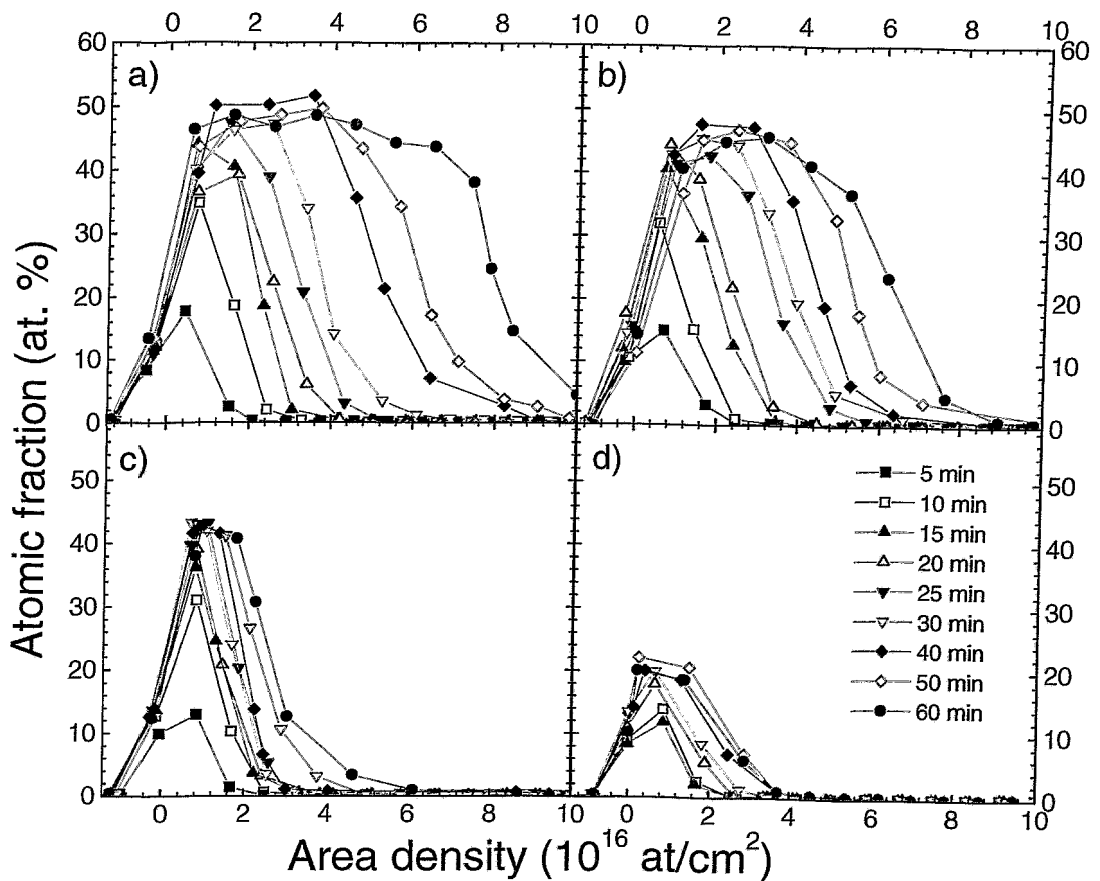


Figure 4.12: Nitrogen profiles obtained by NRA after ion nitriding of aluminium at an ion energy of 1.6 keV and a current density of 0.2 mA/cm² for different nitriding times and substrate temperatures of a) 400 °C, b) 350 °C, c) 300 °C and d) 250 °C.

a combination of both cases. For nitriding times less than 2400 s the data are consistent with a linear dependence, which later transforms to a parabolic function of the processing time. It should be also noted, that the data presented in Fig. 4.13 are limited to a maximum nitriding time of 60 min. Actually, experiments at longer nitriding time were performed too, but the obtained results do not obey any of the dependencies described here. This phenomenon will be discussed in detail in section 4.7.2.

4.5.3 Model of aluminium ion nitriding

Considering the mechanism of aluminium ion nitriding presented in the previous section, a simplified picture of the process can be drawn. Fig. 4.14 shows an elemental piece of the sample with three different zones as follows: 1) a near surface region, where the nitrogen is implanted and AlN formation takes place, 2) a zone of the nitride layer the thickness of which is zero in the beginning and increases during the process and 3) the underlying

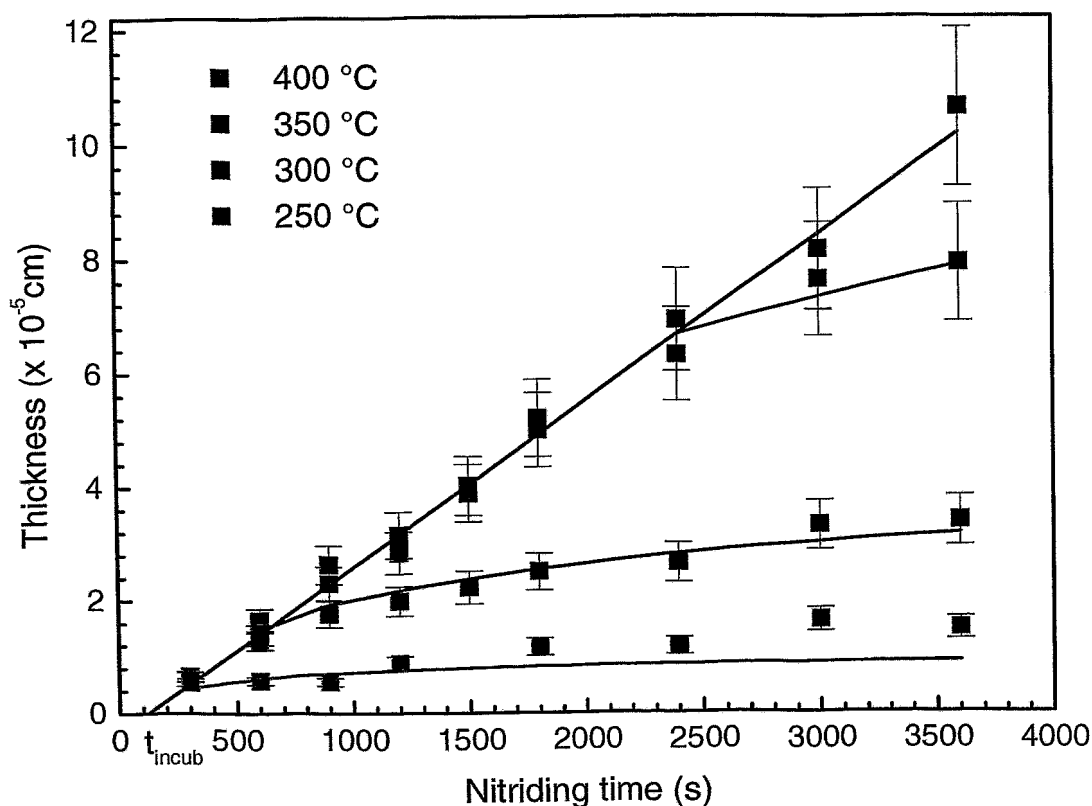


Figure 4.13: Nitride layer thickness as a function of the processing time for substrate temperatures of 250 °C, 300 °C, 350 °C, and 400 °C. The experimental data (squares) are fitted by Eq. 4.10 (a solid line) for $n = 3.8 \times 10^{22}$ at./cm³, $n_{Al} = 6 \times 10^{22}$ at./cm³, $j_N = 1.125 \times 10^{15}$ at./cm²s and $s = 9 \times 10^{-9}$ cm/s.

bulk, which is a source for aluminium atoms. Since the ion beam can be considered as homogeneous over the sample area (refer to Fig. 4.2 in section 4.1), a one dimensional approach to describe the ion nitriding phenomenon will be applied here.

The nitride layer grows only if both elements nitrogen and aluminium are delivered to the first, here named "reaction" zone. The transport of nitrogen and aluminium atoms can be described by means of corresponding fluxes j_N and j_{Al} , as shown in Fig. 4.14. The flux of nitrogen is a constant flux, defined by the flux of nitrogen atoms delivered by the ion beam and reduced by the sputtering loss of nitrogen. In this sense, j_N can be considered as an effective flux. Let us assume that this is also valid for j_{Al} , because sputtering of aluminium atoms can also occur. The flux of aluminium is caused by the concentration gradient in the system. To define the difference in concentration only the free aluminium will be taken into consideration. The aluminium, which is bound in AlN is fixed and therefore it can not contribute to the diffusion as shown by the absence of intermixing in the isotope nitriding experiment of section 4.4. At the surface the concentration of free aluminium is assumed to be zero, since in the "reaction" zone all arriving aluminium is consumed by the formation of AlN. The bulk consists only of aluminium with the concentration n_{Al} . Then, the concentration gradient in the system is determined by the

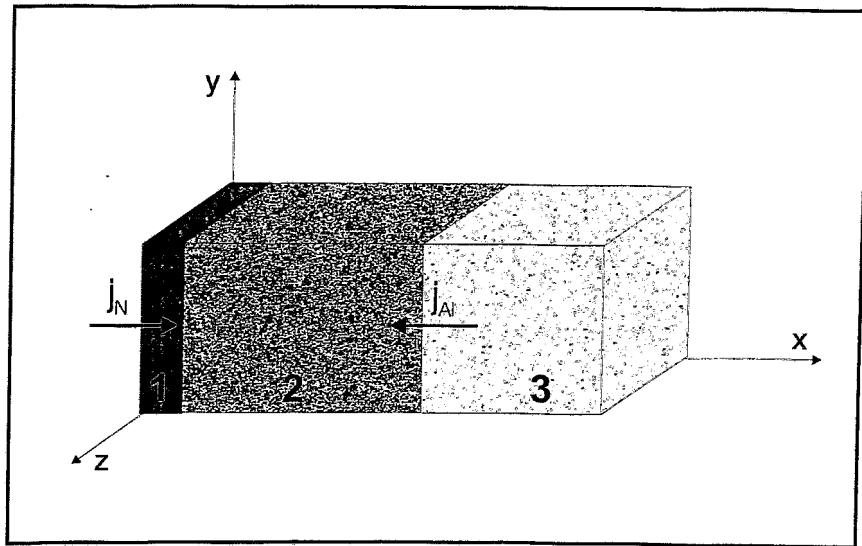


Figure 4.14: An elemental piece of the sample, indicating the different zones formed during ion nitriding of aluminium: 1) "reaction zone" situated near the surface where nitrogen is implanted and formation of AlN takes place, 2) the zone of the nitride layer the thickness of which is zero in the beginning and increases during the process and 3) the underling bulk, which is a source for aluminium atoms.

difference in aluminium concentration between bulk and surface divided by the thickness of the nitride layer x , i. e. it is equal to n_{Al}/x . For a steady-state regime the first Fick's law can be applied (Eq. 2.10) and the aluminium flux is given by:

$$j_{Al} = D \frac{n_{Al}}{x} - j_{Al}^s, \quad (4.8)$$

where D is the diffusion coefficient of aluminium through the nitride layer determined by Eq. 2.11 and j_{Al}^s is the flux of sputtered aluminium. The diffusional flux is directed down the concentration gradient i.e. towards the surface as shown in Fig. 4.14.

The growth of the nitride layer is limited either by the flux of nitrogen atoms delivered from the ion beam or by the diffusive flux of aluminium atoms. In this sense, the nitride layer growth rate can be written as:

$$\frac{dx}{dt} = \frac{2}{n} \begin{cases} j_N & \text{if } j_N \leq j_{Al} \\ j_{Al} & \text{otherwise} \end{cases}, \quad (4.9)$$

where n is the atomic density in the nitride layer. The factor 2 appears since each incorporated nitrogen or aluminium atom, in both cases, involves the incorporation of one atom of the other species due to the surface reaction.

From Eqs. 4.8 and 4.9 the thickness of the nitride layer is given by the analytical solution:

$$x(t) = \begin{cases} kt & \text{if } t \leq t_0 \\ ds^{-1} \left(1 + \text{ProductLog} \left(-e^{-\left(1 + \frac{st}{d}\right)} \right) \right) & \text{otherwise} \end{cases} \quad (4.10)$$

where $k = 2j_N/n$, $d = 2Dn_{Al}/n$, $s = 2j_{Al}^s/n$ and t_0 is the transition time at which the nitride layer growth changes from the regime controlled by the rate of nitrogen supply to the regime controlled by the rate of aluminium diffusion.¹

The transition time is defined by a consideration for continuity as:

$$t_0 = ds^{-1} \left(k + s + k \text{ProductLog} \left(-\frac{(k+s)e^{-\left(1 + \frac{s}{k}\right)}}{k} \right) \right). \quad (4.11)$$

t_0 can be determined also graphically as the crossing point between the two functions given in Eq. 4.10.

Eq. 4.10 is used to fit the experimentally determined layer thickness as a function of nitriding time, as shown in Fig. 4.13. To fit the data, the exact solution of 4.10 in the case of $t > t_0$ was expanded in a power series to the third order of t , which is given by:

$$x(t > t_0) = \frac{d\sqrt{2t\frac{s^2}{d}}}{s} - \frac{2st}{3} + \frac{s\sqrt{\frac{s^2}{d}}t^{3/2}}{9\sqrt{2}} + \frac{2s^3t^2}{135d} + \frac{s^3\sqrt{\frac{s^2}{d}}t^{5/2}}{540\sqrt{2}d} - \frac{4s^5t^3}{8505d^2} + O[t]^{7/2} \quad (4.12)$$

The parameters j_N and n are chosen on the base of the following experimental results. The effective flux of nitrogen atoms has been determined in section 4.3. For an ion current density of 0.2 mA/cm² the effective flux of nitrogen atoms (j_N) is taken as 1.125×10^{15} at./cm²s on the base of experimentally determined nitrogen loss (refer to Fig. 4.9). The atomic density of the nitride layer is 7.5×10^{22} at/cm³, which is determined in section 4.7.1. The atomic density of aluminium in the bulk (n_{Al}) is chosen to be equal to the standard of aluminium (6×10^{22} at/cm³).

The best fit, which satisfies all data with the same sputter rate of aluminium 3.4×10^{14} at/cm²s ($s = 9 \times 10^{-9}$ cm/s) is shown in Fig. 4.13 by a solid line. It can be seen that the obtained fit is in good agreement with the experimental data. Only in the case of 250 °C there is a difference, which is in the order of the experimental error. A diffusion constant $D_0 = 1.1 \times 10^{-3} \pm 0.6 \times 10^{-3}$ cm²/s and an activation energy $U = 1.1 \pm 0.3$ eV are determined from the parameters d obtained by the fit for temperatures of 250 °C, 300 °C and 350 °C. The large error for D_0 is due to the high correlation of d and s parameters in Eq. 4.10. Then, diffusion coefficients for the different temperatures are determined by Eq. 2.11 and listed in Table 4.2. The transition time t_0 for the different substrate

¹The *ProductLog* function gives the solution for w in $z = we^w$.

temperatures and for d and s values determined by the fit are calculated by Eq. 4.11 and listed in Table 4.2 too. The graphical solution for t_0 at the temperature of 250 °C, 300 °C and 350 °C can be seen in Fig. 4.13. It should be noted that for the determination of D and t_0 , the incubation time t_{incub} was taken into consideration.

In the above model, it has been assumed that freely diffusing aluminium atoms are available at the layer/substrate interface with a concentration being equal to the atomic density of the metal. Alternatively, a thermally activated solution of aluminium into AlN might be proposed. However, any corresponding data of solubility are not available to the knowledge of the author. Formally, the above model would remain unaltered since only the product of D and n_{Al} appears.

Temperature (°C)	Diffusion coefficient (D) (cm ² /s)	Transition time (t_0) (s)
250	2.8×10^{-14}	246
300	2.3×10^{-13}	697
350	1.4×10^{-12}	2360
400	6.4×10^{-12}	16140

Table 4.2: Diffusion coefficients of aluminium in AlN and transition times obtained by fitting of the experimental data in Fig. 4.13 with Eq. 4.10 ($D_0 = 1.1 \times 10^{-3} \pm 0.6 \times 10^{-3}$ cm²/s and $U = 1.1 \pm 0.3$ eV).

4.5.4 Discussion

The obtained experimental results together with the model presented here allow to distinguish two different regimes of nitride layer growth depending on the process parameters. For nitriding times shorter than the transition time t_0 the nitride layer grows with a constant rate determined in terms of nitrogen delivery by the ion beam and nitrogen loss due to sputtering and backscattering. The desired growth rate can be adjusted by the current density of the ion beam considering the effect of sputtering (refer to Fig. 4.8 and Fig. 4.9 in section 4.3). In this regime the diffusion does not play a limiting role, because the nitride layer is relatively thin and for the given temperature the diffusion rate of aluminium is faster than the rate of nitrogen supply. After the transition time, the layer thickness becomes significant and hampers the diffusion of aluminium atoms. In this regime the rate of aluminium diffusion plays a limiting role, which determines the nitriding kinetic. Basically, the nitride layer thickness is a square root function of time, slightly reduced by the erosion due to sputtering. This result is in agreement with other studies on the evolution of the nitride layer during ion nitriding of steel [14, 117]. They have shown that at similar diffusion and sputtering rates, a significant deviation from the parabolic law takes place for nitriding times larger than 60 min.

The sputter rate of aluminium was calculated by TRIDYN (see Fig. 2.4 on page 16). For an ion energy of 0.8 keV and 1.6 keV the computer simulations results in a sputtering

yield of 0.17 and 0.21, respectively. Considering the composition of the ion beam and the flux of nitrogen, the sputtered flux of aluminium is found to be 3.8×10^{14} at./cm²s, which is about 10 % higher than the value obtained from the fit (3.4×10^{14} at./cm²s). It has to be taken into consideration that in the diffusion controlled regime the supply of aluminium atoms to the "reaction" zone is lower. This may lead to a decrease in the sputtered yield of aluminium, since less aluminium atoms are present in the near surface region. This effect should be most pronounced for the lowest temperature and may be the reason for the observed difference between experiment and fit at 250 °C. Moreover, in the diffusional regime the amount of nitrogen loss might be also different to that determined in section 4.3. Taking into account that an AlN compound forms only if free aluminium is delivered to the "reaction" zone, a limitation in the arriving rate of aluminium limits also the incorporation rate of nitrogen. Then, the exceeding amount of nitrogen can form N₂ molecules, which for instance, can be incorporated in cavities of the nitride layer. However, most probably the excess nitrogen is released through the surface to the gas phase. In the last case, an essential contribution to the nitrogen loss is added to the nitrogen loss due to sputtering and backscattering discussed in section 4.3. The different layer thickness observed in Fig. 4.13 for the same incident fluence but different temperatures indicates that in the diffusional controlled regime the amount of nitrogen loss significantly increases in relation to the lower incorporation rate. In the extreme case of ion nitriding performed at 250 °C for 60 min, the amount of incorporated nitrogen is estimated to be only 15 % of the supplied nitrogen.

The mechanism of aluminium diffusion through the nitride layer has not been investigated. Interstitial diffusion of aluminium is not appropriate, because the aluminium atoms have a larger atomic radius (1.82 Å) in comparison to nitrogen (0.75 Å). Aluminium may diffuse substitutionally via vacancies or along grain boundaries and other defects. The values of the diffusion coefficients determined here (Table 4.2) are in the range of diffusion coefficients characteristic for grain boundary diffusion according to Fig. 2.6 on page 17. However, it has to be noted that the temperature range, material and diffusing species used for the determination of the diffusion coefficients in Fig. 2.6 are not specified and therefore this argument is not sufficient to draw a conclusion. On the other hand, concerning the fine size of AlN crystallites, which is less than 10 nm (refer to section 4.6), the diffusion along grain boundaries appears to be the most possible mechanism.

4.5.5 Summary

The growth kinetic of the nitride layer formed by ion nitriding of aluminium at an ion energy of 1.6 keV and an ion current density of 0.2 mA/cm² for temperatures of 250 °C, 300 °C, 350 °C and 400 °C was investigated. The nitride layer growth is controlled either by the delivery of nitrogen atoms from the ion beam or by the diffusion of aluminium atoms through the formed nitride layer. The two regimes are characterised as a function of process parameters. A modelling approach results in determination of a diffusion activation energy of 1.1 eV and diffusion coefficients of aluminium, which are listed in Table 4.2.

4.6 Phase formation and structure analysis

4.6.1 Introduction

In this section, an investigation of the phases and structure of the nitride layers is presented. For an integral investigation, XRD at grazing incidence is applied. The obtained results are compared with results of HRTEM images, which give an information from a selected area only.

4.6.2 Experimental results

Fig. 4.15 a) shows an example of an X-ray diffraction pattern obtained after ion nitriding of an aluminium polycrystalline sample at an ion energy of 1.6 keV, a current density of 0.2 mA/cm², and a substrate temperature of 300 °C for 20 min. The appearance of Bragg peaks at $2\theta = 33.2^\circ$, 49.8° , 59.3° and 71.4° clearly indicates formation of hexagonal AlN. There is a good agreement with the diffraction angles for hexagonal AlN taken from the PDF data base, shown by squares in Fig. 4.15. The measured peaks are of broad shape, indicating a fine grained polycrystalline structure of the nitride layer. It has to be taken into consideration that the thickness of the investigated layers (about 250 nm) is smaller than the penetration depth of the X-ray beam, even for the grazing incidence technique ($\theta_{in} \approx 1^\circ$) used here. Therefore, an occurrence of diffraction peaks from the aluminium substrate is unavoidable. This can be seen in Fig. 4.15 a), where these peaks have strong intensity and narrow shape. Their smaller width indicates a larger grain size. Moreover, the deviation of the measured peak intensity ratios from the calculated ones (diamonds) indicates the existence of preferred orientations in the substrate. The texture is an effect of the manufacturing process of the aluminum rods, from which the samples are cut. The superposition of diffraction peaks from the layer itself and the aluminium substrate is an obstacle for the determination of a metastable f.c.c. AlN phase (refer to section 2.3.1). Due to the very small difference in the lattice constant of f.c.c. AlN ($a = 4.055 \text{ \AA}$) and f.c.c. Al ($a = 4.049 \text{ \AA}$) the diffraction angles 2θ are almost the same, as shown by triangles and diamond symbols in Fig. 4.15. Therefore, in practice the Bragg peaks from the cubic AlN phase will fully overlap with the strong reflections from aluminium. In order to overcome this problem, an aluminium single crystal with (111) orientation was used as substrate instead of the polycrystalline sample. The advantage of the single crystal substrate is that XRD analysis can be done at such a crystal orientation at which diffraction is avoided and no aluminium Bragg peaks will occur. In Fig. 4.15 b) the diffraction pattern of the aluminium single crystal substrate after wet chemical removing of the damaged surface layer is shown by the dotted line. It can be seen that indeed no diffraction peaks are observed. Further, the aluminium crystal was ion nitrided at 1.6 keV ion energy, 0.2 mA/cm² current density and 300 °C substrate temperature for 50 min. The diffraction pattern obtained for the same crystal orientation after ion nitriding is shown in Fig. 4.15 b) by the solid line. From the position and intensity of the observed Bragg peaks it can be seen that the main phase present in the layer is the hexagonal AlN. In addition, diffraction peaks arise at $2\theta = 38.33^\circ$, 44.55° , 64.85° and 78.47° . They can be interpreted as diffraction peaks from the f.c.c. AlN phase. The diffraction intensity of these peaks is very low in

comparison to those from the hexagonal phase. From the intensities of the corresponding peaks the content of the cubic phase is roughly estimated to be about 5 % only. For the hexagonal AlN phase no indication for a preferred orientation of the crystallites is observed. In contrast to that, the cubic phase shows a preferred (111) orientation. An average grain size of the crystallites in the nitride layer is estimated from the width of the corresponding diffraction peaks in Fig. 4.15 b). The average grain size of the crystallites of the hexagonal AlN phase is determined to be about 5 nm, while this of the cubic phase is larger, about 16 nm.

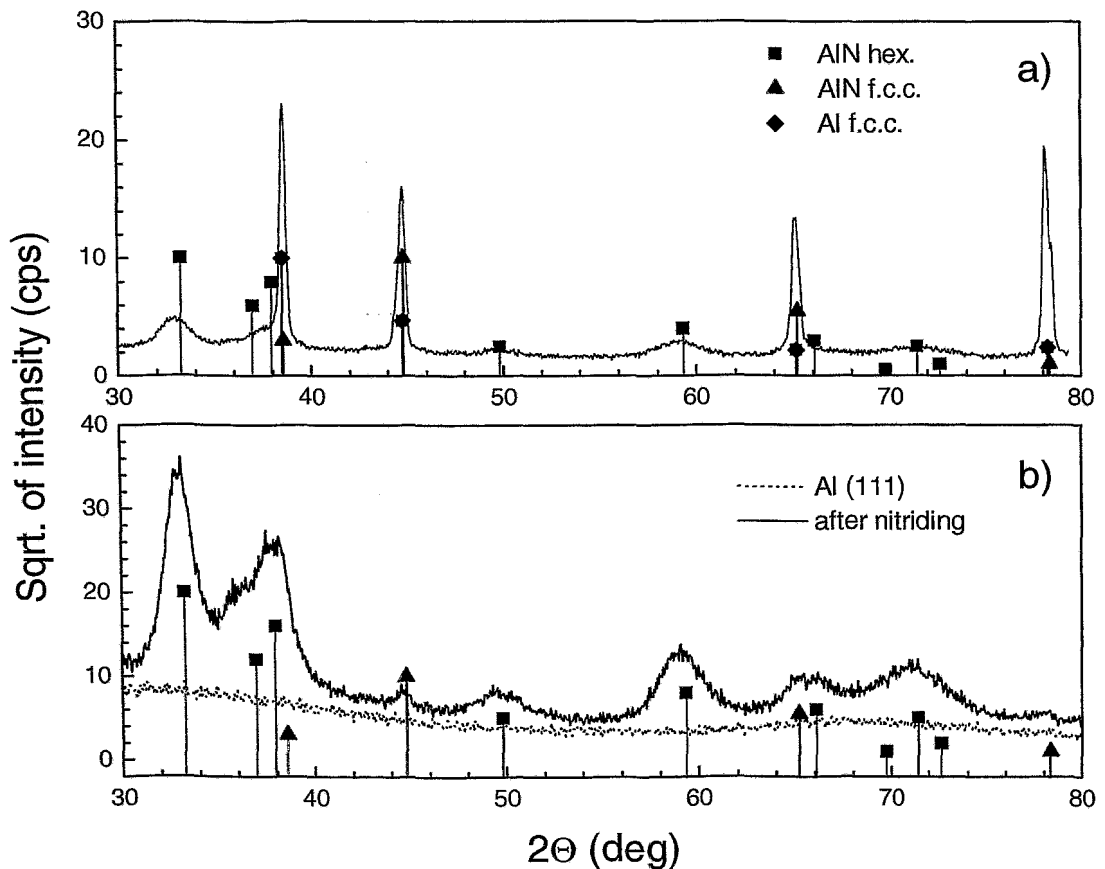


Figure 4.15: X-ray diffraction pattern obtained at 0.5° grazing incidence from a) an Al polycrystalline sample after ion nitriding at an ion energy of 1.6 keV, a current density of 0.2 mA/cm^2 , a substrate temperature of 300°C for 20 min and b) an Al (111) single crystal before ion nitriding (dotted line) and after ion nitriding at an ion energy of 1.6 keV, a current density of 0.2 mA/cm^2 , a substrate temperature of 300°C for 50 min. The squares show the PDF peak positions for hexagonal AlN, the triangles and diamonds indicate the peak positions of the cubic phase of AlN and Al, respectively.

A more detailed investigation of the crystallites with the hexagonal AlN structure was carried out. The influence of the temperature was investigated by annealing an already formed nitride layer at 500°C for 54 h in vacuum. The performed XRD analysis reveals that the size of the crystallites is weakly increased from 5.5 nm up to 7 nm. The effect of

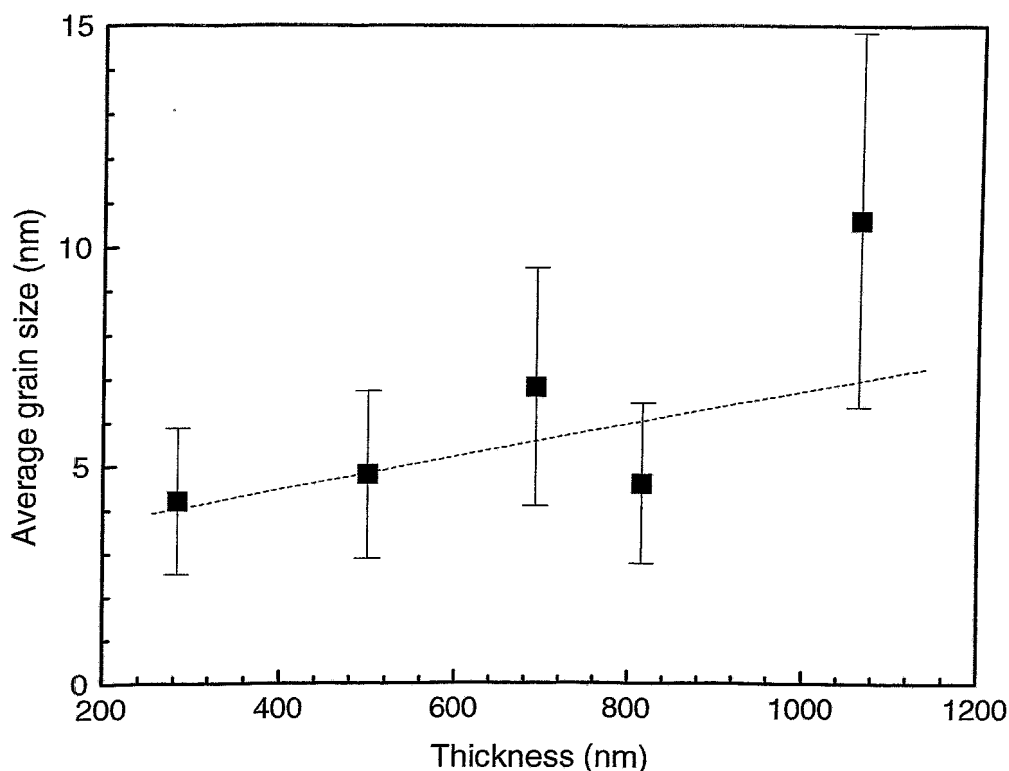


Figure 4.16: Average grain size of the crystallites having hexagonal AlN structure for nitride layers with a different thickness. The layers are obtained after ion nitriding at 1.6 keV, 0.2 mA/cm², 400 °C for times varied from 20 min to 60 min by intervals of 10 min.

ion nitriding for different times, hence of different layer thickness on grain size was also investigated. For this reason, a series of nitride layers was analysed, which were grown by ion nitriding of aluminium polycrystalline samples at an ion energy of 1.6 keV, a current density of 0.2 mA/cm², substrate temperature of 400 °C and nitriding times varied from 20 min to 60 min by intervals of 10 min. Fig. 4.16 shows that the average grain size of the hexagonal AlN crystallites increases from 4 nm up to 10 nm as the layer thickness increases.

The presence of crystallites with cubic structure in the nitride layer is also confirmed by HRTEM analysis. Fig. 4.17 shows an image taken from a selected area in the nitride layer near to the interface with the aluminium substrate. The investigated layer is obtained by ion nitriding of an aluminium polycrystalline sample at 1.6 keV ion energy, 0.2 mA/cm² current density and 500 °C substrate temperature for 15 min. By applying Fourier transformation from the marked areas in Fig. 4.17, the local lattice spacing is determined. Again, together with regions having a lattice constant of hexagonal AlN regions are observed with a lattice constant, which can be attributed either to f.c.c. Al or the f.c.c. AlN phase.

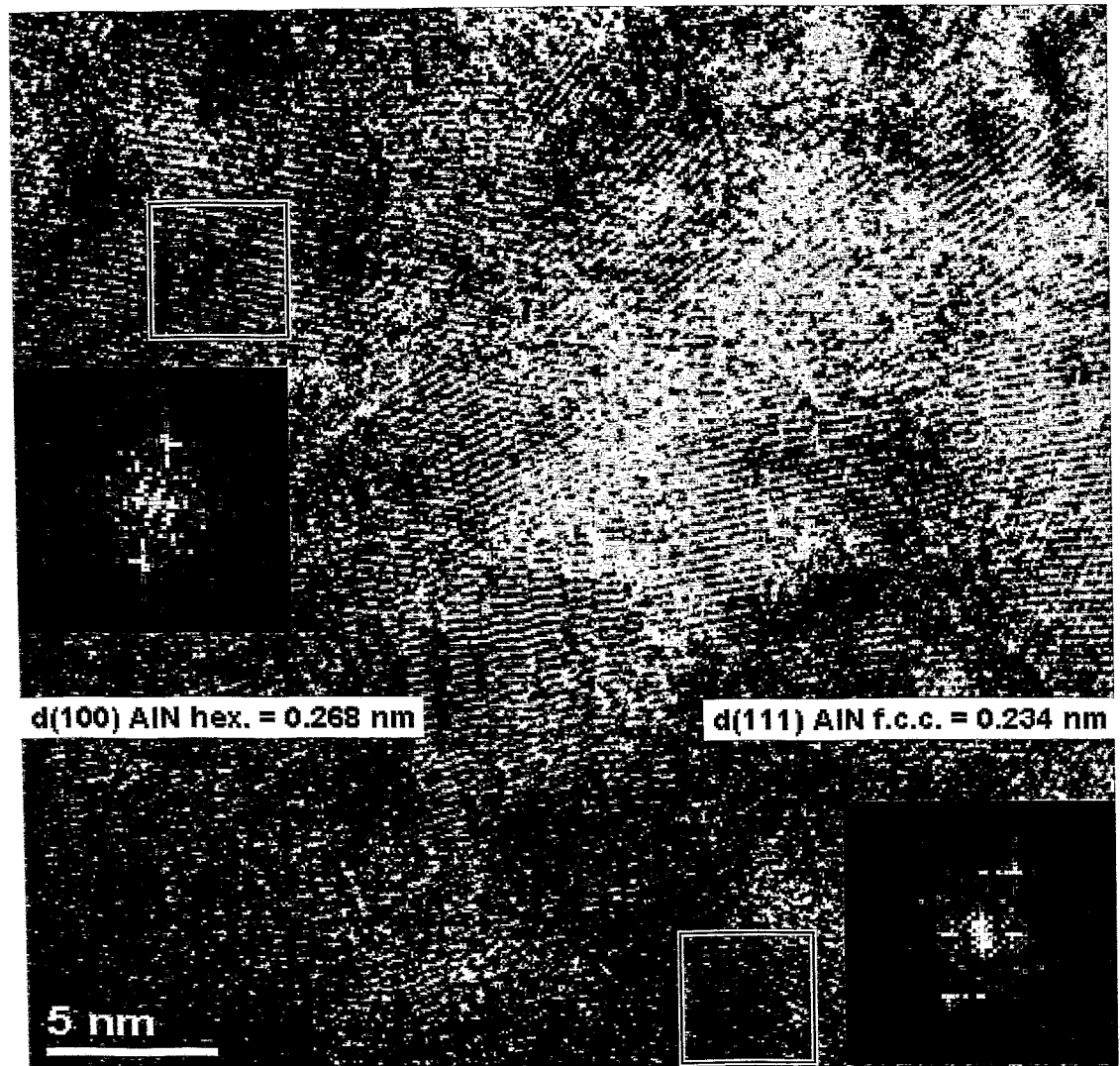


Figure 4.17: HRTEM cross-sectional image and Fourier transform showing the existence of crystallites with a cubic phase.

4.6.3 Discussion

The experiment performed with the (111) oriented aluminium single crystal sample clearly proves the presence of a cubic phase in the formed nitride layer. In this case, an influence of the aluminium substrate on the obtained diffraction pattern can be excluded because of two reasons. First, the XRD analysis was done at such an orientation of the crystal for which it was proven that no diffraction peaks occur. Second, the observation of the peaks at $2\theta = 38.33^\circ$, 44.55° , 64.85° and 78.47° indicates that the diffracting material is polycrystalline. Taking into consideration the low ion energy at which the ion nitriding

was performed, it is not to expect that the single crystalline structure of the aluminium substrate behind the nitride layer can be damaged to a polycrystalline one. Another possible explanation for the origin of observed additional diffraction peaks is that some aluminium crystallites may be present in the nitride layer. This would be consistent with the mechanism of aluminium nitriding which requires a fraction of free aluminium atoms diffusing through the nitride layer. On the other hand, the cubic phase could be a metastable f.c.c. AlN phase. By the performed XRD and HRTEM analysis it is not possible to distinguish between the cubic phases of Al and AlN because of the small difference in lattice constants. However, considering the large size of the crystallites having a cubic structure (about 16 nm), it is most likely that the observed phase is metastable f.c.c. AlN. The aluminium atoms which travel through the nitride layer in order to approach the surface, should not be able to form such large grains. Moreover, the preferred (111) orientation shows a clear relation to the aluminium substrate. Therefore, it is expected that the cubic AlN phase is present near the interface. This is confirmed by HRTEM analysis of the local lattice spacing. It shows that the regions with a cubic structure are localized in the nitride layer near to the interface with the aluminium substrate.

The formation of metastable cubic AlN as a result of aluminium nitridation by PIII was also reported by Manova et al. [87]. In this study, f.c.c. AlN is observed only at substrate temperatures of 300 °C and below. The authors explain this effect by the enhanced mobility of aluminium atoms at higher temperature, leading to a rearrangement of the crystal lattice to the energetically favoured hexagonal AlN phase. In the present study, an indication that the f.c.c. AlN phase is more pronounced at low temperatures is also observed. Nevertheless, the HRTEM analysis reveals formation of the cubic AlN phase also after ion nitriding at 500 °C (see Fig. 4.17).

The present study shows that the nitride layers exhibit a nano-crystalline structure. It should be noted that in the determination of the average grain size of the crystallites by means of the "Integral width method" the influence of microscopic stress is taken into account. The XRD analysis of the nitride layer annealed for a long time (54 h) at 500 °C shows that the average grain size increases only weakly from 5 nm to 7 nm. Therefore, it can be concluded that the temperature alone does not play a significant role for the growth of the crystallites. More pronounced is the effect observed by prolongation of the nitriding time. Ion nitriding for 1 h at 400 °C results in formation of grains with an average size of 10 nm. This could be an effect of depth dependent crystalline size. The crystallites formed in the beginning may grow during the process. This will result in formation of larger grains near to the interface with aluminium bulk and influence the average grain size determined by XRD. On the other hand, the increased crystallite size could be caused by radiation defects. Even that only the near surface region is damaged by the implantation, the high temperature allows migration of defects into depth. Moreover, the nitride layer grows at the surface, which means that the surface and the created there defects are continuously buried during the process. Most probably the mechanism by which the grains grow is the so called Ostwald ripening [142]. During this process the smallest crystallites dissolve giving rise to the growth of the largest ones. The transformation occurs because larger crystallites with their greater volume to surface area ratio, represent a lower energy state and therefore they are thermodynamically more favoured. Furthermore, the grain growth can be caused by the aluminium atoms, which diffuse through the layer. If a small amount

of over-stoichiometric nitrogen is present in the nitride layer (refer to 4.7.4), it may react with some of the aluminium and contribute to the growth of the AlN crystallites.

4.6.4 Summary

The study presented in this section shows that the main crystallographic phase formed after ion nitriding of aluminium is hexagonal AlN phase, randomly oriented. In addition, a small content of metastable f.c.c. AlN phase is also observed. The cubic AlN phase has a preferred orientation related to that of the aluminium substrate and it is found to be present in the nitride layer near to the interface with aluminium. No other phases are detected in the layer.

The formed nitride layers have a nano-crystalline structure. Investigation of the crystallites with hexagonal structure shows that the average grain size increases from 4 nm up to 10 nm by increasing the nitriding time from 20 min up to 60 min. The effect of annealing on the grain growth is small.

4.7 Characteristics and properties of the nitride layers

4.7.1 Atomic density

In general, the density of thin layers created by implantation or deposition techniques can strongly deviate from the bulk density. Incorporation of gas molecules or crystalline disorder may produce holes and pores which reduce the layer density of the material. This may have an influence on several other properties of the layers such as: adhesion, hardness, electrical and optical properties, etc. In this study, the atomic density of the nitride layers produced by ion nitriding of aluminium was determined by means of ion beam analysis and thickness measurements.

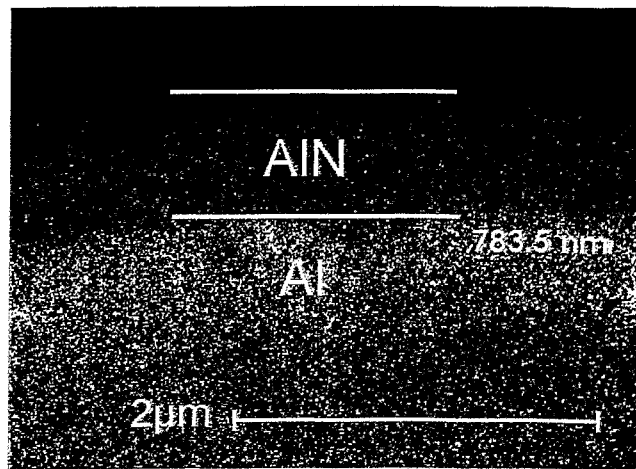


Figure 4.18: SEM micrograph from a cross-section of aluminium sample ion nitrided at 1.6 keV ion energy, 0.2 mA/cm² current density, 400 °C substrate temperature for 50 min. The layer has a nitrogen area density of 3.78x10²² at./cm² determined by NRA.

First, the area density of nitrogen atoms in the nitride layers was defined by NRA. Then, the atomic area density of the nitride is taken twice as the area density of nitrogen, since the formed layers have almost stoichiometric concentration of AlN ($N/Al \approx 1$). Second, the thickness of this layers was determined independently. For this reason, cross-sections of the samples investigated by NRA were prepared and analysed by SEM. An example of a micrograph obtained after ion nitriding at an ion energy of 1.6 keV, a current density of 0.2 mA/cm² and a substrate temperature of 400 °C for 50 min is shown in Fig. 4.18. The atomic density of the nitride is calculated applying the relation:

$$\text{atomic density} \left(\frac{\text{at}}{\text{cm}^3} \right) = \frac{\text{area density} \left(\frac{\text{at}}{\text{cm}^2} \right)}{\text{thickness} \text{ (cm)}} \quad (4.13)$$

After investigating a number of nitride layers, an average atomic density of 7.5x10²² at/cm³ has been determined. This value is about 20 % lower than the standard density of AlN bulk material (9.58x10²² at/cm³). No significant difference in the atomic density of layers produced at different substrate temperatures is observed. However, it has to be

pointed out that the accuracy of density determination is not very high, since the nitride layers are rather rough which induces an error of about 6 % in the thickness determination.

4.7.2 Morphology and adhesion

The morphology of the nitride layers was studied by SEM. The results presented here are obtained from layers produced at an ion energy of 1.6 keV, a current density of 0.2 mA/cm² and substrate temperature of 300 °C for different nitriding times. Fig. 4.19 a) shows the surface morphology of a layer obtained after 20 min. It can be seen that the surface is rough and completely covered with small nitride particles. Taking into account the scale of the image, it is assumed that this nitride particles consist of several AlN crystallites (the average crystalline grain size is about 5 nm, as shown in section 4.6). Such an inhomogeneous and undulated structure can be explained by a preferred diffusion of aluminium along grain boundaries towards the surface and low surface mobility. With prolongation of the nitriding time, the nitride particles in the layer grow further and coalescence between them occurs as shown in Fig. 4.19 b) after 60 min. The layer surface becomes smooth but furrowed by deep grooves. Further increase in the nitriding time confirms the tendency of coalescence. However, cracking of the plane layer is also observed in Fig. 4.19 c). As a consequence of cracking the nitride layer breaks into parts, which loose contact with the substrate. This effect can be better seen in the SEM cross-sectional image of Fig. 4.20, obtained from a sample ion nitrided for 80 min. Together with the cracks within the layer, also cracks which penetrate deeply into the aluminium substrate (at the left edge of the micrograph) are observed. Most probably the latter is a crack along the boundary between two grains of the aluminium substrate. Moreover, spalling of the layer occurs even without visible from the top view microcracks, as seen on the right edge of the micrograph.

After a nitriding time of about 60 min, a corresponding peculiarity is also observed in the nitrogen profiles. At a substrate temperature of 300 °C, 350 °C and 400 °C, a strong deviation from the rectangular shape occurs. Representative examples are shown in Fig. 4.21 for 400 °C and compared to a rectangular one. The nitrogen profiles change to a triangular shape with an apparent smooth slope at the interface between layer and aluminium substrate. Moreover, the transformation of the shape is also accompanied by a change in the nitride layer thickness. Rather than increasing with prolongation of nitriding time, the layer thickness suddenly decreases. Fig. 4.22 shows the results presented in Fig. 4.13 in section 4.5.3 plus additional data obtained for nitriding times longer than 60 min. It can be seen that after a certain upper time limit no clear correlation between layer thickness and nitriding time can be stated. This phenomenon is correlated with a change of the surface morphology. The spalled parts of the layer can peel off or become sputtered. Consumption by sputtering may occur because the contact with the substrate is lost and the supply of aluminium atoms is interrupted. Fig. 4.19 d) shows the surface morphology obtained from a sample ion nitrided for 120 min. Most probably, it reveals the underlying morphology of the nitride layer, open after delamination or sputtering of the upper part. Both effects, delamination and sputtering can explain the observed sudden decrease of the nitride layer thickness.

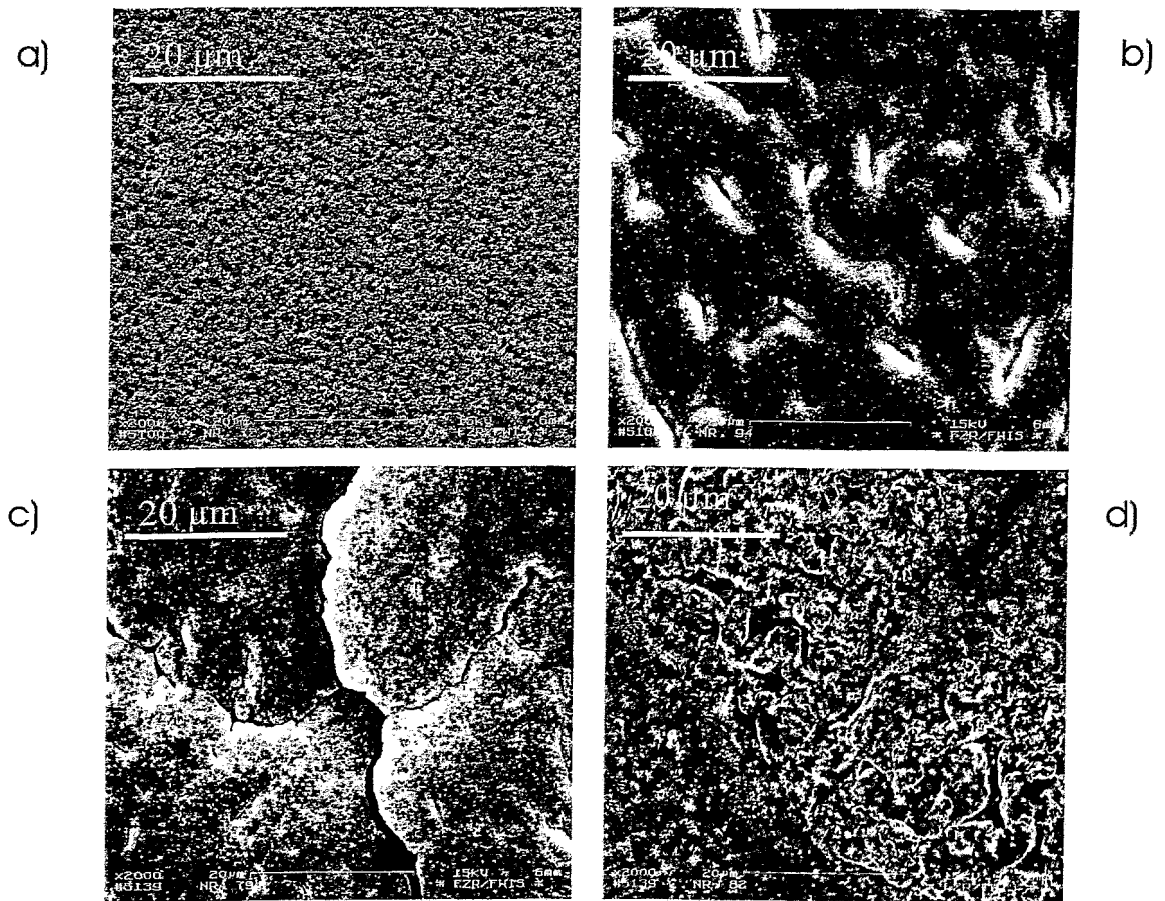


Figure 4.19: Surface morphology of the nitride layers grown at an ion energy of 1.6 keV, a current density of 0.2 mA/cm² and a substrate temperature of 300 °C for nitriding times of a) 20 min, b) 60 min, c) 80 min and d) 120 min.

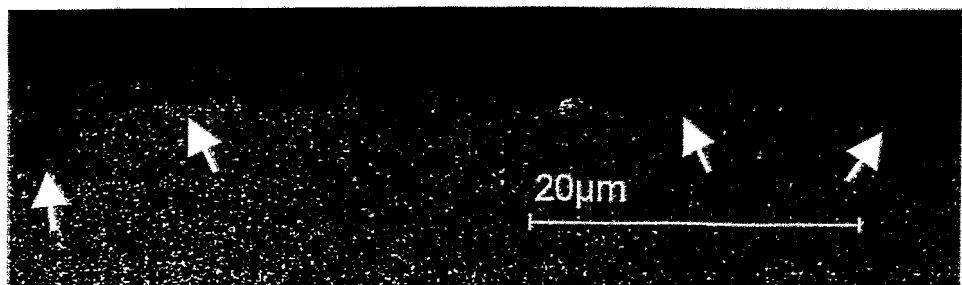


Figure 4.20: Cross-section of an aluminium sample nitrided at an ion energy of 1.6 keV, a current density of 0.2 mA/cm² and a substrate temperature of 300 °C for 80 min obtained by SEM.

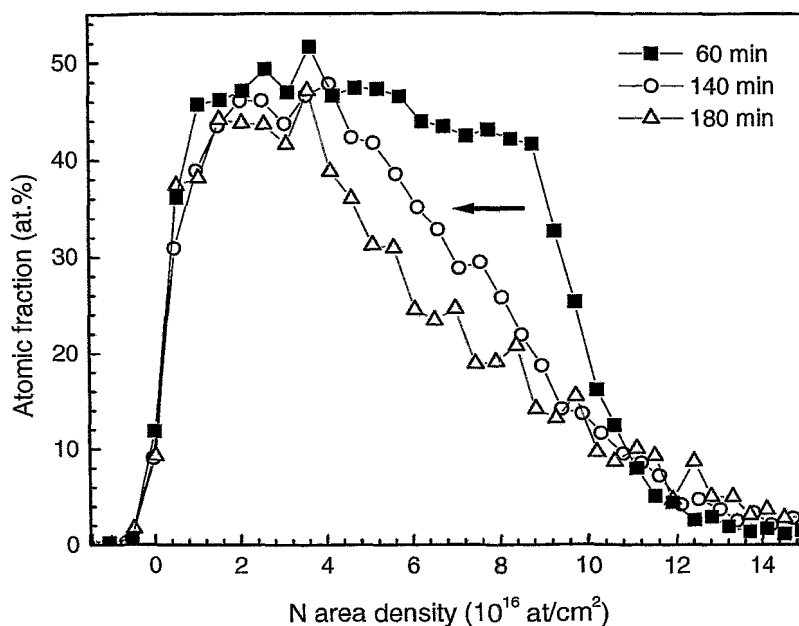


Figure 4.21: Example for the deviation of the nitrogen profile from rectangular to triangular shape. The profiles are obtained by NRA after ion nitriding at 1.6 keV, 0.2 mA/cm² and 400 °C.

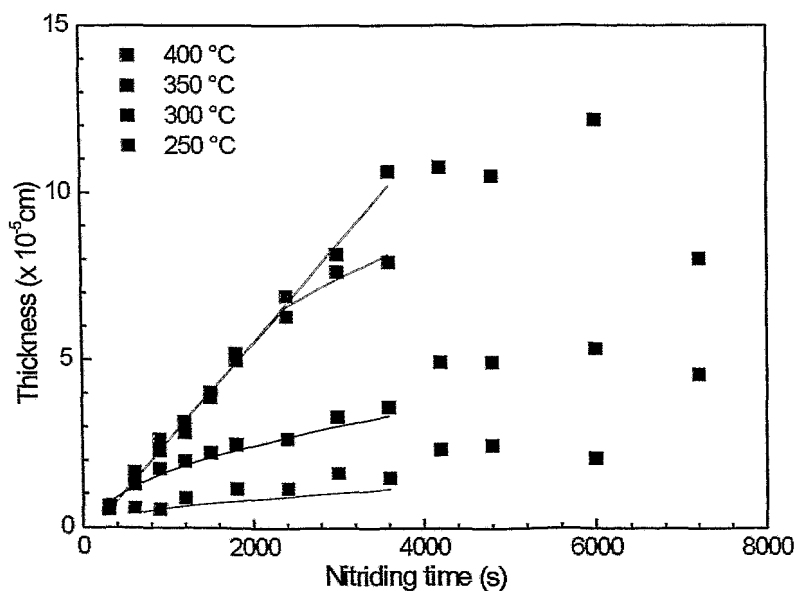


Figure 4.22: Nitride layer thickness as a function of the processing time for substrate temperatures of 250 °C, 300 °C, 350 °C, and 400 °C as presented in Fig. 4.13 plus additional data for nitriding time longer than 60 min. The delamination regime is gray patterned.

4.7.3 Stress

The effect of delamination is usually related to stress in the formed layers. Moreover, it is well known that stress has a great influence on the mechanical properties of these layers. It may modify properties as resistivity, magneto-electric and tribologic behaviour, etc. Therefore, it is important to obtain an information about the stress incorporated in the nitride layers produced by ion nitriding of aluminium.

The global stress (S) in layers at room temperature represents a sum of intrinsic stress (S_{in}) and thermal stress (S_{th}). The intrinsic stress builds up during the layer growth and depends on material properties and process conditions. In crystalline systems the formation of strain due to point defects and dislocation in the lattice causes intrinsic stress. In nano-crystalline layers, as the layers here, stress may depend also on texture and grain size. The thermal stress builds up during cooling of the sample after ion nitriding down to room temperature. It is caused by a thermal strain, which is generated from the difference in thermal expansion coefficients between layer and substrate. S_{th} can be estimated from the relation:

$$S_{th} = E_{AlN} (\alpha_{AlN} - \alpha_{Al}) (T - T_R), \quad (4.14)$$

which assumes that the thickness of the nitride layer is much less than the thickness of the aluminium substrate. Here E_{AlN} is the Young's modulus of AlN ($E_{AlN} \approx 350$ GPa [143]), $\alpha_{Al} \approx 25.5 \times 10^{-6} \text{K}^{-1}$ [144] and $\alpha_{AlN} \approx 5.7 \times 10^{-6} \text{K}^{-1}$ [143] are the linear thermal expansion coefficients of AlN and Al, T and T_R are the substrate temperature during ion nitriding and room temperature, respectively. Applying equation 4.14 for 400 °C, the thermal stress in such an AlN/Al system is calculated to be rather high, about - 2.6 GPa. This value can be reduced by decreasing the process temperature. The thickness at which the layer delaminates depends on the force acting on the layer-substrate interface. The layer force on the substrate is expressed in term of the force per unit width (FPUW) as: $\text{FPUW} = S \cdot x$, where x is the thickness of the layer. If the thermal stress is the main contribution to the global stress, lowering the thermal stress by growing the layer at lower temperature should result in thicker layers because the critical FPUW for delamination is reduced. In contradiction, the experiment shows that the nitride layers obtained at lower temperature are significantly thinner (see Fig. 4.22) but they also delaminate after an nitriding time of about 60 min. Moreover, it is observed that the surface morphology changes during further progress of nitriding (see Fig. 4.19 d)). Consequently, thermal stress can not be the main reason for the poor adhesion and delamination of the layers. Other reasons like intrinsic stress and growth morphology have to be addressed to explain the limited layer thickness.

X-ray diffraction is often applied for investigation of stress in thin films. In this method, the strain in the crystal lattice is measured and the residual stress producing the strain is calculated, assuming a linear elastic distortion of the crystal lattice. The nitride layers obtained in the present study have a small thickness and a fine crystallinity, which results in low diffraction intensity and strong peak broadening. All this does not allow a precise determination of stress. Nevertheless, some information about the macroscopic and microscopic strains present in the nitride layers can be obtained.

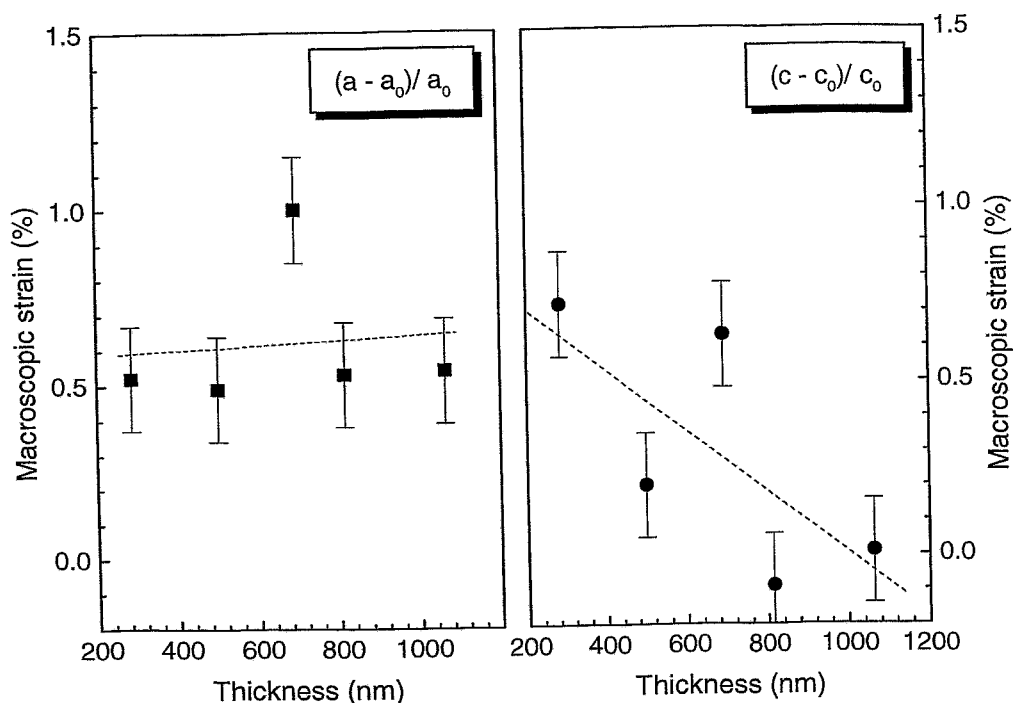


Figure 4.23: Macroscopic strain determined by XRD at 0.5° grazing incidence. The layers are obtained after ion nitriding at 1.6 keV, 0.2 mA/cm², 400 °C for times varied from 20 min to 60 min by intervals of 10 min.

Macroscopic stress acts over distances much larger than the grain size of the crystallites. It produces an uniform distortion, shifting the position of the diffraction peaks. In this study, the macroscopic strains are estimated from the position of the diffraction peaks by the PowderCell code. The measured diffraction patterns are fitted considering the two main phases: hex. AlN and f.c.c. Al. For both phases the XRD patterns were evaluated separately. By matching phase content, lattice constants, preferred orientation besides background and angular dependent peak width, the summed intensity is fitted to the measured one. From these full profile fits, the mean value of lattice parameters and information about the possible preferred orientation (texture components) are obtained. Further follows crystalline grain size and microscopic strain determined by applying the "Integral Width Method" (refer to section 3.2.2.2). However, for the correct evaluation of strain and texture a Bragg-Brentano diffraction pattern has to be used [145, 146]. For the grazing incidence technique used here, with the increasing detector angle ($\sim 2\theta$) the orientation of the selected net plane changes too ($\sim \theta$). Therefore, the measured diffraction pattern contains an information obtained from diffraction planes with different orientation and fitting of this pattern can give only mean values, which will be used here for the strain determination.

The macroscopic strains are determined as $(a - a_0)/a_0$ and $(c - c_0)/c_0$, where a and c are the fitted lattice constants for the hexagonal AlN phase and a_0 and c_0 are the stress-free lattice constants for this phase taken from the PDF data base. The obtained results are shown in Fig. 4.23 as a function of layer thickness. In fact, the magnitude of the

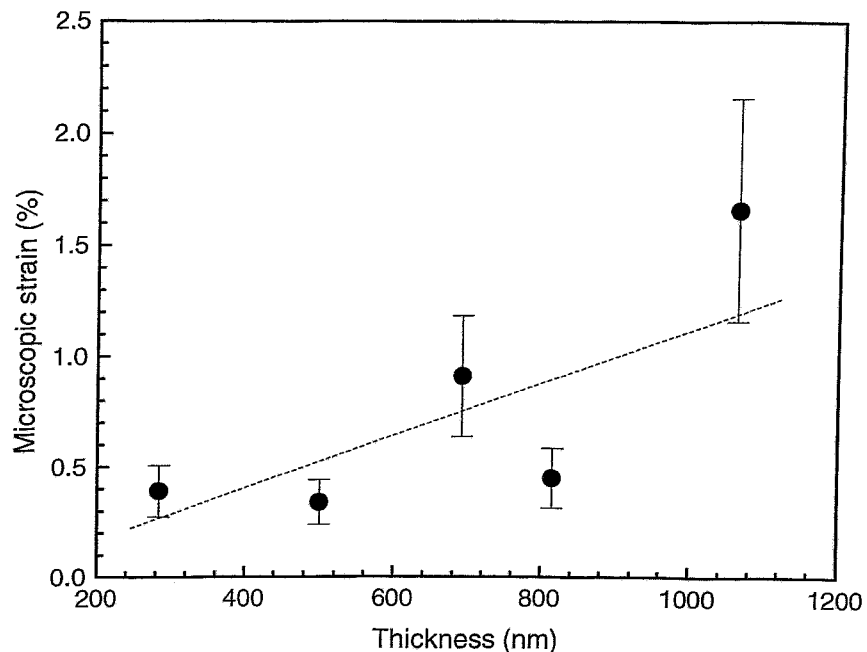


Figure 4.24: Microscopic strain determined by XRD at 0.5° grazing incidence. The layers are obtained after ion nitriding at 1.6 keV, 0.2 mA/cm^2 , 400°C for times varied from 20 min to 60 min by intervals of 10 min.

macroscopic strain is low, less than 1.5 %. Furthermore, the measured lattice constants are larger than the stress-free parameters. Increased lattice constants are indication for extension of the crystal lattice, which corresponds to a tensile stress. This is consistent with the result obtained from the density determination of the nitride layers, since a density that is lower than the nominal one results in tensile stress. Fig. 4.23 shows that the macroscopic strain described by the lattice constant a does not depend on the layer thickness. In contrast, that one obtained from c decreases as the layer thickness increases. This different behaviour could indicate a preferred orientation of the crystallites in the layer. The observed decrease of $(c - c_0)/c_0$ for larger layer thickness may be correlated with the partial delamination in the layer. The interpretation of the results has to take into consideration, that the XRD analysis gives an information integrated over the illuminated area and the depth of penetration of the X-ray beam.

Microscopic stress arises from fluctuation of the global stress within the layer. Therefore the microscopic strain varies from point to point within the crystals producing fluctuations in the lattice spacings and broadening of the diffraction peaks. In this study, the effect of microscopic strain on the peak broadening is separated by applying the "Integral width method". Fig. 4.24 shows the obtained microscopic strains for layers with a different thickness. The obtained values of microscopic strain are in the order of this obtained for the macroscopic ones (compare to Fig. 4.23). As it can be also seen the scattering of these values is quite large but a tendency of increasing microscopic strain with increase of layer thickness can be noted, i.e. thicker layers have higher microscopic stress.

In summary, the thermal stress is not the main reason for the layer delamination described in subsection 4.7.2. The performed XRD analysis reveals existence of microscopic and macroscopic stress in the nitride layers. The determined mean values of macroscopic strains indicate lattice extension, thus tensile stress. It is observed that the microscopic strain increases for larger layer thickness and its magnitude is comparable to this of the macroscopic one.

4.7.4 Stoichiometry

As already mentioned in section 4.5, the nitrogen concentration profiles evaluated by NRA after ion nitriding at different temperatures exhibit a difference in maximum concentration. Fig. 4.12 on page 61 shows that the layers produced at 400 °C have an average maximum concentration of about 48 at.%. For the layers produced at 350 °C and 300 °C it decreases to about 44 at.% and 42 at.%, respectively. The nitrogen profiles measured after ion nitriding at 250 °C show a significantly lower apparent concentration of nitrogen, but it has to be taken into consideration that this low value is strongly affected by the depth resolution of the NRA measurement due to the small layer thickness (less than 200 nm). The dependence of nitrogen concentration on the process temperature was verified by ERDA. Fig. 4.25 shows the ERDA profiles for selected samples ion nitrided at 300 °C and 400 °C. The average maximum concentration of nitrogen, determined by ERDA, is about 55 at.% and 50 at.% for substrate temperatures of 400 °C and 300 °C, respectively. In contrast to the NRA profiles, due to the better depth resolution here a well established plateau with almost equal concentration of nitrogen and aluminium is measured for the case of 300 °C. The layers produced at 400 °C clearly show an over-stoichiometric concentration of nitrogen atoms. However, ERDA has the advantage to measure the profiles of N, Al, O and H separately in contrast to the NRA where only the nitrogen is detected. The over-stoichiometry may be caused by an enhanced mobility of atomic nitrogen at higher substrate temperature, which allows nitrogen to penetrate deeply into the layer and to be solved in the AlN. However, most probably the excess amount of nitrogen forms N₂ molecules, which can be trapped in cavities as the structure of the nitride layers is porous. In order to investigate this phenomenon, a layer with over-stoichiometric concentration of nitrogen was annealed at 500 °C for 24 h at vacuum and subsequently analysed by ERDA. The obtained concentration profiles of nitrogen and aluminium do not show a noticeable change after annealing. Again, the concentration of nitrogen is slightly higher than this of the aluminium. Most probably, the N₂ molecules can not diffuse out due to their relatively large size. On the other hand, the thermal energy at 500 °C is estimated to be about 0.1 eV, which is not sufficient to dissociate N₂ molecule with a binding energy of 9.84 eV and create a mobile atomic nitrogen.

It should be also noted that the amount of oxygen and hydrogen within the nitride layers is negligible in comparison to nitrogen. Only a slightly higher maximum concentration of oxygen atoms in the near surface region is observed for the layer nitrided at 300 °C. In the bulk of the nitride layers the oxygen concentration is very low, less than 2 at.%. No other contamination from heavier elements is observed by RBS analysis.

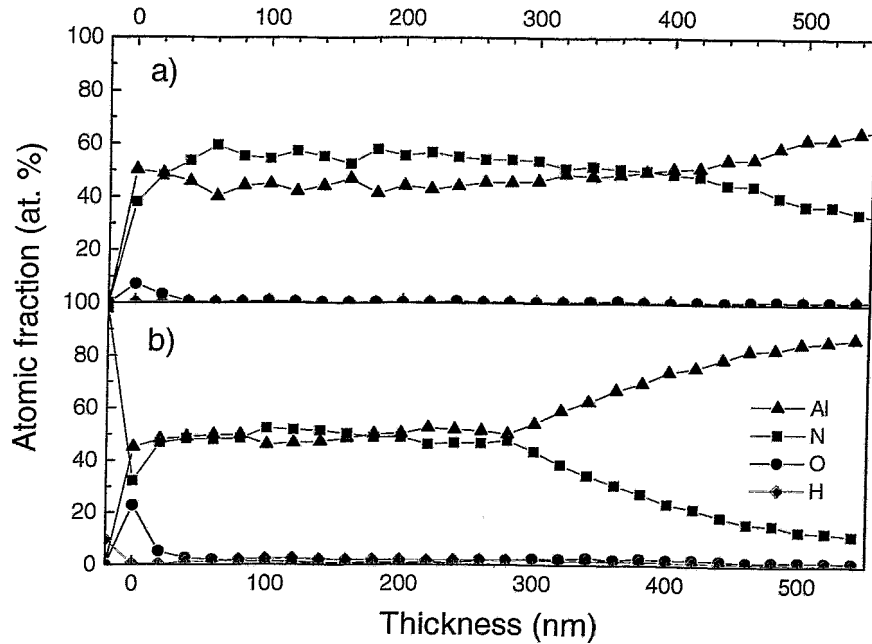


Figure 4.25: ERDA profiles of aluminium, nitrogen, oxygen and hydrogen obtained after ion nitriding of aluminium at a) 400 °C and b) 300°C.

4.7.5 Electrical properties

An investigation of the electrical properties of the nitride layers grown by ion nitriding of aluminium was also performed. For this reason, contacts of aluminium were deposited on the top of the layers through a hole mask by magnetron sputtering. In result a structure of Al (contact) - AlN (layer) - Al (bulk) was formed. The contacts have a round shape with a diameter of 0.8 mm and an area of $5 \times 10^{-7} \text{ m}^2$. Current measurements through this structure were performed using a Keithley I - V source type SMU- 237. Fig. 4.26 shows an example of a measured current-voltage (I - V) curve for a sample with 690 nm thick nitride layer. It can be clearly seen that the obtained I - V characteristic is nonlinear with low values of the electrical current, which reveals the insulating nature of the nitride layer. The resistance (R) of the layer is roughly estimated by applying a constant voltage V and measuring the current through the Al-AlN-Al structure. It is found to be higher than $1.7 \times 10^{10} \Omega$. Only the lowest value of R is given, because the current tends to decrease very slowly with time as typical for capacitors. An estimation of R can be also done from the slope of the I - V curve and it is found to be about $3.4 \times 10^{10} \Omega$ (see Fig. 4.26).

The specific electrical resistivity (ρ), which is the material property, can be estimated by the relation:

$$\rho = R \frac{A}{L} \quad (4.15)$$

and assuming a wire with a length (L) equal to the thickness of the nitride layer and a cross sectional area (A) equal to the area of the deposited contact. Using the above determined resistance, ρ is calculated to be higher than $1.2 \times 10^{10} \Omega \cdot \text{m}$. This value is in

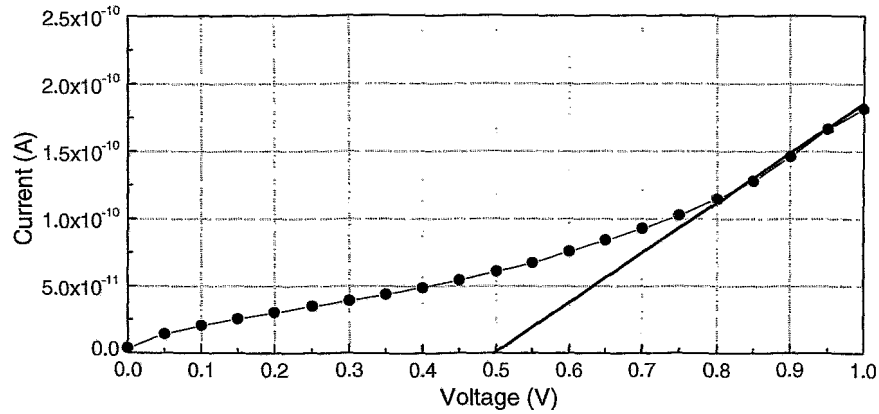


Figure 4.26: I - V characteristic of an Al-AlN-Al structure with a nitride layer of 690 nm.

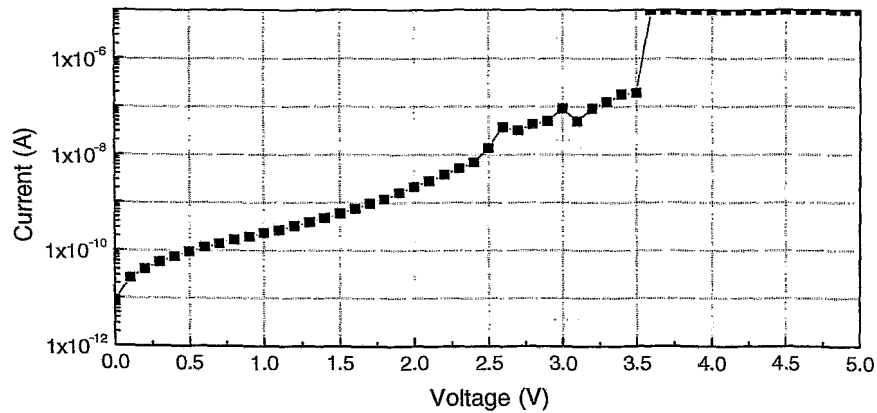


Figure 4.27: Breakdown characteristic of an Al-AlN-Al structure with a nitride layer of 690 nm.

the range of the specific electrical resistivity for AlN given in the literature ($2 \times 10^9 \Omega \cdot \text{m}$ - $1 \times 10^{11} \Omega \cdot \text{m}$) [17]. In the estimation the effect of aluminium contact and bulk is not taken into consideration, since the specific resistivity of aluminium is very low, about $2.6 \times 10^{-8} \Omega \cdot \text{m}$.

A breakdown test of the nitride layer was also performed and an example of an I - V curve is shown in Fig. 4.27. The measurement reveals that the nitride layer breaks at very low voltage of 3.5 V. Considering the thickness of the nitride layer, the breakdown per unit distance is calculated to be about 5 kV/mm, which is very low in comparison to the this of AlN bulk material (14 - 16 kV/mm) [147, 148]. Most probably, this is caused by the specific morphology of the nitride layers (see subsection 4.7.2). For instance, the current flux can preferentially flow along grain boundaries. Moreover, it has to be taken into account that any imperfection of the layers as defects, roughness, macrocracks, distortions, etc. can have a significant influence on the electrical properties. In confirmation of this it should be said that for some other places in the nitride layer a linear I - V characteristic was obtained, indicating high conductivity. Most probably, this is caused by the cracks and partly delamination of the nitride layers.

4.7.6 Tribological and corrosion properties

It is known that formation of a nitride layer on the surface of aluminium and aluminium based alloys leads to improvement of hardness, wear and corrosion resistance [1, 2, 149]. Here, an investigation of the tribological properties of the nitride layers formed by ion nitriding of aluminium will be presented.

A study of depth-dependent changes of hardness as result of the ion nitriding was done by measuring the dynamic microhardness with an ultra-microhardness tester Shimadzu DUH-202. During such a measurement the load P of the indenter increases with constant rate up to a preset maximum value and the resulting penetration depth X is recorded. For the measurements a Vickers indenter was used. The dynamic hardness is than defined as $DH = P/A = 37.838 (P/X^2)$, where A is the area of the indenter [150]. A maximum load of 3 mN was used. The results were corrected for the deviation of the diamond tip from the ideal shape. The influence of the elastic deformation on the dynamically measured hardness is small for a soft material like aluminium, therefore no such corrections were carried out in the determination of the depth dependent hardness.

In order to show the influence of the ion nitriding treatment on the mechanical surface properties of aluminium the relative hardness was determined, i.e., the dynamic hardness of the nitrided samples measured in a given depth normalized by the corresponding value of the untreated sample. Fig. 4.28 shows the depth dependence of the relative hardness increase for samples with different thickness of the nitride layer. It should be noted that actually the penetration depth of the indenter is deeper than required for correct hardness determination (less than one tenth of the layer thickness). In the case here, the measured hardness is a combination of the layer hardness and that of the soft aluminium substrate. Therefore, in the present investigation absolute values of hardness are not determined. The results are used only for comparison with respect to the untreated aluminium. In Fig. 4.28 it can be seen that for all nitrided samples the hardness increases beyond the surface up to a depth of about 100 nm. The highest increase by a factor of 12 is observed for the sample with the thickest nitride layer. Moreover, the penetration depth of the indenter at the maximum load of 3 mN decreases with increasing nitride layer thickness demonstrating the protective behaviour of the nitride layer. For a 500 nm thick layer the indenter breaks through and penetrates into the aluminium substrate, whereas the penetration depth is limited to 20 % and 15 % of the thickness for 692 and 1060 nm thick nitride layers, respectively. The observed results demonstrate the benefit of ion nitriding for the mechanical properties of aluminium. By increasing the nitride layer thickness, the hardness also increases.

An investigation of the wear behaviour of the nitride layers was not possible due to their small thickness.

A corrosion test was performed by potentiodynamic polarisation technique using an EG&G Potentiostat [151]. The polarisation curves were obtained at room temperature in 3.5 wt.% NaCl solution with 6.7 pH. This solution approximates sea water and was chosen because aluminium surfaces can not repassivate when exposed to chloride electrolytes. The potential was measured against a standard calomel electrode (SCE). Air was bubbled through the solution to hold the oxygen concentration in the solution approximately constant and to avoid localized concentration polarization effects. The corrosion potential

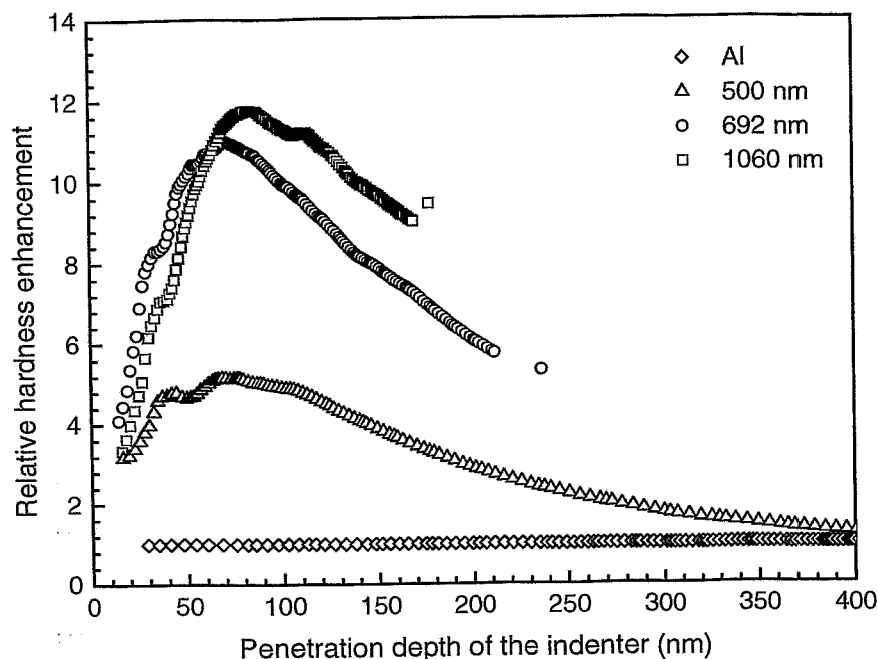


Figure 4.28: Depth dependence of the relative hardness enhancement as a result of ion nitriding for nitride layers with different thickness.

was determined by fitting the measured curves using the software of EG&G.

Fig. 4.29 shows the potentiodynamic scans from an untreated and an nitrided aluminium sample with 1 μm thick nitride layer. The polarisation curve obtained from the untreated aluminium sample is typical for conductive materials. It consists of cathodic and anodic polarisation parts. The potential at which the transition occurs, i.e., the cathodic current is equal to the anodic current, is known as corrosion potential (E_{corr}). It is found to be - 892 mV. The polarisation curve obtained from the nitrided sample shows a different behaviour. Due to the insulating property of the nitride layer, no anodic part is observed. The polarisation curve has a broad range of potentials where the current density is low and almost constant. Over this range, the surface repassivates until the potential is increased up to the pitting potential (E_{pit}), at which the nitride layer breaks down and pitting occurs. The obtained E_{pit} is about - 400 mV and - 320 mV for the untreated and ion nitrided sample, respectively. Moreover, the polarisation curve obtained from the nitrided sample has a lower current density, which corresponds to an increase of corrosion resistance. The observed shift of E_{pit} to a more positive value for the ion nitrided sample with respect to the untreated one together with the enhanced corrosion resistance, clearly indicates the benefit of the nitride layer on passivation in NaCl solution.

The mechanism responsible for the corrosion of aluminium in chloride solution is well studied [152, 153]. In brief, it is based on the electrochemical reaction between aluminium with the Cl^- ions resulting in formation of chlorine salt (AlCl_3). Negatively charged chlorine ions on the surface set up an electric field that drives the migration of Al^{3+} through the native oxide layer. The surface oxide is not enough for passivation, since it

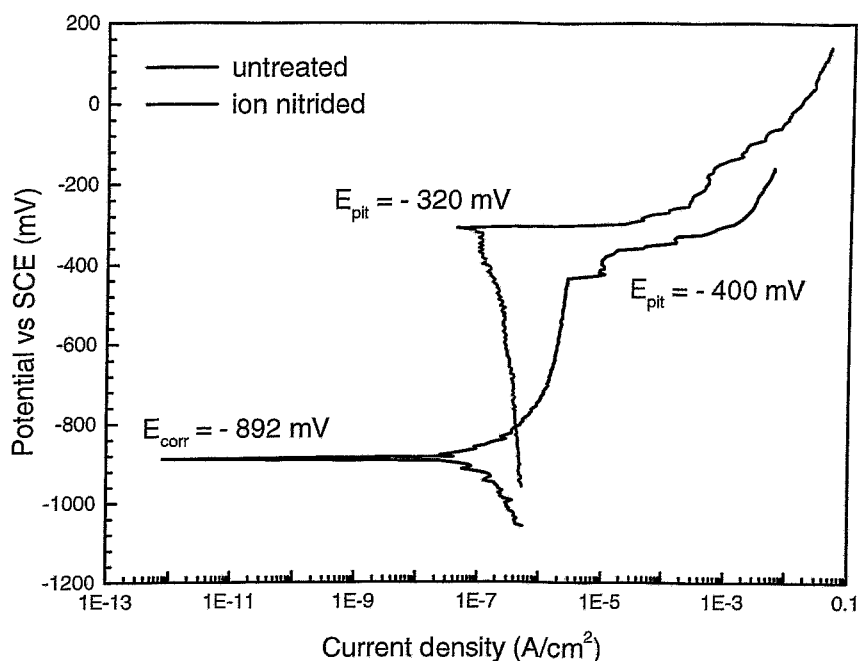


Figure 4.29: Potentiodynamic scans for untreated and nitrided aluminium samples with a nitride layer of $1 \mu\text{m}$.

is soluble in acidic solutions. When a continuous layer of AlN is present on the surface of aluminium, a similar process occurs. However, AlN first has to dissociate in order to provide Al^{3+} ions or the created electric field must be sufficient to draw aluminium from the underlying bulk. This adds an additional energy barrier, so the corrosion potentials are shifted to more noble values. Moreover, the insulating properties of AlN impede the flow of electrons and ions, thus reducing the corrosion current.

4.8 Ion nitriding of the AlMg_{4.5}Mn alloy

4.8.1 Introduction

For industry and technological purposes components made of pure aluminium are rarely used. By addition of alloying elements the properties of the pure aluminium can be positively modified. There is a broad range of alloys with various properties which are suitable for a wide spectrum of applications. With respect to surface modification by nitriding, several studies have been carried out using different aluminium alloys [2, 62, 72, 73, 86, 154, 155, 156]. The main problem is related to the fact that the high temperature required for the nitriding process deteriorates other properties of the alloys such as toughness, elastic qualities and phases [157]. Therefore the application of nitriding is restricted to a certain aluminium alloys. In Ref. [63] the nitriding behaviour of several alloys has been investigated by plasma nitriding. The highest growth rate is observed for AlMg_{4.5}Mn, which is about 0.17 nm/s at a substrate temperature of 400 °C. Moreover, PIII of the same alloy results in formation of 15 µm thick nitride layer (at 500 °C and 5 h nitriding time), which has not been achieved in the case of pure aluminium [89].

In the present study, experiments of ion nitriding of AlMg_{4.5}Mn were performed too. Investigation of the nitride layer growth kinetic at 400 °C was carried out at the same ion beam parameters as in the case of pure aluminium. Analysis of phase formation, structure, macro- and microscopic strains and surface morphology were performed. The results are compared with those obtained by ion nitriding of pure aluminium.

4.8.2 Experimental results

The composition of the AlMg_{4.5}Mn alloy is given in Table 4.3 according to Ref. [158]. The ion nitriding was performed at an ion energy of 1.6 keV and a current density of 0.2 mA/cm² for different nitriding times, increasing from 20 min up to 4 h. A substrate temperature of 400 °C was chosen because, as observed in section 4.5, this temperature enables a high growth rate and thus the formation of thick nitride layers.

Element	Symbol	Concentration (mass %)
Silicon	Si	0.25
Iron	Fe	0.40
Copper	Cu	0.05
Manganese	Mn	0.6 - 1
Magnesium	Mg	4.3 - 5.2
Chromium	Cr	0.05 - 0.25
Zinc	Zn	0.25
Titanium	Ti	0.15
Aluminium	Al	balance

Table 4.3: Composition of AlMg_{4.5}Mn according to Ref. [158].

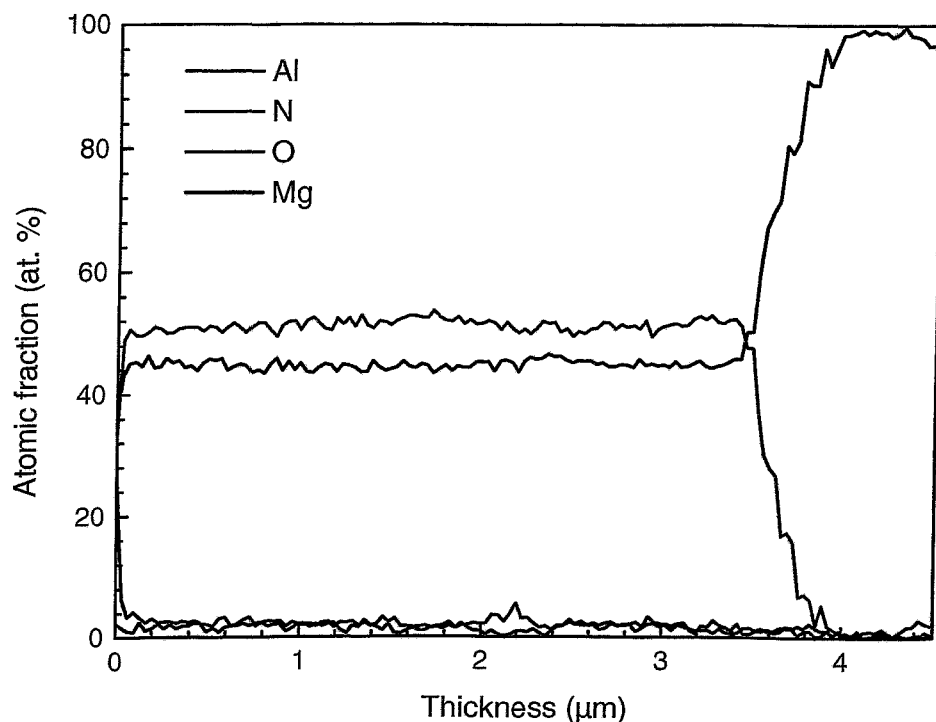


Figure 4.30: Depth profiles of aluminium, nitrogen, oxygen and magnesium obtained by AES after ion nitriding of $\text{AlMg}_{4.5}\text{Mn}$ at 1.6 keV, 0.2 mA/cm^2 , $400 \text{ }^\circ\text{C}$ for 4 h.

The elemental depth profiles were determined by AES, since the layers exceed the detection depth range of ion beam analysis. An example of such a profile obtained after ion nitriding for 4 h is shown in Fig. 4.30. It can be seen that it has a pronounced rectangular shape and a thickness of about $4 \mu\text{m}$. The nitrogen to aluminium ratio corresponds to the one reported in section 4.7.4 for a substrate temperature of $400 \text{ }^\circ\text{C}$, since the results obtained by ERDA were used for calibration of the relative sensitivity factors of AES. The amount of oxygen contamination in the nitride layer is low, less than 2 at.% and slightly higher at the surface. Magnesium is homogeneously distributed through the layer. The concentration of the other elements in the alloy is too low to be detected.

The growth kinetics of the nitride layer is shown in Fig. 4.31 by squares. For comparison, the results obtained by ion nitriding of pure aluminium at the same substrate temperature and ion beam parameters are shown by triangles. It should be noted, that in the case of pure aluminium the thickness was determined from the results of NRA and the atomic density of the nitride layers. For nitriding time shorter than 80 min there is a very good agreement, while for larger time a difference in the nitriding behaviour is observed. The nitride layers formed by ion nitriding of $\text{AlMg}_{4.5}\text{Mn}$ grow thicker than the maximum thickness achieved in the case of pure aluminium. Only a linear dependence between layer thickness and nitriding time is observed, which is in good agreement with the transition time t_0 of about 4:50 h determined in section 4.5.4 for substrate temperature of $400 \text{ }^\circ\text{C}$.

Phase formation and structure were investigated by means of XRD. The diffraction pattern (not shown here) reveals formation of hexagonal AlN . Bragg reflections from aluminium were also observed due to a superposition of signals caused by the substrate.

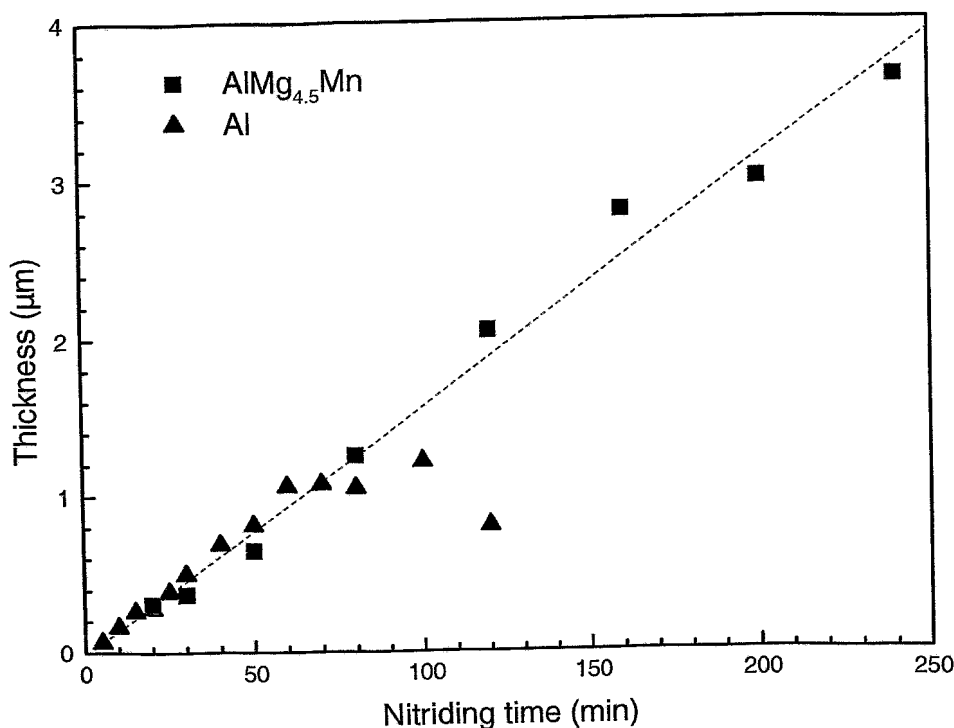


Figure 4.31: Nitride layer thickness as a function of the processing time for AlMg_{4.5}Mn (squares) determined by AES and pure Al (triangles) determined by NRA and the density of the nitride layers. Ion nitriding parameters: 1.6 keV, 0.2 mA/cm², 400 °C.

No special effort for determination of the cubic AlN phase was carried out. Diffraction peaks, which could be related to the alloying elements are not observed, since XRD is not sensitive to the phases with a volume fraction less than 10 % [159]. An average crystallite size of 8 nm is determined for a layer grown for 20 min. For the same layer, a microscopic strain of 0.3 % is found. An analysis of the macroscopic strain results in a value of 0.5 % for the lattice parameter a . A virgin sample of AlMg_{4.5}Mn was also investigated by XRD in order to check, if there is a difference in the lattice parameters of the pure aluminium and the alloy. The result reveals that the lattice constant of AlMg_{4.5}Mn is only 0.48 % larger than that of pure aluminium.

Fig. 4.32 shows a comparison between the surface morphology of layers obtained by ion nitriding of AlMg_{4.5}Mn and pure aluminium at different magnifications. The layers were grown for 80 min at the same substrate temperature and ion beam parameters. It can be seen that the macrostructure of the two layers is different. Ion nitriding of AlMg_{4.5}Mn results in formation of macroscopic nitride particles (Fig. 4.32 a) which make the sample surface rougher and seems to be not so dense like in the case of aluminium (Fig. 4.32 b). The image taken at lower magnification from the layer grown on the alloy reveals that the nitride particles are almost homogeneously distributed over the sample surface (see Fig. 4.32 c). No cracking or distortion of the layer are observed as for the pure aluminium (see Fig. 4.32 d). Nevertheless, it should be noted that after long nitriding times (200 min and 240 min) an indication for partly delamination of the nitride layers is observed too.

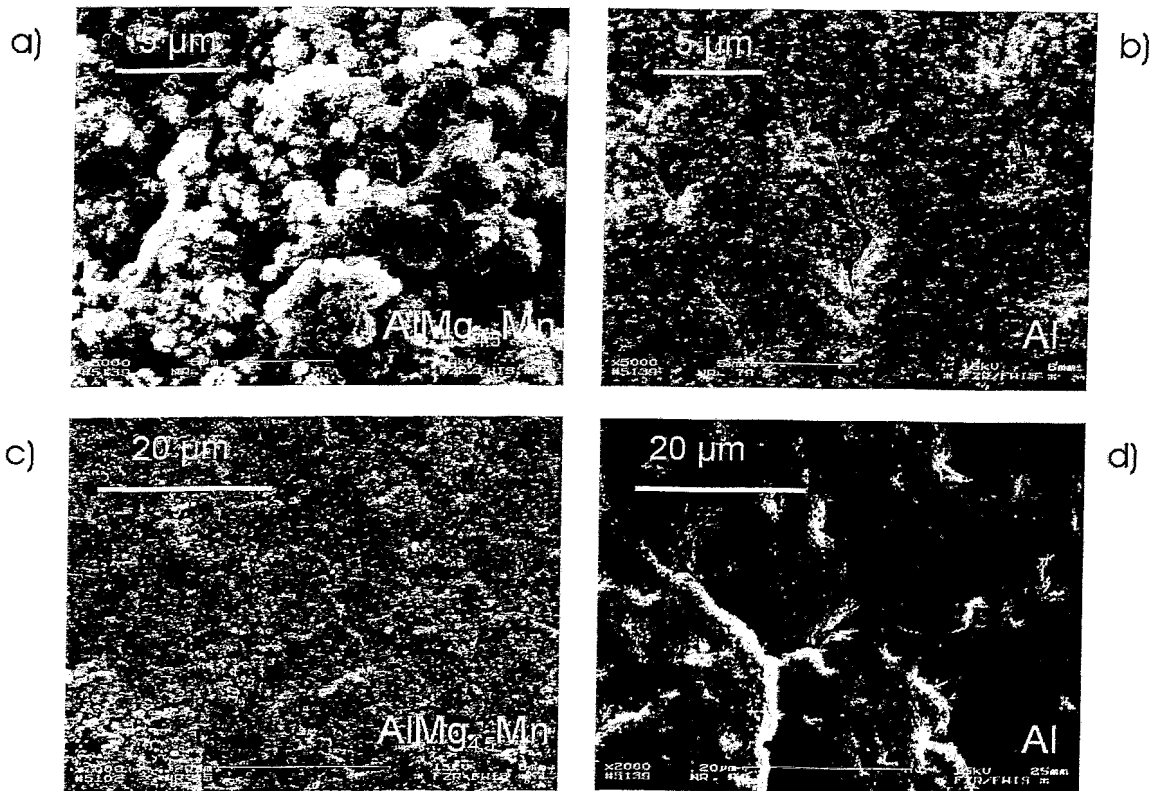


Figure 4.32: Surface morphology of nitride layers grown by ion nitriding of $\text{AlMg}_{4.5}\text{Mn}$ and pure Al. The layers are produced at 1.6 keV, 0.2 mA/cm^2 , 400°C for 80 min.

This is in agreement with Refs. [59] and [63], where is reported that the nitride layers produced by plasma nitriding are uniform up to a maximum thickness of about $3 \mu\text{m}$, after which cracking occurs.

4.8.3 Discussion

The results presented above show that ion nitriding of $\text{AlMg}_{4.5}\text{Mn}$ leads to formation of nitride layers thicker than these achieved in the case of pure aluminium. The obtained elemental depth profiles reveal the existence of a sharp interface between the layer and substrate, even for the $4 \mu\text{m}$ thick nitride layer. The analysis of the surface morphology shows that the layer obtained on the $\text{AlMg}_{4.5}\text{Mn}$ substrate is free of cracks and distortions as compared to that obtained at the same process parameters in the case of aluminium. All this indicates that the layer grown by ion nitriding of $\text{AlMg}_{4.5}\text{Mn}$ interacts with the substrate in a different way. One possible reason could be a better matching between the lattice constants. However, the XRD analysis of an $\text{AlMg}_{4.5}\text{Mn}$ virgin sample shows that the difference in the lattice constant in comparison to that of the pure aluminium is negligible small. Consequently, the better performance of the alloy is not due to the structure of the bulk material. On the other hand, the analysis of the nitride layer shows that it consists of crystallites with hexagonal AlN structure with an average grain size

similar to the one formed after ion nitriding of pure aluminium. The only distinction, which is observed, is in the surface morphology of the nitride layers grown by ion nitriding of the alloy. These layers are composed from several macroscopic nitride particles, even after a relatively long nitriding time of 80 min (see Fig. 4.32 a and c). In the case of pure aluminium, macroparticles are observed only for short nitriding times (about 20 min), while the layer grown for 80 min (see Fig. 4.32 b and d) is more smooth, apart from the observed cracks. Obviously, the less dense arrangement of particles results in lower stress and formation of nitride layers without cracking. In fact, the obtained value for the microscopic strain of 0.3 % is lower than that of aluminium (compare to Fig. 4.24 on page 79) but because of the large error in its determination, no clear conclusion can be drawn. The macroscopic strain determined by XRD is in the range of that obtained by using pure aluminium. Nevertheless, the specific growth morphology appears to be the reason why thicker nitride layers can be grown by ion nitriding of AlMg_{4.5}Mn. The influence of the alloying elements and their role for the formation of such a morphology was not investigated.

4.8.4 Summary

The nitriding kinetic of the AlMg_{4.5}Mn alloy at an ion energy of 1.6 keV, a current density of 0.2 mA/cm² and a substrate temperature of 400°C was investigated. For nitriding times less than 80 min the results are similar to those obtained by ion nitriding of pure aluminium. For longer nitriding times, a different behaviour is observed. The nitride layers grow thicker than the maximum layer thickness achieved in the case of aluminium. This effect is related to the specific growth morphology of the layers formed by ion nitriding of AlMg_{4.5}Mn alloy.

5 Summary & Conclusions

The present study is devoted to the investigation of the mechanism of aluminium nitriding by a technique that employs implantation of low-energy nitrogen ions and diffusional transport of atoms. The nitriding of aluminium is investigated, because this is a method for surface modification of aluminium and has a potential for application in a broad spectrum of fields such as automobile, marine, aviation, space technologies, etc. However, at present nitriding of aluminium does not find any large scale industrial application, due to problems in the formation of stoichiometric aluminium nitride layers with a sufficient thickness and good quality. For the purposes of this study, ion nitriding is chosen, as an ion beam method with the advantage of good and independent control over the process parameters, which thus can be related uniquely to the physical properties of the resulting layers. Moreover, ion nitriding has a close similarity to plasma nitriding and plasma immersion ion implantation, which are methods with a potential for industrial application.

The main results and conclusions of this study are summarised below:

An investigation of ion beam current density, energy and uniformity in dependence on the parameters of the ion source is performed. A stable operation regime is established by choosing the optimum values for the gas flux and electrical potentials applied to the ion source. The ion beam is characterised in terms of composition and energy distribution. The obtained results show that it consists of N_2^+ and N^+ ions with a composition of about 80 % and 20 %, respectively. The ion beam can be considered as quasi monoenergetic, since the ion energy distributions of both N_2^+ and N^+ consist of a single narrow peak with a full width at half maxima of about 10 eV. These results are used for a quantitative determination of the nitrogen incorporation and loss during ion nitriding of aluminium.

An analysis of the gas composition in the experimental chamber is also performed and shows that the main gas species are N_2 molecules. The other species as H_2 , H_2O , O_2 and CO_2 are detected in a very small amount and therefore their impact on the contamination during the ion nitriding of aluminium can be neglected. The partial pressure of atomic nitrogen at the sample position is estimated to be about 2×10^{-9} Pa.

The influence of the surface oxide layer on the nitriding of aluminium is investigated by means of in-situ real time elastic recoil detection analysis. Experiments are performed at different oxygen partial pressures and at fixed ion beam energy and current density. It is observed that, if an oxide layer is present on the surface of aluminium it hampers or stops the nitriding process. If the sample surface is free of oxide, nitriding takes place at a constant growth rate. It is confirmed that the thickness of the oxide layer is controlled by the interplay between the rate of surface oxidation due to adsorption of oxygen atoms from the residual gas and the rate of surface removal due to sputtering induced by the

ion beam. This result demonstrates the positive effect of low-energy ion bombardment, since it induces cleaning of the surface oxide simultaneously to the nitriding. For an ion energy of 1.6 keV and a current density of 0.2 mA/cm², which are mainly used in the present study, the critical partial pressure of oxygen is found to be about 3×10^{-5} Pa.

The mechanism of diffusional transport during ion nitriding of aluminium is investigated by means of a marker layer. For this reason gold atoms with a low concentration are implanted in a stoichiometric AlN layer, which is grown on bulk aluminium. Then, ion nitriding is performed and its influence on the position of the marker layer is investigated. The result shows that the gold layer is shifted in direction of the bulk due to the nitriding. Additionally, it has been proved that the gold atoms do not diffuse themselves due to the high process temperature. Therefore, it is concluded that the diffusional transport during nitriding of aluminium is dominated by the diffusion of aluminium rather than nitrogen. This mechanism is confirmed by applying an isotope sequence technique. Ion nitriding of aluminium is performed with ¹⁴N and ¹⁵N isotopes and their location in depth is investigated. The obtained results reveal that the formation of AlN takes place close to the surface with the nitrogen being deposited there by the ion beam and the aluminium being provided by diffusion from the underlying bulk through the nitride, which is formed before. This phenomenon was found out for the first time in the present study. It is opposite to the commonly accepted opinion that during nitriding of aluminium the nitrogen atoms diffuse in direction of the bulk.

The growth kinetics of the nitride layer is investigated during ion nitriding of aluminium at an ion energy of 1.6 keV and ion current density of 0.2 mA/cm² for temperatures of 250 °C, 300 °C, 350 °C and 400 °C. Two regimes of nitride layer growth are distinguished. First, in the beginning of the process, the nitride layer grows linearly in time with the same growth rate for all temperatures. In this regime the nitride layer growth is controlled by the rate of nitrogen delivery from the ion beam reduced due to sputtering. Second, after a certain nitriding time, which depends on the substrate temperature, the nitride layer thickness transforms into a nearly square root function of time. This reveals that in the second regime the rate of aluminium diffusion is lower than the rate of nitrogen supply and therefore it plays a limited role for the nitriding kinetic. The two regimes are characterised as a function of process parameters, which provides a key for achieving control over the aluminium ion nitriding process. A modelling approach results in determination of a diffusion activation energy of 1.1 eV and diffusion coefficients of aluminium in AlN, which are between 2.8×10^{-14} cm²/s and 6.4×10^{-14} cm²/s for the temperature range from 250 °C to 400 °C.

An investigation of nitrogen incorporation and loss during ion nitriding of aluminium is performed. For the linear regime of nitride layer growth the loss of nitrogen is determined quantitatively by considering the ion beam composition and the measured amount of incorporated nitrogen. Dynamic binary collision simulations are performed to estimate the sputtering and backscattering yields of nitrogen. For an ion energy of 1.6 keV the sputtering yield of nitrogen is calculated to be 0.36, while the fraction of backscattered nitrogen is found to be about 4 % of the incident fluence. This result is in reasonably good agreement with the experimentally determined loss of nitrogen (within 20 %) for two current densities of 0.1 mA/cm² and 0.2 mA/cm². Experiments at different ion energies varied from 0.4 keV to 2.4 keV and a current density of 0.2 mA/cm² are also carried out.

Again, the estimated sputtering and backscattering yields are close to the experimental results, except for the two lowest energies of 0.4 keV and 0.6 keV. The contribution of neutrals (N_2 molecules and N atoms) to the incorporation of nitrogen because of adsorption is found to be negligible. Consequently, it is concluded that in the linear growth regime the mechanism of nitrogen incorporation and loss is mainly defined by the ion-solid state interaction. In the diffusional controlled regime the nitrogen loss is found to be higher than that in the linear one. In this regime more nitrogen than aluminium atoms are delivered to the near surface region, where the AlN formation takes place. The nitrogen, which is in over-stoichiometric concentration diffuses to the gas phase, giving rise to loss of nitrogen. The sputtered rate of aluminium in the diffusional controlled regime for ion energy of 1.6 keV and current density of 0.2 mA/cm^2 is investigated too. It is determined by the deviation from the parabolic law and it is found to be $3.4 \times 10^{14} \text{ at/cm}^2\text{s}$. The binary collision simulations result in $3.8 \times 10^{14} \text{ at/cm}^2\text{s}$ sputtering rate of aluminium.

An investigation of phase formation and structure of the nitride layers is performed. It shows that, the hexagonal AlN without significant texture is the main crystallographic phase formed as a result of the ion nitriding of aluminium. A small content of a metastable f.c.c. AlN phase is also observed. It is found to be present in the nitride layer near to the interface with aluminium and has a preferred orientation related to that of the aluminium substrate. The aluminium nitride layers have a nano-crystalline structure. Investigation of the average size of the the hexagonal structured crystallites shows that it increases from 4 nm up to 10 nm by increasing the nitriding time from 20 min to 60 min respectively. The effect of annealing on the grain growth is found to be small.

A characterisation of the obtained nitride layers in terms of stoichiometry, atomic density, surface morphology as well as electrical and tribological properties is performed. The layers grown by ion nitriding of aluminium have a concentration close to the stoichiometric AlN. The amount of oxygen in the layers is negligible low (less than 2 at. %). No contamination of other elements is observed. This result fulfils one of the requirements for surface modification of aluminium. However, density and morphology of the obtained nitride layer are not very satisfactory. An atomic density of $7.5 \times 10^{22} \text{ at/cm}^3$ is determined, which is about 20 % lower than the standard value of AlN. The surface of the nitride layers is rough and after a nitriding time of about 60 min cracking and partly delamination of the layer occurs. The spalled parts peel off or get sputtered, which limits the thickness of the nitride layer. The maximum thickness achieved by ion nitriding of pure aluminium is about $1 \mu\text{m}$. An investigation of the macroscopic and microscopic strains in nitride layers with different thickness is performed by XRD, since the delamination suggests high stress in the layers. The measured macroscopic strains are lower than 1 %. The microscopic strains are determined to be between 0.3 % and 1.7 %. These results provide evidence for the stress in the nitride layer but a clear conclusion from the obtained results cannot be made, since the measurements are strongly affected by the local morphology. The analysis of the electrical properties demonstrates the dielectric character of the nitride layers. However, the electrical characteristics of the layers are also influenced by defects such as cracks and grain boundaries. The investigation of the tribological properties shows an improvement of the surface hardness and corrosion resistance as a result of the ion nitriding.

A study of the nitriding kinetic of the alloy AlMg_{4.5}Mn at an ion energy of 1.6 keV, a current density of 0.2 mA/cm² and a substrate temperature of 400 °C for nitriding times up to 4 h is performed. The results show that the nitride layer grows linearly with time at the same rate as in the case of pure aluminium. No limitation in thickness is observed. The layers produced by ion nitriding of AlMg_{4.5}Mn have a different surface morphology than that of pure aluminium. They are composed by several AlN particles, which are homogeneously distributed over the surface and therefore less cracks in the layers are created. In this context, ion nitriding of AlMg_{4.5}Mn alloy fulfils better the requirements for surface modification and therefore it is more appropriate for application purposes.

Considering the above presented results, it can be said that an improved understanding of the mechanism of aluminium ion nitriding is achieved by the present study. The obtained knowledge of the basic physical phenomena governing nitriding of aluminium and the influence of different process parameters and experimental conditions allows control over the formation, growth and properties of the nitride layers produced by ion nitriding of aluminium. Furthermore, this knowledge can also be applied to describe the mechanism of aluminium nitriding during PIII. The success in nitriding of aluminium by PIII can be explained by the influence of the surface oxide layer. Due to the relatively high energies provided by this method, a large amount of nitrogen is implanted behind the surface oxide and contributes to the growth of the nitride layer. It is also found that in methods which use low-energy ions, the ion bombardment can induce cleaning of the oxide surface simultaneously to the nitriding. Therefore, good vacuum conditions, in particular low partial pressure of oxygen, which is closely related to the ion energy and current density are required for the success of the nitriding process. This result can have an impact on the plasma nitriding in achieving a better reproducibility of the nitride layers. The industrial relevance of the obtained results has to be considered too. The obtained understanding of the nitriding process and the quantitative description of nitride layer growth kinetics as a function of process parameters and conditions could be used as a base to set a nitriding process on a large scale. The results obtained in the present study clearly show the advantage of AlMg_{4.5}Mn alloy over pure aluminium. However, the ion nitriding is restricted to certain alloys, which do not loose other properties due to the high temperature treatment. Finally it should be pointed out that the technological application requires nitride layers with better adhesion, smoother surfaces and higher density than the layers obtained in the present study. The later can give a direction for further research in the field of aluminium nitriding.

List of Figures

2.1	AlN wurtzite structure	6
2.2	Nuclear and electronic stopping power for atomic nitrogen ions in Al and AlN	12
2.3	The mean projected range of atomic nitrogen ions implanted into Al and AlN	13
2.4	Partial sputtering yields of nitrogen and aluminium, and backscattering yield of nitrogen	16
2.5	Al - N binary phase diagram	18
2.6	The magnitude of the diffusion coefficient for different mechanisms of diffusion	19
3.1	A sketch of the ion nitriding system	22
3.2	A sketch of the ion source	23
3.3	A scheme of the energy selective mass spectrometer (<i>HIDEN EQP 500</i>)	24
3.4	A schematic diagram of RBS scattering geometry	27
3.5	A schematic diagram of ERDA scattering geometry	28
3.6	A schematic diagram of mass and energy dispersive TOF ERDA geometry	29
3.7	TOF ERDA spectrum	30
3.8	NRA spectrum	31
3.9	NRA experimental spectrum and fit by WiNDF 6.5	32
3.10	Elemental profiles obtained by WiNDF 6.5	33
3.11	A schematic diagram of XRD at grazing incidence	34
3.12	A diagram of an Auger transition	36
4.1	Ion current density as a function of gas flow and potential applied to the filament of the ion source	38
4.2	The radial distribution of ion density	39
4.3	Characteristic ion mass spectrum of nitrogen ion beam	40
4.4	Ion energy distribution of N_2^+ and N^+	40
4.5	Partial pressure of H_2 , H_2O , O_2 , N_2 and CO_2 in the experimental chamber	42
4.6	Time evolution of oxygen and nitrogen depth profiles and their area densities	45
4.7	Nitrogen incorporation as a function of the ion energy	50
4.8	Nitrogen incorporation at a current density of 0.1 ma/cm^2 and an ion energy of 1.6 keV	51
4.9	Nitrogen incorporation at a current density of 0.2 ma/cm^2 and an ion energy of 1.6 keV	52

4.10 RBS spectra obtained after ion nitriding of aluminium with ^{14}N and ^{15}N and implantation with Au	56
4.11 Elemental depth profiles of ^{14}N , ^{15}N , aluminium and oxygen	57
4.12 Nitrogen profiles obtained after aluminium ion nitriding at different substrate temperatures	61
4.13 Nitride layer growth kinetic at different temperatures	62
4.14 An elemental piece of the sample indicating the zones formed during ion nitriding of aluminium	63
4.15 X-ray diffraction pattern at grazing incidence	68
4.16 An average grain size of the crystallites with hexagonal AlN structure	69
4.17 HRTEM cross-sectional image from an ion nitrided aluminium sample	70
4.18 SEM cross-sectional micrograph of aluminium nitride layer	73
4.19 Surface morphology of aluminium nitride layers	75
4.20 SEM cross-sectional micrograph showing delamination of the layer	75
4.21 Nitrogen profiles - deviation from rectangular to triangular shape	76
4.22 Nitride layer growth kinetic for nitriding times up to 2 h	76
4.23 Macroscopic strain determined by XRD	78
4.24 Microscopic strain determined by XRD	79
4.25 ERDA profiles of aluminium, nitrogen, oxygen and hydrogen	81
4.26 I - V characteristic of Al-AlN- Al structure	82
4.27 Breakdown characteristic of Al-AlN- Al structure	82
4.28 Depth dependence of the relative hardness enhancement due to ion nitriding	84
4.29 Potentiodynamic scans for untreated and nitrided aluminium samples	85
4.30 AES depth profiles of aluminium, nitrogen, oxygen and magnesium	87
4.31 Comparison between the growth kinetic of nitride layers grown on aluminium and $\text{AlMg}_{4.5}\text{Mn}$	88
4.32 Surface morphology of nitride layers grown by ion nitriding of aluminium and $\text{AlMg}_{4.5}\text{Mn}$	89

List of Tables

4.1	The growth rate and the sputter removal rate of surface oxide layer	47
4.2	Diffusion coefficients of aluminium in AlN	65
4.3	Composition of AlMg _{4.5} Mn	86

Bibliography

- [1] K. C. Walter, R. A. Dodd, and J. R. Conrad, Nucl. Instr. and Math. B **106**, 522 (1995).
- [2] J. H. Booske, I. Zhang, W. Wang, K. Mente, N. Zjaba, C. Baum, and J. L. Shohet, J. Mater. Res. **12**(5), 1356 (1997).
- [3] R. Gruen and D. Repenning, Proceedings of 2 nd. Conference on Ion Nitriding, Cleveland, Ohio, 376 (1989).
- [4] K. T. Rie, T. Stucky, R. A. Silva, E. Leitao, K. Bordji, J. Y. Jouzeau, and D. Mainard, Surf. Coat. Technol. **74-75**, 973 (1995).
- [5] N. Renevier, P. Collignon, H. Michel, and T. Czerwiec, Surf. Coat. Technol. **111**, 128 (1999).
- [6] D. L. Williamson, J. A. Davis, P. J. Wilbur, J. J. Vajo, R. Wei and J. N. Matossian, Nucl. Instrum. Meth. B **127/128**, 930 (1997).
- [7] S. Mändel, R. Günzel, E. Richter, and W. Möller, Surf. Coat. Technol. **100-101**, 372 (1998).
- [8] W. Möller, S. Parascandola, O. Kruse, R. Günzel, and E. Richter, Surf. Coat. Technol. **116-119**, 1 (1999).
- [9] E. Menthe and K. T. Rie, Surf. Coat. Technol. **116-119**, 199 (1999).
- [10] T. Arai, H. Fujita and H. Tachikawa, "Ion Nitriding" edited by T. Spalvinaas, American Society for Metals, Metals Park, 37, (1987).
- [11] S. Parascandola, O. Kruse, and W. Möller, Appl. Phys. Lett., **75**(13), 1851 (1999).
- [12] "ASM committee on gas carburising", carbonitriding and nitriding, vol. 4 of ASM Handbook, American society of metals, Materials Park, OH, pages 191-221 (1991).
- [13] "ASM committee on liquid carburising", vol. 4 of ASM Handbook, American society (1996).
- [14] S. Parascandola, PhD Thesis, Forschungszentrum Rossendorf e.V., Germany, (2001).

- [15] "CRC Handbook of Chemistry and Physics", 74th ed., edited by D. R. Linde, (CRC Boca Raton, FL), pages 4-36 (1994).
- [16] F. Vacandio, Y. Massiani, P. Gergaud, and O. Thommas, *Thin Solid Films* **359**, 221 (2000).
- [17] J. F. Shackelford and W. Alexander, "CRC Material Science and Engineering Handbook", Third Edition, MRS, California, USA (2000).
- [18] D. Liufu and K. C. Kao, *J. Vac. Sci. Technol. A* **16**, 2360 (1998).
- [19] M. A. Khan, J. N. Kuznai, D. T. Olson, J. M. Van Hove, and M. Blasingame, *Appl. Phys. Lett.* **60**, 2917 (1992).
- [20] P. F. Carcia, R. H. French, M. H. Reilly, M. F. Lemon, and D. J. Jones, *Appl. Phys. Lett.* **70**(18), 2371 (1997).
- [21] H. Okano, N. Tanaka, Y. Takahashi, T. Tanaka, K. Shibata, and S. Nakano, *Appl. Phys. Lett.* **64**, 166 (1994).
- [22] M. A. Dubois and P. Muralt, *Appl. Phys. Lett.* **74**, 3032 (1999).
- [23] V. Fuflyigin, E. Salley, A. Osinsky, and P. Norris, *Appl. Phys. Lett.* **77**(19), 3075 (2000).
- [24] B. Armas, M. de Icaza Herrera, and F. Sibieude, *Surf. Coat. Technol.* **123**, 199 (2000).
- [25] W. Zhang, Y. Romeno, M. Sasaki, and T. Hirai, *Jpn. J. Appl. Phys., Part 2* **32** L116 (1993).
- [26] D. C. Bertolet, H. Liu, and J. W. Rogers, *J. Appl. Phys.* **75**, 5385 (1994).
- [27] C. J. Sun, P. Kung, A. Saxler, H. Ohsato, K. Haritos, and M. Razeghi, *J. Appl. Phys.* **75**, 3964 (1994).
- [28] Y. Someno, S. Makoto, and T. Hirai, *Jpn. J. Appl. Phys.* **29**, 1358 (1987).
- [29] H. Itoh, M. Kato, and K. Sugiyama, *Thin Solid Films*, **146**, 255 (1987).
- [30] S. H. Lee, B. J. Kim, H. H. Kim, and J. J. Lee, *J. Appl. Phys.*, **80**, 1469 (1996).
- [31] G. Y. Meng, S. Xie, and D. K. Peng, *Thin Solid Films*, **334**, 145 (1998).
- [32] A. Bourret, A. Barskui, J. L. Rouviere, G. Renaud, and A. Barbier, *J. Appl. Phys.*, **83**, 2003 (1998).
- [33] K. Järrendahl, S. A. Smith, T. Zheleva, R. S. Kern, and R. F. Davis, *Vacuum* **49**, 189 (1998).
- [34] Z. Yang, L. K. Li, and W. I. Wang, *J. Vac. Sci. Technol B* **14**(3), 2354 (1996).

- [35] G. W. Auner, F. Jin, V. M. Naik, and R. Naik, *J. Appl. Phys.* **85**, 7879 (1999).
- [36] M. He, N. Cheng, P. Zhou, H. Okabe, and J. B. Halpern, *J. Vac. Sci. Technol. A*, **16**, 2372 (1998).
- [37] S. Six, J. W. Gerlach, and B. Rauschenbach, *Thin Solid Films* **370**, 1 (2000).
- [38] A. K. Sharma and R. K. Thareja, *J. Appl. Phys.*, **88**, 7334 (2000).
- [39] E. Gyorgy, C. Ristoscu, I. N. Mihailescu, A. Klini, N. Vainos, C. Fotakis, C. Ghica, G. Schmerber, and J. Faerber, *J. Appl. Phys.* **90**, 456 (2001).
- [40] W. J. Meng, J. Heremans, and Y. T. Cheng, *Appl. Phys. Lett.* **59**, 2097 (1991).
- [41] G. T. Kiechne, G. K. L. Wong, and J. B. Ketterson, *J. Appl. Phys.*, **87**, 5922 (1998).
- [42] K. Kusaka, T. Ao, T. Hanabusa, and K. Tominaga, *Thin Solid Films* **332**, 247 (1998).
- [43] E. Dogheche, D. Remiens, A. Boudrioua, and J. C. Loulergue, *Appl. Phys. Lett.* **74**, 1209 (1999).
- [44] S. Tungasmita, J. Birch, P. O. Persson, K. Jarrendahl, and L. Hultman, *Appl. Phys. Lett.*, **170**, 76 (2000).
- [45] H. Y. Joo, H. J. Kim, S. J. Kim, and S. Y. Kim, *Thin Solid Films* **368**, 63 (2000).
- [46] X. Wang, A. Kolitsch, F. Prokert and W. Möller, *Appl. Phys. Lett.* **71**, 1951 (1997).
- [47] S. Ohira and M. Iwaki, *Mater. Sci. Eng. A*, **116**, 153 (1989).
- [48] B. Rauschenbach, K. Brener, and G. Leonhard, *Nucl. Instr. and Meth. B* **50**, 401 (1990).
- [49] S. Lucas, G. Terwagne, and F. Bodart, *Nucl. Instr. and Meth. B* **47**, 396 (1990).
- [50] G. Terwagne and S. Lucas, *Surf. Coat. Technol.*, **51**, 368 (1992).
- [51] H. L. Lu, W. Sommer, M. Borden, J. R. Tesmer, and X. D. Wu, *Thin Solid Films* **289**, 17 (1996).
- [52] Y. Miyagawa, M. Ikeyama, K. Saitoh, S. Nakao, and S. Miyagawa, *Surf. Coat. Technol.* **83**, 275 (1996).
- [53] T. Reier, J. Schultze, W. Österle, and Chr. Buchal, *Surf. Coat. Technol.* **103-104**, 415 (1998).
- [54] V. Uglov, A. Laskovnev N. N. Cherenda, and V. V. Khodasevich, *Surf. Coat. Technol.* **83**, 296 (1998).

- [55] A.P. Matthews, M. Iwaki, Y. Horino, M. Satou, and K. Yabe, *Nucl. Instr. and Meth. B* **59/60**, 671 (1991).
- [56] T. R. Jervis, H. L. Lu, and J. R. Tesmer, *Nucl. Instr. and Meth. B* **72**, 59 (1992).
- [57] T. Reier, J. Schultze, W. Österle, and Chr. Buchal, *Thin Solid Films* **385**, 29 (2001).
- [58] H. Michel, T. Czerwiec, M. Gantois, D. Ablitzer and A. Ricard, *Surf. Coat. Technol.* **72**, 103 (1995).
- [59] H. R. Stock, C. Jarms, F. Seidel, and J. E. Döring, *Surf. Coat. Technol.* **94-95**, 247 (1997).
- [60] H. Y. Chen, H. R. Stock, and P. Mayr, *Surf. and Coat. Technol.* **64**, 139 (1994).
- [61] P. W. Wang, S. Sui, W. Wang, and W. Durrer, *Thin Solid Films* **295**, 142 (1997).
- [62] K. C. Walter, *J. Vac. Sci. Technol. B* **12(2)**, 945 (1994).
- [63] B. Reinhold, J. Naumann, and H. J. Spies, *HTM, Zeitschrift für Wärmebehandlung und Werkstofftechnik (in german)*, **53**, 329 (1998).
- [64] Y-K. Shim, Y-K. Kim, K. H. Lee, and S. Han, *Surf. Coat. Technol.* **131**, 345 (2000).
- [65] T. Czerwiec, H. Michel, and E. Bermann, *Surf. Coat. Technol.* **108/109**, 182 (1998).
- [66] T. Czerwiec, N. Renevier, and H. Michel, *Surf. and Coat. Technol.* **131**, 267 (2000).
- [67] E. I. Meletis and S. Yan, *J. Vac. Sci. Technol. A* **9(4)**, 2279 (1991).
- [68] N. Renevier, P. Collignon, H. Michel, and T. Czerwiec, *Surf. and Coat. Technol.* **86-87**, 285 (1996).
- [69] N. Renevier, T. Czerwiec, P. Collignon, and H. Michel, *Surf. and Coat. Technol.* **98**, 1400 (1998).
- [70] N. Renevier, T. Czerwiec, A. Billard, J. von Stebut, and H. Michel, *Surf. and Coat. Technol.* **116-119**, 380 (1999).
- [71] S. Kumar and P. K. Ghosh, *J. Appl. Phys.* **26**, (1993) 1419.
- [72] M. Quast, P. Mayr, and H. R. Stock, *Surf. Coat. Technol.* **120-121**, 244 (1999).
- [73] M. Quast, P. Mayr, H. R. Stock, H. Podlesac, and B. Wielage, *Surf. Coat. Technol.* **135**, 238 (2001).
- [74] M. Hudis, *J. Appl. Phys.* **44**, (1973) 263.

- [75] C. K. Johnes, S. W. Martin, D. J. Struges and M. Hudis, in: Proc. Heat Treatment Conf., Metals Society, London, 1973, 71.
- [76] Y. Baba and T. A. Sasaki, Mater. Sci. Eng. A **115** (1989) 203.
- [77] T. A. Sasaki, Y. Baba and H. Yamamoto, Vacuum **41** (1990) 185.
- [78] G. M. Lancaster and J. W. Rabalais, J. Chem. Phys. **83** (1979) 209.
- [79] G. G. Tibbetts, J. Appl. Phys. **45** (1974) 5072.
- [80] A. Ricard, T. Czerwicz, T. Belmonte, S. Bockel, and H. Michel, in Proc. of the 1st Asian-European Int. Conf. on Plasma Surf. Engineering, Seoul, South Korea, 98 (1997).
- [81] W. Ensinger, Nucl. Instr. and Meth. B **120**, 270 (1996).
- [82] R. Günzel, E. Wieser, E. Richter, and J. Steffen, J. Vac. Sci. Technol. B **12**(2), 927 (1994).
- [83] M. Nunogaki, H. Suezawa, Y. Kuratomi, and K. Miyazaki, Nucl. Instr. and Meth. B **39**, 591 (1989).
- [84] K. C. Waiter, R. A. Dodd, and J. R. Conrad, Nucl. Instr. and Meth. B **106**, 522 (1995).
- [85] C. Blawert and B. L. Mordike, Nucl. Instr. and Meth. B **127/128**, 873 (1997).
- [86] S. Schoser, G. Brauchle, J. Forfet, K. Kohlhof, T. Weber, J. Voigt, and B. Rauschenbach, Surf. Coat. Technol. **103-104**, 222 (1998).
- [87] D. Manova, P. Hubert, S. Mändel, and B. Rauschenbach, Surface and Coating Techn., **128-129**, 249 (2000).
- [88] D. Manova, S. Mändel, and B. Rauschenbach, Nucl. Instr. and Meth. B **178**, 291 (2001).
- [89] E. Richter, R. Günzel, S. Parascandola, T. Telbizova, O. Kruse, and W. Möller, Surf. and Coat. Technol. **128-129**, 21 (2000).
- [90] S. Simson, T. Reier, J. W. Schultze, and Chr. Buchal, Surf. Coat. Technol. **83**, 49 (1996).
- [91] K. T. Rie, Surf. Coat. Technol. **112**, 56 (1999).
- [92] W. Österle, I. Dörfel, I. Urban, T. Reier, and J. W. Schultze, Surf. and Coat. Technol. **102**, 168 (1998).
- [93] H. K. Sanghera, J. L. Sullivan, and S. O. Saied, Appl. Surf. Sci. **141**, 57 (1999).
- [94] A. Anders, 3rd International Workshop on Plasma-Based Ion Implantation and deposition, Dresden, Germany (1996).

- [95] H. Takikawa, K. Shinsako, and T. Sakakibara, *Thin Solid Films* **316**, 73 (1998).
- [96] D. Manova, P. Huber, S. Mändl, and B. Rauschenbach, *Surf. Coat. Technol.* **142-144**, 61 (2001).
- [97] H. Takikawa, K. Kimura, R. Miyano, T. Sakakibara, A. Bendavid, P. J. Martin, A. Matsumuro, and K. Tsutsumi, *Thin Solid Films* **386**, 276 (2001).
- [98] "Phase transformation during irradiation" edited by F. V. Nolfi, Applied Science Publishers, London, (1983).
- [99] M. Nastasi, J. W. Mayer and J. K. Hirvonen, *Ion-solid interactions: fundamentals and applications*, University Press, Cambridge, Great Britain, (1996).
- [100] A. Anders (ed.), *Handbook of plasma immersion ion implantation and deposition*, A Wiley-Interscience publication, USA, (2000).
- [101] J. F. Ziegler, SRIM, the program is downloaded from <http://www.research.ibm.com/ionbeams/home.htm>.
- [102] P. C. Zalm, *Vacuum*, **36**, 787 (1986).
- [103] J. F. Ziegler, J. P. Biersack, and U. Littmark, "The stopping and range of ions in matter", Pergamon, New York, USA, (1985).
- [104] P. Sigmund, *Phys. Rev.* **184**, 383(1969).
- [105] W. Möller and W. Eckstein, *Appl. Phys. A* **34**, 73 (1984).
- [106] W. Möller, W. Eckstein, and J. P. Biersack, *Comput. Phys. Commun.* **51**, 355 (1988).
- [107] W. Möller and M. Posselt, "TRIDYN FRZ User Manual", Institute of Ion Beam Physics and Materials Research, Research Centre Rossendorf, Germany, FZR-317, (2001).
- [108] I. Popova, V. Zhukov, and J. T. Yates, *J. of App. Phys.*, **87**, 8143 (2000).
- [109] H. Brune, J. Winterlin, R. J. Behm, and G. Ertl, *Phys. Rev. Lett.* **68**, 624 (1992).
- [110] Gassmann, G. Schmitz, J. Boysen, F. Bartolucci, and R. Franchy, *J. Vac. Sci. Technol. A* **14**(3), 813 (1996).
- [111] D. J. Lichtenwalner, A. Anderson, D. A. Rudman, and D. A. Rudman, *J. Vac. Sci. Technol. A* **8**(3), 1283 (1990).
- [112] D. A. Porter and K. E. Easterling, "Phase transformations in metals and alloys", published by Chapman and Hall, London, UK (1992).
- [113] J. Philibert, "Atom movements diffusion and mass transport in solids", Les edition de physique, France (1991).

- [114] H. A. Wriedt, in: "Binary Alloy Phase Diagrams", edited by T. Massalski, ASM International, USA, **1**, 177 (1990).
- [115] S. Lucas and J. Chevallier, *Surf. and Coat. Technol.*, **51**, 441 (1992).
- [116] S. Lucas and J. Chevallier, *Surf. and Coat. Technol.*, **65**, 128 (1994).
- [117] V. I. Dimitrov, J. D'Haen, G. Knuyt, C. Quaeys, and L. M. Stals, *Comp. Mat. Sci.*, **15**, 22 (1999).
- [118] V. I. Dimitrov, G. Knuyt, L. M. Stals, J. D'Haen, and C. Quaeys, *Appl. Phys. A* **67**, 183 (1998).
- [119] D. Gupta and P. S. Ho, "Diffusion phenomena in thin films and microelectronic materials", Noyes Publications, New Jersey, USA (1988).
- [120] M. Zeuner, J. Meichsner, H. Neumann, F. Scholze, and F. Bigl, *J. Appl. Phys.* **80**(2), 611 (1996).
- [121] M. Zeuner, H. Neumann, F. Scholze, D. Flamm, M. Tartz, and F. Bigl, *Plasma Sources Sci. Technol.* **7**, 252 (1998).
- [122] E. Rutherford, *Philos. Mag.* **21**, 666 (1911).
- [123] W. H. Bragg and R. Kleeman, *Philos. Mag.* **10** (1905) 318.
- [124] W. Assmann, H. Huber, C. Steihausen, M. Dobler, H. Gluckler, and A. Weidinger, *Nucl. Instrum. Meth. B* **89**, 131 (1994).
- [125] S. Grigull, U. Kreissig, H. Huber, and W. Assmann, *Nucl. Instrum. Meth. B* **132**, 709 (1997).
- [126] U. Kreissig, S. Grigull, K. Lange, P. Nitzsche, and B. Schmidt, *Nucl. Instrum. Meth. B* **136-138**, 679 (1998).
- [127] N. P. Barradas, WinDF 6.5, <http://www.ee.surrey.ac.uk/SCRIBA/ndf/>
- [128] N. P. Barradas, C. Jeynes, and R. P. Webb, *Appl. Phys. Lett.* **71**(2), 291 (1997).
- [129] N. P. Barradas and R. Smith, *J. Phys. D: Appl. Phys.* **32**, 2964 (1999).
- [130] L. R. Doolittle, *Nucl. Instr. and Meth. B* **15**, 227 (1985).
- [131] C. Spaeth, F. Richter, S. Grigull, and U. Kreissig, *Nucl. Instr. and Meth. B* **140**, 243 (1998).
- [132] Powder Diffraction File, Joint Committee on Powder Diffraction Standards Swarthmore, Pennsylvania.
- [133] L. Bimbault, K. F. Badawi, Ph. Goudeau, V. Branger, and N. Durand, *Thin Solid Films*, **275**, 40 (1996).

- [134] N. Durand, K. F. Badawi, and Ph. Goudeau, *J. Appl. Phys.* **80**(9), 5021 (1996).
- [135] W. Kraus and G. Nolze, PowderCell, <http://www.ccp14.ac.uk/>
- [136] M. Liberman and A. Lichtenberg, "Principles of plasma discharges and materials processing", John Wiley & Sons, New York, USA (1994).
- [137] A. Makarem, Hussein, G. A. Emmert, N. Herschkowitz, and R. Claude Woods, *J. Appl. Phys.* **72**(5), 1720 (1992).
- [138] A. P. H. Goede, T. S. Green, and B. Singh, *J. Appl. Phys.* **51**(4), 1896 (1980).
- [139] H. C. Straub, P. Renault, B. G. Lindsay, K. A. Smith, and R. F. Stebbings, *Phys. Rev. A*, **54**(3), 2146 (1996).
- [140] T. Majeed and D. J. Strickland, *J. Phys. Chem. Data*, **26**(2), 335 (1997).
- [141] K. K. Bourdelle and D.O. Boema, *Mat. Res. Soc. Symp. Proc.* **279**, 485 (1993).
- [142] R. Boistelle and J. P. Astier, *J. Cryst. Growth.* **90**, 14 (1988).
- [143] H. Holleck, *J. Vac. Sie. Technol. A*, **4**, 2661 (1986).
- [144] "Aluminium-Taschenbuch" edited by W. Hufnagel, Aluminium - Verlag. Düsseldorf, 14th edn, (1988).
- [145] H. Ljungcrantz, L. Hultman, J. E. Sundgren, and L. Karlsson, *J. Appl. Phys.* **78**(2), 832 (1995).
- [146] I. D. Wolf, M. Ignat, G. Pozza, L. Maniguet, and H. E. Maes, *J. Appl. Phys.* **85**(9), 6477 (1999).
- [147] I. Owate and R. Freer, *J. Appl. Phys.* **72**(6), 2418 (1992).
- [148] J. Meinschien, F. Falk, R. Hergt, and H. Stafast, *Appl. Phys. A* **70**, 215 (2000).
- [149] W. Biller, D. Heyden, D. Müller, and G. K. Wolf, *Surf. Coat. Technol.* **116-119**, 537 (1999).
- [150] T. Chudoba, PhD Thesis, Forschungszentrum Rossendorf e.V., Germany, (1996).
- [151] "Library of Congress Cataloging-in-Publication Data", edited by R. Baboian, Philadelphia, U. S. A., (1995).
- [152] S. B. de Wexler and J. R. Galvele, *J. Electrochem. Soc.* **121**, 1271 (1974).
- [153] M. P. Natishan, E. McCafferty, and G. K. Hubler, *J. Electrochem. Soc.* **135**, 321 (1988).
- [154] L. Guzman, G. Bonini, M. Adami, P. M. Ossi, A. Miotello, M. Vittori-Antisari, A. M. Serventi, and E. Voltolini, *Surf and Coat. Technol.* **83**, 284 (1998).

-
- [155] H. J. Spies, HTM, Zeitschrift für Wärmebehandlung und Werkstofftechnik (in german), **55**, 135 (2000).
- [156] H. J. Spies, HTM, Zeitschrift für Wärmebehandlung und Werkstofftechnik (in german), **55**, 141 (2000).
- [157] A. M. Serventi, M. V. Antisari, L. Guzman, and A. Miotello, Mat. Res. Soc. Symp. Proc. **400**, 287 (1996).
- [158] J. Datta, "Key to aluminium alloys", Aluminium-Verlag Marketing & Kommunikation GmbH Düsseldorf, Germany, (1997).
- [159] H. P. Klug and L. E. Alexander, "X-ray diffraction procedures for polycrystalline and amorphous materials", Wiley, New York, (1984).

Acknowledgement

Here I would like to thank all people which contribute for the success of this work. Especially to:

- Prof. Dr. W. Möller for giving me the opportunity to work on my PhD thesis in the Institute of Ion Beam Physics & Materials Research in the Research Centre of Rossendorf.
- Prof. E. Wieser for scientific discussions and his help during writing this thesis.
- Dr. F. Prokert for XRD measurements, data evaluation and several helpful discussions.
- Dr. R. Grötschel and Dr. U. Kreissig for IBA measurements, lessons and advices.
- Dr. T. Chevolleau for his help in performing the ion beam diagnostic, creative conversations and advices in work with electronic devices.
- Dr. S. Parascandola for his help and contribution to this study.
- Dr. R. Günzel for suggesting the experiment with different isotopes of nitrogen.
- Dr. E. Richter for his help and support in solving administrative problems.
- Dr. A. Mücklich for TEM measurements and discussion, as well as A. Kunz and M. Missbach for the preparation of the cross sectional samples.
- Dr. B. Schmidt and I. Beatus for the competent and fast deposition of aluminium films, electrical measurements and chemical etching.
- Dr. M. Seidel and G. Anwandt for their experienced technical support.
- R. Aniol and H. Seifert for the mechanical preparation of the samples.
- My colleagues and friends: Dr. J. Noetzel, Dr. M. Maitz, M. Peikert, B. Fritsche and R. Bhandari for their moral support and nice working atmosphere.
- My husband Dr. C. Fitz for giving me help and encouragement when I really needed it.

Declaration

Hiermit versichere ich, die vorliegende Arbeit ohne unzulässige Hilfe Dritter und nur unter Benutzung der angegebenen Hilfsmittel angefertigt zu haben. Die aus fremden Quellen oder indirekt übernommenen Gedanken sind als solche kenntlich gemacht. Die Arbeit wurde bisher weder im Inland noch im Ausland in gleicher oder ähnlicher Form einer anderen Prüfungsbehörde vorgelegt.

Diese Arbeit wurde am Institut für Ionenstrahlphysik und Materialforschung des Forschungszentrums Rossendorf unter der wissenschaftlichen Betreuung von Herrn Prof. Dr. W. Möller angefertigt.

Die Promotionsordnung der Fakultät für Mathematik und Naturwissenschaften der Technischen Universität Dresden vom 20. März 2000 erkenne ich an.

Rosendorf, den March 3, 2002